Keshavanarayana, Pradeep (2019) *Experimental and numerical investigations of stress fibre reorientation in biological cells.* PhD thesis.

https://theses.gla.ac.uk/41149/

Experimental and numerical investigations of stress fibre reorientation in biological cells

Pradeep Keshavanarayana

Submitted in fulfilment of the
requirements of the degree of
Doctor of Philosophy

School of Engineering
University of Glasgow

April 2019

Abstract

Cells are the fundamental units of living organisms controlling the behaviour of tissues, organs and thereby the organ system. The mechanical stimuli has been found to contribute towards changes in mechanical properties of cells, sometimes resulting in diseases. In order to quantify the response of cells to mechanical stimuli, a variety of experiments have been carried out. They have helped us to understand the effects of different types of stimuli, responses in different length and time scales, effect of different environmental factors, and the relation between different components of the cell. Focal adhesions present on the cell membrane contain mechanosensitive proteins called integrins which can form a connection between the cell and the extra cellular matrix, and thus sense the properties of the substrate and thereby the external stimuli. This creates a chain of biochemical reactions within the cytoplasm, leading to a cross bridge between the actin and myosin proteins in the presence of calcium ions, forming stress fibres. In this regard, cyclic loading experiments have been performed to understand the nature of connection between the growth of focal adhesions and stress fibres. In this thesis, a novel DIY design of an uniaxial cell stretcher has been designed and the manufacturing process using 3D printing technology has been explained. The device has been used to apply uniaxial cyclic load with different amplitudes, keeping the frequency constant to study the response of cells to changing strains. The experiments have been performed on two types of cells, fibroblasts and osteoblasts. The results are analysed quantitatively and the stress fibre orientation is studied for varying loading conditions for each cell type.

Since the experiments performed are *in vitro*, the numerical models are developed in order to apply *in vivo* type loading and study the response of cells. In this regard, a numerical model is developed where in the already existing stress fibre and focal adhesion growth models are extended and coupled through a feedback loop involving cytoplasmic calcium concentration. Stress fibre is assumed to depend on the calcium concentration and the active stress, while focal adhesion is modelled by assuming that integrins which exist in two states are in thermodynamic equilibrium. The active stress is taken as a product of strain-rate and strain dependent functions. The focal adhesion forming a bond with the substrate, and the cell provides a traction force to the cell. To consider the variation of calcium concentration depending on the focal adhesion growth, a feedback loop is introduced. The effect of substrate stiffness on the response of cells is analysed. The model thus developed is used to obtain solutions to numerical problems simulating biological phenomenon including stress fibre reorientation due to changing amplitude of cyclic loading.

The mathematical model developed results in a coupled system of equations, for which the solution scheme needs special consideration. Noting the limitation on the time step that could be used with the staggered coupling scheme, a monolithic coupling scheme is developed where the system of equations are solved simultaneously. The variational formulation of the constitutive equations have been derived along with the algorithmic aspects of the solution schemes. Solution is obtained by following finite element method with large strain formulation. Numerical problems have been solved to compare the coupling schemes for space and time refinements, and for changing parameter values. The convergence behaviour of the solution schemes have been analysed. Finally, the solution obtained from the numerical scheme have been compared with the experimental observations, and the ways this project could be extended has been discussed. Some of the important results that could be drawn from this thesis are

(i) A novel compact 3D-printed cell stretcher which has the size of a standard 96-well plate.

(ii) Stress fibres are formed predominantly in directions away from the direction of loading, when cells are subjected to uni-axial cyclic stretch.

(iii) Reorientation is higher with increasing amplitude of the cyclic loading.

(iv) Mathematical model for stress fibre growth has been coupled with focal adhesions' and the cytoplasmic calcium is controlled through a feedback loop.

(v) Feedback loop plays a crucial role in simulating experiments such as optical tweezers, and ROCK inhibition.

(vi) Uni-axial cyclic stretch simulation results could be qualitatively compared to the average results obtained from experiments.

(vii) Coupling the system of equations can be performed following either a staggered or a monolithic approach.

(viii) Monolithic approach allowed using higher time step values, while staggered approach had limitations in the time step, and the parameter values that could be used.

Acknowledgements

First of all, my deepest gratitude would go to René de Borst for choosing me as the PhD candidate for the exciting topic at offer. Because of which, from not knowing to where exactly Glasgow was, before accepting this offer, to, spending 4 years at this lovely place, it has been a wonderful learning journey. I would like to thank him for providing me the freedom to choose the path in solving the quest, while the advices he provided were always the best. I got to learn a lot working with him, especially his time management, and academic writing skills, for which I am very grateful.

I would also like to thank another supervisor of mine, Martin Ruess, who guided me with his positive critics and helped me develop many aspects of research. I am very grateful for the constant support he provided in terms of research, and otherwise, and for sharing his thoughts on a wide variety of topics. Paying attention to even the smallest of details is something that I learnt from him, and has helped me during every stage of my PhD, and will be really useful in future too. I thank René and Martin for their extended support in writing research articles and attending conferences.

A big thanks to my another supervisor Nikolaj Gadegaard, who has been very helpful since the beginning of my PhD. His encouraging ideas have been a motivation to work even when nothing was working. Many a times, on-the-stairs meeting was sufficient to overcome weeks of hurdles. His enthusiasm for doing a wide variety of research and managing all of them with equal prominence is very inspiring. I would also like to thank him for all the support he provided with the thesis submission. I would also like to thank Daniel Mulvihill for providing me the DIC setup, and Ewan Russell for 3D printing.

I have to extend thanks to my colleagues in the computational group, Julian, Stefan, Remi, Zahur, Ignatius, Karol; the discussions with whom has helped me improve my knowledge and clear many doubts. The usual lunch talks from a wide ranging topics from food to culture to politics to environment, and about food again has been very delightful.

Transition from civil engineering to cell culture has been possible only because of my colleagues in the BIG group. A special thanks to Marie, who trained me in cell culture, and for the (false) hopes that experiments would be over very soon. Thanks for the support in working over the weekends and for imparting me the motivation to work more. Thanks also to Rachel, Paul, Badri, Eline, Emma for all the bio discussions and for teaching me the tips and tricks to keep the cells alive.

Life in Glasgow would not have been the same without having close friends. Thanks to Bhavana for being my bestie, and cheers to all those debates and Kannada banters, laughter and tears, and infinite visits to Rishis, without which life would have been so dreary. Thanks to Nivasan, Shoubhik, and Wenting for their BEST stories with imitations, and to Pavi for all the hiking and cycling trips. Finally to Vasilis and Archan for being my flatmates, and for all the good times.

I could not have come to this stage without the incessant support of my family and teachers. Gratitude to my parents who were my first teachers, and have been one ever since. They have taught me many important lessons of life through their actions with hard work and patience. Thanks to other relatives whom I have taken inspiration from, since my childhood. Thanks to all the inspiring teachers I have had, especially Rao, Narasimhan, Babunarayan, Christian, and Manfred, who have developed in me the interest to pursue scientific research.

Finally, in this day and age, I should also thank the people of Glasgow for making this city a very friendly place to live.

Declaration

I declare that, except where explicit reference is made to contribution of others, this dissertation is the result of my own work and has not been submitted for any other degree at University of Glasgow or any other institution.

Pradeep Keshavanarayana

Outcomes

Parts of this thesis have been published as the following journal articles :

- Pradeep Keshavanarayana, Martin Ruess, and René de Borst. A feedback-loop extended stress fiber growth model with focal adhesion formation. *International journal of solids and structures*, 2017. DOI: 10.1016/j.ijsolstr.2017.08.023
- Pradeep Keshavanarayana, Martin Ruess, and René de Borst. On the monolithic and staggered solution of cell contractility and focal adhesion growth. *International journal for numerical methods in biomedical engineering*, 2018. DOI: 10.1002/cnm.3138

Contents

List of Tables

List of Figures

List of Algorithms

Nomenclature

Abbreviations

ECM	Extra cellular matrix
FA	Focal adhesion
SF	Stress fibre
PLA	Polylactic Acid
PC	Polycarbonate
FDM	Fused deposition modelling
DIC	Digital image correlation
FEM	Finite element method
PDMS	Polydimethylsiloxane
LMW	Low molecular weight
BCS	Bovine calf serum
DMEM	Dulbecco's Modified Eagle's Medium
p/s	Pencillin streptomycin

Symbols

η	Stress fibre concentration
C	Calcium concentration
κ_f	Rate of association of stress fibres
κ_b	Rate of dissociation of stress fibres
σ^a	Active stress in stress fibres
σ^p	Passive stress in stress fibre
σ_0	Isometric stress in stress fibres
σ_{max}	Maximum stress allowed
$f(\varepsilon)$	Strain dependent function
$g(\dot{\varepsilon})$	Strain rate dependent function
S_{exp}	Expansion parameter
$\mathbf{u}$	Displacement vector
$\boldsymbol{\Delta}$	Stretch vector
ξ_H	Concentration of high affinity integrins
ξ_L	Concentration of low affinity integrins
ξ_0	Total number of integrins
$\bar{S}$	IP3 concentration
σ^{sub}	Substrate stress
Σ	Total stress in the cell
C^{sub}_{ijkl}	Substrate elasticity tensor
$\mathbf{F}$	Deformation gradient
$\mathbf{N}$	Bilinear shape function matrix
$\mathbf{B}_L$	Linear contribution to strain displacement matrix
$\mathbf{B}_N$	Nonlinear contribution to strain displacement matrix
$\mathbf{E}$	Green-Lagrangian strain tensor
$\mathbf{S}$	Second Piola-Kirchoff stress tensor
$\boldsymbol{\tau}$	First Piola-Kirchoff stress tensor
OL	Osteoblast cells subjected to low amplitude load
OH	Osteoblast cells subjected to high amplitude load
FL	Fibroblast cells subjected to low amplitude load
FH	Fibroblast cells subjected to high amplitude load
OR	Osteoblast cells in their reference state

FR	Fibroblast cells in their reference state
CV	Circular variance

1. Introduction

The anatomy of living beings is more complex than that of the man-made systems. Because of the inherent complexity, myriad processes occur simultaneously resulting in convolute interactions between several components of an organ system. In spite of such intricacy, processes are highly optimized, and efficient. Human beings, apparently the most intelligent creatures, are on a never ending quest to make life more comfortable. As devices become more intricate, there is a higher necessity to give importance to even the minute details of the mechanisms, and optimise them. In this regard, it is a great thought to get inspiration and ideas from the well developed natural habitat, and build systems that would make lives simpler, and better. One of the very famous examples is of Leonardo da Vinci, a scientist, and an artist, who had begun the study to understand the movement of birds to create an aircraft. Historically, many of the architectural marvels have been designed and built having been inspired from the structural elements in Nature. Carrying this forward, terms such as *bio-inspired structures* and *biomimetics* have been coined to develop this field of study.

The scientific study of living organisms is undoubtedly multi-disciplinary, involving a number of biological, chemical, and mechanical processes occurring simultaneously. Understanding the behaviour of biological systems using the concepts of mechanics is termed *biomechanics* [1], and since finding the solution to a problem in mechanics involves mathematical discourse, it is also sometimes referred to as *mathematical biology* [2]. Thus, by developing theories, to complement experimental studies, it is possible to obtain an analytical perspective to the multi-physics stimuli resulting in a biological response. As reviewed in [3], the earliest books containing the concepts of biomechanics were probably the Greek classic *On the Parts of Animals* by Aristotle and the Chinese book *Nei Jing*. The field of biomechanics has been advanced by the contributions of many well known scientists, including Galileo Galilei, William Harey, René Descartes, and Isaac Newton. The invention of prosthetic heart valves and other heart assist devices, which has solved many clinical problems in cardiovascular systems, have been possible due to biomechanics. It has also helped in the development of prosthetic legs and arms, and has assisted in the advancement of sports science as well.

In order to discern the behaviour of the living body in its entirety it is necessary to study its mechanics, beginning from cells. In a human body, the number of cells is three orders of magnitude greater than the number of stars in the Milky way, yet, there are only about 200 different types of cells [4]. Many experimental procedures have been developed over time to understand the organisation, function and behaviour of cells. It has been found that, each type of cells has its own shape, size, and mechanical properties. For example, nerve cells are shaped like a tree with a cylindrical body and branches at the top while cardiac cells have the shape of fibres cross-linked to each other. In order to understand the mechanisms of organs, which are formed by the tissues and in-turn by cells, it becomes important to study the mechanics of cells. This field of study has been termed *cell mechanics* [5].

With recent advancements in experimental techniques such as atomic force microscopy (AFM), optical stretcher, it has been possible to observe the behaviour of cells and sub-cellular structures in more detail, and understand to an extent the mechanisms involved. State-of-the-art optical technologies have made it possible to view sub-cellular parts with higher resolution, while modern fabrication devices have made studies of individual cells possible. But, since most of the experiments are performed outside the living body, usually on the glass dish, termed *in vitro*, there is a necessity to develop theories that can map these experimental observations to the conditions within a living body, termed *in vivo*. In this regard, mathematical models, simulating the environment of a living body, can be used along with experimental observations to predict the *in vivo* responses. Hence, with state-of-the-art computational technologies, experiments have been successfully bolstered by numerical analyses, and the predictions of the behaviour of cells under different environmental conditions are being possible.

1.1. Background and motivation

Recent experiments on a variety of cells, especially on fibroblasts and endothelial cells have shown that cells respond to external mechanical stimuli [6–8]. The behaviour of cells was found to vary based on the mechanical properties of the material surrounding the cells, termed extracellular matrix (ECM), and the loading type. In particular, it has been found that cells reorient away from the direction of loading when a uniaxial cyclic loading is applied to the substrate onto which the cells are attached, as observed with fibroblasts, Fig. 1.1 [9]. It has also been observed that cellular reorientation depends on the stiffness of the substrate used, and parameters of the loading cycle. This has also led to the observation of an existence of a mechanism for continuous crosstalk between different sub-cellular parts of the cell.

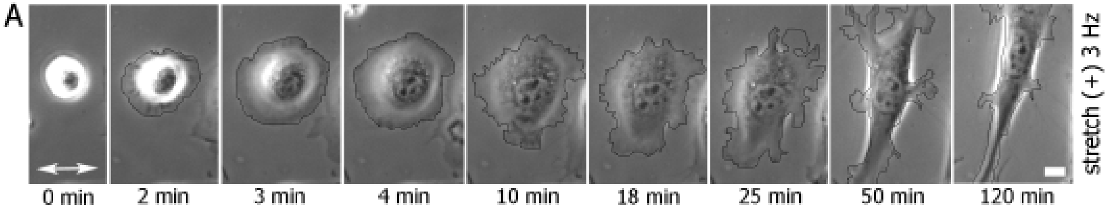

Fig. 1.1: (A)Reorientation of Fibroblasts subjected to cyclic strain, as observed in [9]. Direction of cyclic loading is indicated by the bi-directional arrow. Frequency was chosen to be 3Hz. It can be observed that, with time, cell reorients away from the direction of loading. Scale = 10μm.

Over the past few years, there have been numerous attempts on developing computational models for simulating such reorientation phenomenon [10, 11]. The main scheme of a computational model is to start by constructing the geometric model of the body, upon which the mathematical model involving the governing equations has to be solved, as indicated by undeformed geometry or reference configuration in Fig. 1.2(A). The domain of the geometry can then be discretised into subdomains and converted into a numerical model using any of the schemes such as Finite elements or Finite differences and the boundary conditions are applied to the numerical model, as shown in Fig. 1.2(B). The numerical model can then be solved to obtain the final configuration of the body. The solution obtained can be represented as the deformed geometry, and indicates the final configuration, as shown in Fig. 1.2(C).

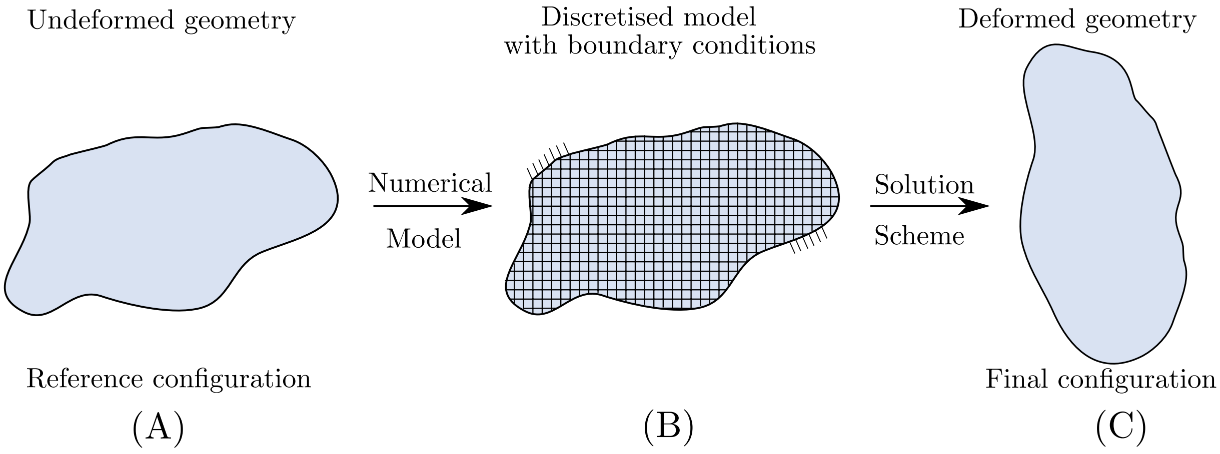

Fig. 1.2: Converting geometrical model of cell to a numerical model and then solving to obtain the final configuration. (A) Reference configuration indicates the geometric model of the body prior to any loading. (B) Discretisation of the whole domain to finite sub domains, indicated by rectangles within the body, and the applied boundary conditions indicated by straight lines on the boundary. (C) Solution of the numerical problem represented by deformed geometry, indicating the final configuration.

1.2. Aims of the project

Even though there are several mathematical models developed to explain various cellular processes individually, it was found that, an explicit connection between several cytoplasmic proteins resulting in a feedback loop would be necessary to simulate the right behaviour caused due to their interactions. Hence, there was a need to study different cellular processes including reorientation using a model involving such a feedback loop. In addition, since modelling of cells involves solving a multi-physics coupled system of equations, the solution scheme and the type of coupling plays an important role in obtaining the right solution. In addition to having a right model which can describe the cellular mechanisms, it is necessary to have a robust numerical scheme as well. Hence, finding the right solution scheme that can give meaningful results over a wide range of parameters representing experiments on different cells is necessary. In addition, experiments had to be carried out in order to validate the numerical results and further design studies to understand the behaviour of cells. In this regard, the main aims of the project were:

- Designing and building a cell stretcher in order to perform cyclic loading experiments
- Developing a robust numerical model for cell contractility including feedback loop

- Analysing different coupling schemes and comparing their numerical efficiencies
- Validating the numerical model using experimental results.

1.3. Thesis layout

The thesis is divided into 6 chapters with following contents in each:

- Chapter 1 : A brief introduction to the topic and the objectives of the thesis has been provided.
- Chapter 2 : An introduction to the cellular biology is given detailing the important components and mechanisms of the cell. A brief literature review of the experiments and numerical modelling focussing on the stress fibre reorientation phenomenon is given.
- Chapter 3 : The uniaxial cyclic loading experiments performed on fibroblast and osteoblast cells are explained. The design of the cell stretcher and the additive manufacturing process used is described. Detailed procedure of the quantitative analysis performed is given and the results are compared between two cell types.
- Chapter 4 : The numerical model developed to explain the process of stress fibre growth coupled with focal adhesion formation, including the feedback loop is explained. Numerical examples are provided and compared with experimental observations. This chapter is based on P.KESHAVANARAYANA *et.al* [12].
- Chapter 5 : The numerical schemes followed to couple the governing equations is analysed through the variational formulations. Effect of space and time refinement on the solution schemes is analysed. This chapter is based on P.KESHAVANARAYANA *et.al* [13].
- Chapter 6 : Conclusion is provided by discussing each chapter. The experiments that could be done, and the possible extension to numerical modelling is given as future work.

2. Cell Mechanics

2.1. Response to stimuli

It is known that the growth of tissues is greatly influenced by external mechanical forces. For example, the remodelling of bones can be controlled by the applied mechanical forces [14]; and tissues can be repaired by exercises [15]. Cells, the fundamental units of living organisms, in the presence of extra cellular matrix (ECM), make a functional ensemble to form tissues, tissues form organs, which function together as an organ system. Thus, for controlling the structure of bones and muscles, and for an organ system to work in unison, cells have to function systematically. Cells have the ability to sense stimuli from its surroundings, the ECM, and respond based on its magnitude and type. Response to stimuli can lead to different cell behaviours such as proliferation (reproduction of cell), gene expression and synthesis, and secretion of proteins. Sometimes, either because cells sense the stimuli wrongly or the stimuli itself is affected, the cellular response is compromised, which might push the cell to a diseased state. Thus, diseases such as diabetes, malaria, and cancer can be detected by observing variations in cellular behaviour.

Over the past few decades, the role of mechanical forces in cellular response is being studied [16–18]. A wide variety of research has established the connection that exists between mechanical and biological properties of cells. The shape and structure of cells, tissues and organs have been extensively studied [1, 3]. Experimental techniques have been devised, advanced over years, to measure the mechanical properties of cells. Experiments have shown that cells sense and respond to stimuli resulting in the dynamic behaviour of tissues and organs. But the question yet to be answered precisely is, how cells sense the various mechanical, biological, chemical and electrical stimuli and convert them into corresponding mechanical or biological responses.

Cells, as a response to stimulus, may alter their structure to maintain the mechanical equilibrium. Stresses are developed during this process which influence the movement, reorganisation, and other bio-chemical reactions altering the concentration of proteins within the cell. These structural and bio-chemical responses affect the ECM, which in turn act as stimuli for the cell. Thus, there is a continuous interaction between the cell and the ECM. In other words, the behaviour of cells depends on the properties of ECM, and vice-versa. Hence, in order to predict the response of cells, it is insufficient to study cell as an independent body. The *in vitro* studies should therefore include the combination of cell and ECM by allowing their interactions to influence each other.

2.2. Cell composition

The eukaryotic cell, as shown in Fig. 2.1, contains a well defined plasma membrane, cytoplasm, nucleus, endoplasmic reticulum and other sub cellular components, whereas prokaryotic cells are devoid of nucleus.

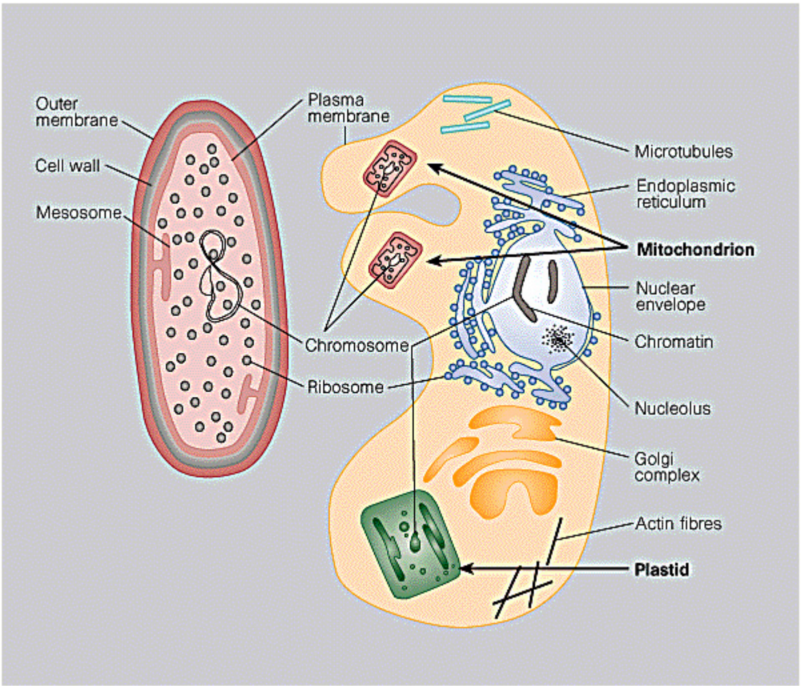

Fig. 2.1: Schematic of a Prokaryotic (left) and Eukaryotic (right) cell [19]. Cells are made up of many organelles, involving many bio-chemical reactions, making it a very complex material to understand.

Some of the important components of a cell, and their functions are:

- Plasma membrane or cell membrane separates the interior of the cell from the external surroundings. It is made of lipid bilayer with embedded proteins. It is mainly responsible for selective permeability of ions and adhesion of cells to ECM. Cell membrane-ECM bond occurs mainly through the focal adhesion proteins such as integrin, and vinculin.

- Cytoplasm is inside the cell membrane. It is made up of gel like substance called cytosol. In prokaryotes, all components of the cell are present within the cytosol, whereas in eukaryotes, components within the nucleus are separated from the cytoplasm by a nuclear membrane. The gel like substance consists of protein filaments, soluble proteins, and mainly water.
- Cytoskeleton forms the internal skeletal structure of cells. They provide structural stability, helps in motility, cell division, contractility, and also in mutation. It is made up of actin filaments, microtubules, and intermediate filaments. Actin filaments formed by polymerisation of actin proteins form contractile bundles necessary for movement. Microtubules are formed by the the proteins tubulin forming a cylindrical tube that helps in the transport of proteins within the cell. It also helps in cell division and motility. Intermediate filaments are made up of multiple proteins and are found to play a major role in the integrity of the cell.
- Nucleus, present only in the eukaryotic cell is the control centre. It contains most of the genetic material and provides instructions to other organelles based on the stimuli received. Recent experiments [20, 21] show that nucleus also contributes to the mechanics of the cell.

2.3. Cell physiology

Irrespective of the type of the cell, several activities take place within the cell to survive. Some of the important processes that occur are membrane transport, cellular respiration, DNA replication, cell division, protein synthesis, adhesion, and cell motility and contractility.

- Membrane transport : This occurs through the cell membrane, as it controls what enters and exits the cell. The process can occur in two ways, passive transport and active transport. In the passive transport, ions move from higher concentration to lower concentration through diffusion while in the active transport, they move from lower concentration to higher concentration in the presence of ATP molecule which is a source of energy, that facilitates such movement.

- Cell division : This process occurs either to reproduce, grow, maintain or repair the cells. In eukaryotes, cell division can occur in two types, mitosis and meiosis, while in prokaryotes, cell division occur through binary fission. Mitosis results in a daughter cell that is genetically equivalent to the parent cell, meiosis is a reproductive cell division in which the number of chromosomes in the daughter cell is reduced by half, and binary fission is a type of asexual reproduction where the cell divides into two.

- Cell signalling : This process is one of the basic activities that govern the actions of cell. Cells should be able to perceive signals from the micro environment in order to function and respond to stimuli. Cell signalling can be classified into mechanical and biochemical based on the type of stimuli. The process of signalling also exists between cells, through the cell-cell contacts.

In addition to the above there are other physiological processes that occur in the cell resulting in the movement of the cell. In this thesis, cell adhesion, and cell contractility and motility are considered, and are described in detail in the following sections.

2.4. Cell motility and contractility

Motility is the term commonly used in biology for the motion generated by forces within the body. In this regard, cell motility refers to the motion of cell due to forces generated by the cytoskeleton. Cell motility, responsible for various processes such as wound healing [22], inflammatory responses [23], and also involved in the spread of tumours [24], can occur in two ways, swimming, and crawling [25]. For example, fibroblast cells on skin crawl while sperm cells swim. Cell motility by crawling is understood to occur in three stages [26]:

- Upon sensing the stimuli by integrins, actin filaments, in the presence of myosin starts polymerising in the direction of the external signal. This leads to protrusion of the leading edge of the cell membrane which behaves dynamically according to the signal.

- Subsequently, adhesion molecules found on the cell membrane starts attaching itself to the substrate, preventing the cell from retraction.

- As the cell attaches at the leading edge, it releases the attachment at the trailing edge, mainly because of the contractile forces produced in the actin filaments. These

> contractile forces are then responsible for the movement of the cell in the direction of protrusion of the leading edge.

It can be seen that during the process of cell motility, contractile forces are generated, resulting in cell contraction. Cell contraction is one of the major reasons for the continuous reorganisation of the cytoskeleton, which depends on the external force. Thus, in order to understand the process of cell motility, it is necessary to understand cell contractility.

Actin filaments, present in cytoskeleton are responsible for cell shape and contractility on the cellular scale [27]. They can be very well organised and stably structured as in muscle cells or highly dynamic and constantly restructured as in non-muscle cells [28–30]. They are connected to each other by $\alpha-$actinin proteins to form actin bundles. These bundles are cross linked by Myosin-II proteins forming stress fibres (SF). Thus, the formation of stress fibres through actin-myosin cross bridge complex results in the contractility of the cell.

Other parts of the cytoskeleton, microtublues and intermediate filaments also contribute towards cell motility. But, in case of contraction dominated model of cell motility occurring in the crawling cells, microtubules acts as an anchor and contributes passively to the motility. Hence, in this study, only actin-myosin stress fibres are considered to influence the active component and microtubules for the passive component.

Based on the sub-cellular locations, stress fibres are classified into three types; (1) ventral stress fibres, (2) dorsal stress fibres and (3) transverse arcs, as shown in Fig. 2.2(left). Ventral stress fibres, the most common stress fibres within a cell, originate and terminate at cell membrane-ECM junctions. Dorsal stress fibres are attached to such junctions at one end, while transverse arcs are found to disassemble near the nucleus of the cell.

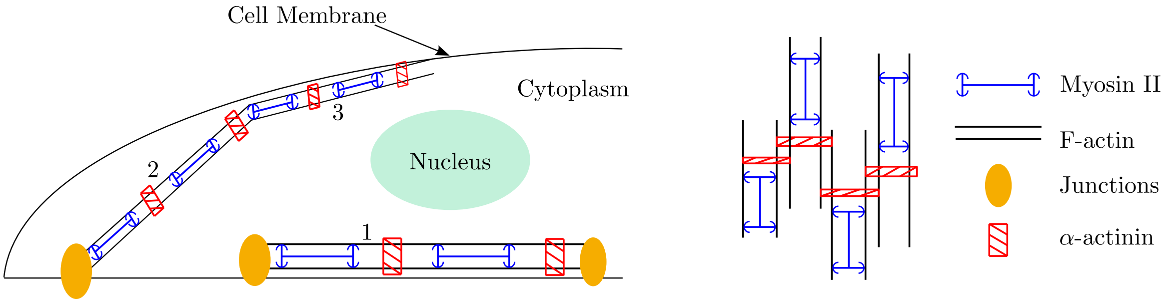

Fig. 2.2: (left) types of stress fibre: ventral stress fibres (1), dorsal stress fibres (2) and transverse arcs (3). The stress fibres are classified based on their location, their chemical constituents remain the same; (right) cross-bridge between α-actinin, F-actin, and myosin II.

It is assumed that, due to structural similarities, transverse arcs contract like muscle sarcomeres, while dorsal stress fibres do not behave like contractile structures. Ventral stress fibres which are connected to the cell membrane at each ends were found to build up tension along the structure, through the actin-myosin bond as shown in Fig. 2.2(right). It has been found that even though the process of contraction of ventral stress fibres is different from that of muscle sarcomeres, growth of tensile force was similar.

2.5. Focal adhesions

Ventral stress fibres, from now on referred to as stress fibres, extend along the length of the cell and end on the cell membrane. The junctions where stress fibres connect to the cell membrane are termed focal adhesions (FA) [31]. The FA junction consists of around 150 types of proteins [32], as shown in Fig. 2.3. Integrins are present at the bottom most layer, forming a connection with the extra cellular matrix. In between the integrin and actin cytoskeleton, FA proteins such as paxilin, vinculin are present, extending to a length of 40nm [33].

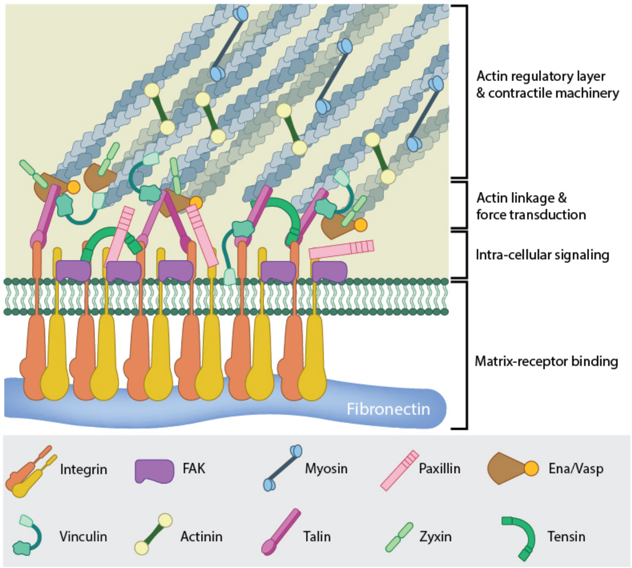

Fig. 2.3: Focal adhesion proteins: Integrins form the connection with the ECM, consisting of fibronectin. Different proteins such as paxilin, vinculin are found in the area between integrins and actin stress fibres, resulting in transfer of signals from ECM to cell, and vice-versa [34].

Integrins are the mechanosensitive proteins present at the bottom layer of FAs that perform the job of developing the required connection between an actin cytoskeleton and the ECM [35]. Cells are found to decay if they are not adhered to the substrate. Thus, the behaviour of FAs developing causes the difference between life and death of a cell [34]. The growth of FAs is not an independent phenomenon. It is affected by the growth of stress fibres and vice versa, making it highly dynamic in nature. The connection between stress fibres and focal adhesion therefore becomes prominent in maintaining the equilibrium. The schematic of a cell consisting of stress fibres within cytoplasm and focal adhesion represented by focal adhesion is shown in Fig. 2.4.

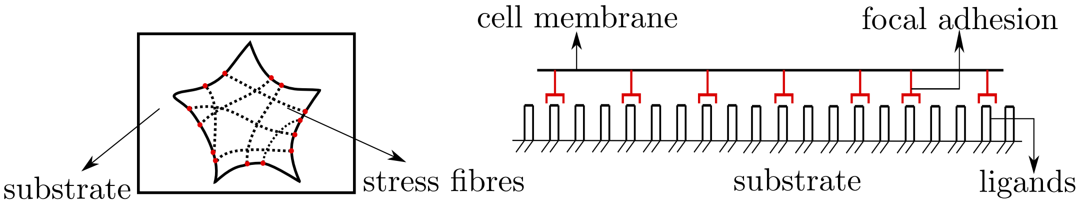

Fig. 2.4: Stress fibres and focal adhesions: Stress fibres extend from one end of the membrane to the other, and end at focal adhesions. Focal adhesion develops the contact between cell membrane and substrate ligands.

FAs not only transfer the stresses generated in stress fibres to the ECM, but also probe the properties of the substrate, the cell has attached to. When cells are attached to an adhesive substrate, the bonds formed at FAs result in the activation of signalling cascade, while on a non-adhesive substrate, cells degrade and die with time. Although the exact nature of force sensing by FAs has not been understood yet, it has been generally observed that by increasing the force acting on the cell, the adhesions are reinforced [34].

2.6. Mechanotransduction and feedback

Focal adhesions, due to the activity of mechanosensitive proteins, generate biochemical signals within the cytoplasm. This process of conversion of external mechanical force into biochemical signals, causing changes to the cytoskeleton, and developing internal forces is termed mechanotransduction, as shown in Fig. 2.5. Though, the exact processes involved in the conversion of mechanical force to biochemical signals are not perfectly understood, stimuli sensed by integrins result in opening up of ion channels. This leads to changes in the concentration of different chemicals in the cytoplasm, causing chemical reactions [36], which develops forces within the cell, as shown in Fig. 2.5.

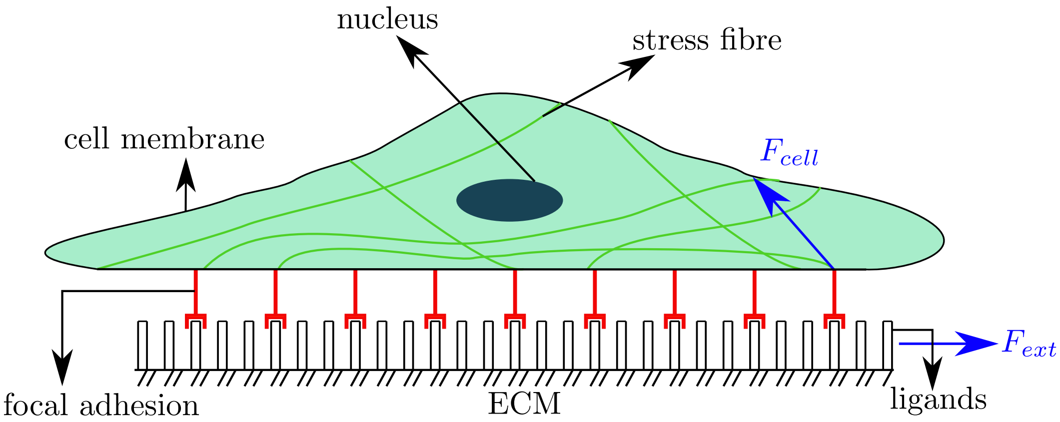

Fig. 2.5: Transfer of external force (F_{ext})to cytoskeleton (F_{cell}) through focal adhesions. Nucleus and other organelles are present in cytoplasm.

The process of mechanotransduction is not a one-way activity. External stimuli causing the bio-chemical reactions in the cytoplasm lead to changes in the mechanical equilibrium of the cell, and thereby develop stress fibres. In order to maintain the equilibrium along the cell membrane, stresses are transferred to the ECM through FAs. Growth of FA, which is connected to the ECM, further acts as stimuli, leading to a reaction cycle, as shown in Fig. 2.6. This constant interaction, a positive feedback, is necessary for the healthy behaviour of a cell. Absence of a feedback loop leads to lack of contact between stress fibres and focal adhesion, causing dissociation of focal adhesion proteins and thereby cells get detached from the ECM resulting in cell death or apoptosis.

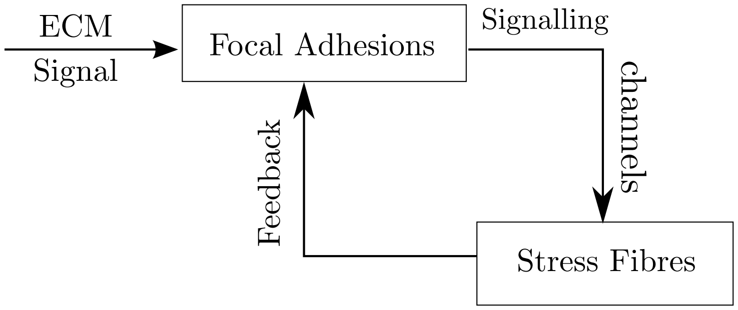

Fig. 2.6: Feedback loop present in cellular mechanotransduction. Stimuli experienced by the cell from ECM is sent to the cytoplasm through the focal adhesion. This leads to signalling induced bio-chemical reactions forming contractile stress fibres, further affecting focal adhesion concentration and thereby completing the feedback loop.

2.7. Computational modelling

As we understand, cells are the building blocks of living organisms. The mysteriously complex processes performed by living bodies originate in cells. Hence, there is a need for a specialized tool, which can delve deep, and be of help in understanding the mechanisms behind cellular functioning. One of the tools present for such an understanding is computational modelling. By computational modelling, it means to develop mathematical models describing the observed processes and solving the system of equations thus generated, using computers. With the advent of better processing hardware and software over the past few decades, very large and complex problems can be solved with relative ease. Computational models, thereby, help in understanding the biology in many ways:

- They can be used as virtual experiments, where the system to be tested can be changed by just changing the parameters. This would hence be equivalent to performing a physical experiment on a different specimen.
- Various hypotheses can be tested in order to understand the processes involved in a mechanism.
- Experiments can be designed, based on the results obtained from computations.
- They can also be used as post-processor for experimental observations.
- They can be used to perform studies by isolating sub-cellular structures.

In order to develop an efficient computational model, various assumptions have to be made. Though, these assumptions usually make the system simplified or sometimes over-simplified, it would be sufficient to simulate the physics governing the mechanisms. Models can be built based on different concepts of physics, numerical algorithms, length or time scales, or a combination of these. A set of such a combination might be highly efficient for a particular problem, but might become inefficient for others. Some of the models use multi-scale approach building stress fibres from individual proteins, while others model whole cell in an average sense. Following the understanding of influence of mechanics on cell behaviour, many mechanics based models have been developed assuming cell as a viscous fluid, or as a deformable solid and sometimes as a porous material with solid-fluid interfaces. Many numerical techniques of modelling such as discrete and continuum approaches using different numerical algorithms such as finite element method, finite volume method and stochastic schemes have been followed for different problem cases.

2.8. Literature review

Since the discovery of cell by Robert Hooke in 1665, there has been a tremendous amount of research effort invested in understanding its internal composition and their functions. Cells, being the fundamental units, are responsible for various behaviours of living beings. Living cells consume energy, either to keep their motion or to change their shape and structure by reorganising the internal cytoskeleton [37]. Furthermore, it has been found that external mechanical forces contribute to the reorganisation of the internal cytoskeleton and thereby control its behaviour [4, 16, 37, 38]. Mechanical loading experienced by cells induces strengthening of bones [14], while forces are generated in muscles. For example, heart muscles have to generate forces throughout the life span of an individual, while some muscles such as those in arms or legs generate power only during certain activities, such as movement or weight lifting [39].Thus, the influence of mechanical forces in maintaining the behaviour of cells and tissues has made it necessary to understand the mechanisms involved, helping in finding a cure for many deadly diseases.

It has been widely agreed that the stimuli induced biochemical reactions occurring within the cytoplasm cause contractility of actin filaments, generating necessary tensile force, thereby regulating the shape and structure of the cell [27]. Due to the developed tension within cytoskeleton, long and straight bundles of microfilaments appear, which crosses the length of the cell, and end on the cell membrane, termed stress fibres. It was found that stress fibres were the contractile structures responsible for maintaining the tensile force within the cytoskeleton [40]. Many detailed studies were performed to observe the structure of stress fibres in order to understand how forces developed within them. It was observed that, actin filaments present in the cytoplasm bundled in the presence of non-muscle myosin and were held together by the actin cross linking protein $\alpha-$actinin [41, 42]. Contractility of such stress fibres was modelled to be similar to that of muscle sarcomeres [43, 44]. In a sarcomeric model of stress fibre contraction, it was assumed that the arrays of myosin would slide between the arrays of actin filaments, resulting in contraction, as shown in Fig. 2.7(a).

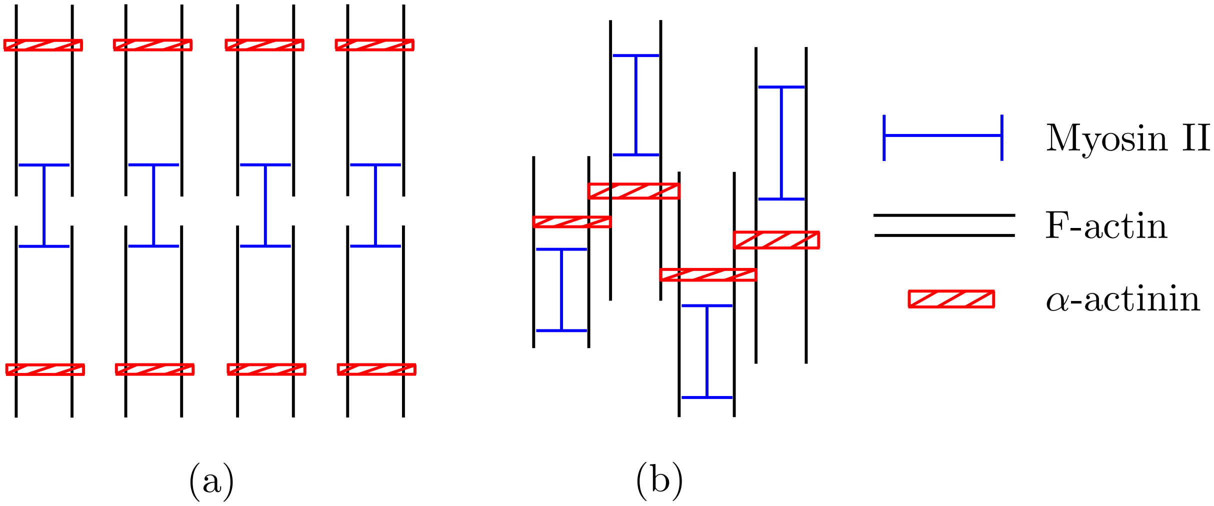

Fig. 2.7: Actin structures are held together by α-actinin and cross linked by myosin. (a)Sarcomeres: During contraction, myosin slides between the filaments. (b)Stress fibres : α-actinin acts as a blockade for the movement of myosin, requiring the rapid dissociation and association of α-actinin for contractility.

But, the polarity analysis, where the analysis of shape of terminals present in actin filaments is performed, showed that this model of contraction was not possible in stress fibres [42]. In addition, it was also found that, in stress fibres, $\alpha-$actinin acted as a blockade for the movement of myosin filaments, as shown in Fig. 2.7(b). Thus, the mechanism allowing stress fibres to contract would involve rapid dissociation and re-association of $\alpha-$actinin to actin filaments [45]. It was also observed that the stress fibre contractility was mainly due to the increasing myosin contractility rather than increased actin polymerisation [46]. It was found that the forces developed in stress fibres due to contractility affected not only the physical behaviour but also the cellular signalling and gene expression. In addition, it was observed that, blocking such cell-generated forces would affect proliferation, differentiation, and other basic cellular functions [47] and that the changes occurring in the cell due to changing stiffness of the extracellular matrix is similar to that obtained by directly changing cell contractility [48, 49]. Hence, the contractility of stress fibres, leading to the growth of tensile force, plays a major role in mechanotransduction.

As another part of mechanotransduction, cells have the ability to sense the properties of ECM. There are a variety of mechanisms developed to understand how cells sense its surroundings, and respond to them [50]. One of the very prominent sub-cellular site for sensing mechanical properties and forces are focal adhesions (FA). The FAs attach the region of the cell to the substrate while needed, and detach while not necessary [26, 51].

Integrins, the mechanosensitive proteins present at the bottom most layer of FAs act as sensors by responding to cues from the ECM, along with other kinases, phosphatases, and adaptor proteins. Integrins are found to exist in two states: a high affinity state where they can form a bond with the substrate, and a low affinity state where they cannot form a bond [52], as shown in Fig. 2.8.

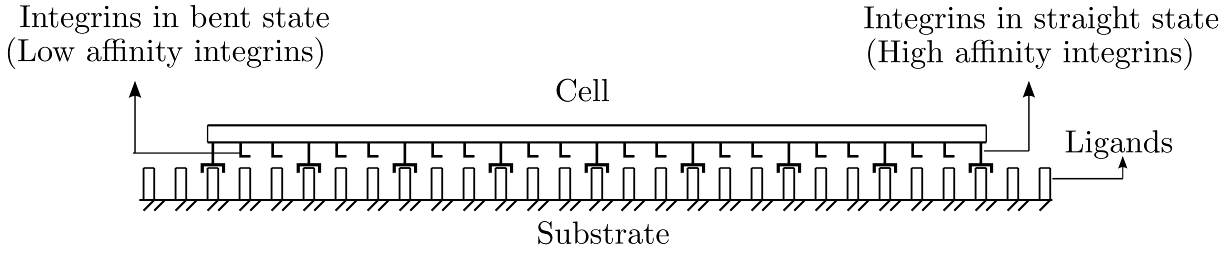

Fig. 2.8: High and low affinity integrins. High affinity integrins can form a connection between the cell and the substrate, while low affinity integrins cannot bind to the substrate. cf[53].

In this regard, when an external force is applied to the cell, the high affinity integrins in contact with the ECM, sense the force and transfers it to the cytoskeleton. Simultaneously, when a region of the cell releases contact with the ECM, high affinity integrins are converted to low affinity ones. At FAs, multiple protein-protein interactions occur, allowing the cells to sense various types of signals leading to a complex behaviour [54]. Amongst several plaque proteins present at FAs, integrins, vinculin, talin, paxilin, and tyrosine phosphorylated proteins are highly characteristic [31]. It has been found that, by using magnetic tweezers and a twisting device, mechanical deformation of one of the FA proteins leads to global cytoskeletal rearrangement [36]. Thus, FAs, either by sensing the properties of the ECM or the external force, alter the properties of the cytoskeleton by forming stress fibres through actin-myosin bonds, which creates a positive feedback loop by affecting FAs in response. In addition to FAs and actin-stress fibres, recently it has been discovered that even nucleus plays a role in mechanotransduction through LINC complex, which is involved in chemical signal transduction pathways [20, 55].

In order to observe the intricate processes occurring in the cell, and to understand the involved mechanisms, there have been several types of experiments designed. Because the time and length scales of the bio-chemical reactions and biological structures, respectively, might be different, a single experimental device or technique is unable to observe all the desired behaviours. Some of the experimental methodologies measure collective properties of a group of cells, while some are able to track individual cells. One of the classifications of experimental techniques is based on the applied force: force-application techniques, where force is applied onto a cell and the mechanical response is recorded, and force-sensing techniques, where cells are seeded onto deformable structures and traction forces are measured [56]. Another classification can be made based on the area of deformation of the cell under study: mechanical loading of an entire cell, deformation of a portion of the cell, and mechanical stretching of a population of cells [38, 57]. Some of the popular experimental techniques used to measure the mechanical properties of cells are:

- Micropipette aspiration : This technique is used to study the whole-cell mechanics where the cell solution is pulled into a glass pipette by the application of a negative pressure. Based on the amount of cellular material that has entered the pipette, its material properties can be estimated, in case of red blood cells [58] or leukocytes [59].

- Atomic Force Microscopy : This technique is used to study the mechanical properties of the cell by deforming a portion of the cell surface. A sharp cantilever is used to apply a pre-fixed force and the deformation is measured. It has been widely used in measuring the properties of cell, focal adhesion, and cytoskeleton [60–62].

- Substrate strain : This technique is used to measure the mechanical properties of cells based on their collective response. Cells are cultured on top of an elastic membrane, which is subjected to strain. The cellular deformation is measured and the properties are evaluated. It has been used to study actin reorganisation [8], and cell motility [63].

- Traction Force Microscopy : This technique is used to measure the traction force exerted by the cell in a quantitative manner. Cells are seeded on a substrate along with the beads. Based on the deformation of beads, traction forces can be evaluated. It has been used to measure forces at focal adhesions [64], and to determine the effect of cell shape on the exerted traction [65]. With advancements in fabrication and optical technologies, over the past few decades, there has been a priority on experiments that can quantify mechanotransduction, by observing the response of cells to different topographies. The process involves fabricating patterned substrates or micropillars upon which cells are seeded. In case of substrates with micropillars, the pillars behave like a cantilever beam, which undergo deflection due to the traction force exerted by the cells. Knowing the material properties of the pillars, the force exerted by cells can be evaluated. This method has been successfully used to measure contractile forces and to study the role of cell spreading [66], and also used to study the force generated by focal adhesion growth [67]. The response of cells are found to depend on the nanotopography of the substrate as well [68].

In addition to understanding the contractile nature of stress fibres, there have been a few experiments to understand how focal adhesions grow and form a bond with the substrate. Studies have dealt with, how shape of the cell dictates the growth of focal adhesion [69], and how an external force can control the focal adhesion growth [70]. Experiments have been performed on different types of cells which have exhibited similar behaviour but with different time scales [8, 71, 72].

Experiments are being performed to understand the response of cells to applied external mechanical loads. Specifically, these experiments are designed to understand the interaction between the cell and the substrate, and how different types of load affects stress fibre and focal adhesion growths. Cells are seeded on a biocompatible elastic substrate, usually polydimethylsiloxane (PDMS), upon which cells develop focal adhesions, and bind to the substrate. Through FAs, cells can sense the stiffness and the loading applied to the PDMS substrate. Cells, thus experiencing the loading, respond by reorienting the actin bundles in such a way that it reaches an optimum condition where either the strain it experiences is the least [8], or the stress it experiences is the least [73], or the passive stored elastic energy is minimum [74]. It was found that such a reorientation was highly dynamic, and strongly depended on the geometry of the substrate [75]. It was also observed that when cells were placed on a soft substrate, the reorientation was not as high as the one observed when placed on a stiffer substrate, exhibiting the influence of substrate stiffness on the cell behaviour [8, 76]. When a static loading was applied, the orientation of stress fibres was found to be parallel to the direction of loading [77], while, when the cells were subjected to a uniaxial cyclic loading, they reoriented in a direction away from the direction of loading, exhibiting strain avoidance [78, 79]. The degree of reorientation was found to correlate with the amplitude and frequency of the cyclic loading [7, 8]. An interesting observation was made where the reorientation was also found to depend on the shape of the waveform being applied [7]. A contrasting behaviour was observed when cells were cultured in a 3D matrix or a gel, where even when a uniaxial cyclic loading was applied, cells were found to orient along the direction of loading [80].

In order to bolster the experimental observations by numerical modelling of cellular mechanotransduction, two approaches have been generally followed: to go up the scale by modelling the sub-cellular components and its influence on each other, or by modelling the behaviour of whole-cell itself. As reviewed in [34], mechanotransduction process involves different mechanisms with varying time scales. Over the years, it has been observed that by varying the experimental conditions, the time taken by the cell to detect changes in the surroundings and respond changes. There is no strong consensus on the distance over which the signal from the cell propagates, and hence the exact nature of the response of the cell under an external stimulus is still unclear. Some experiments suggest that the forces developed during the actin-myosin bond formation is influenced by the stiffness of the substrate and involves individual proteins present at the FAs. In such cases, the proteins can probe the mechanical properties of the substrate in sub micrometer range only [81, 82]. But other experiments and theories suggest that the mechanosensitive channels coupled to the FAs can induce faster response to the mechanical properties, but at a length scale larger than that involved in the protein theory [83, 84]. There are other theories backed by experiments which strongly suggest that, sensing substrate mechanical properties by the cell is a global mechanism and hence involves a length scale of magnitude comparable to the length of the cell, rather than a local mechanism just at the FAs [85]. These mechanisms also suggest that the stress fibres may act as a force sensor which has a time scale of minutes, during which it can transfer the stresses to the FAs. Thus, different experiments leading to different results about the time and length scales have led to building up of different numerical models, which can be classified into 3 types [34].

1. Molecular models: In such models, individual ligand-receptor bonds are considered. Based on its response to external stimuli, the cellular behaviour is predicted [86, 87].
2. Condensation models: Here, the clustering of proteins at FA site is modelled, and hence it can explain the stress transfer between the ECM and the cellular proteins at FA [88, 89].
3. Cellular scale models: In these models, stress fibre formation within the cell and the stress transfer between the cell and the ECM at FAs are modelled [12, 53, 90].

There have been different approaches followed to model the cytoskeletal network in the stationary cells. Cell contractility was modelled by assuming cell as an elastic medium [91], as a discrete set of elastic filaments [92], as a interlinked structure of passive filaments [93, 94], but all these models neglected biochemistry of its formation. Since FAs play an important role in mechanotransduction, several models have been developed to simulate FA growth only. One of the assumptions made in developing numerical models for FA was that, in the absence of forces, the ligands, which are the signal transmitting proteins, are attached to the adhesion site by the attractive force between the ligands and the corresponding receptors [95]. This model suggests that, by stretching the ligand bonds, the stored elastic energy also increases resulting in the distortion of FA. Some of the classical models that have been developed for modelling FA includes the rate reaction theory [96], cohesive zone approach [97], and considering the role of binder mobility in the developments of adhesive contacts [98]. Some of the models were built on mechanical and thermodynamic aspects of the FA growth without considering the influence of external forces on bio-chemical signalling [52, 88, 99], while the positive feedback present between cell contractility and FA growth has been modelled using kinetic equations [100]. Recently, models have been suggested with catch-bond mechanism for FA bonds, providing a multi-scale approach to cell contractility [101, 102]. In addition to the FA, force generation in stress fibres through cell contractility has been modelled as well. It was observed that force generation in stress fibres was similar to muscle sarcomeres, whose contractility behaviour have been investigated in detail [103, 104]. But, stress fibres being more dynamic and disordered compared to muscle sarcomeres, theories have been developed to predict different dynamical states of the stress fibres [105, 106]. The discrete model of tensegrity [107, 108], and the cellular solid model [94] were developed to model the tensile nature of the cytoskeleton, while [90] considers non-equilibrium thermodynamics for modelling the cytoskeletal force generation. Some models have even been developed specifically to validate against a particular type of experiment, such as AFM indentation, optical tweezers, and micropipette aspiration [109–111]. Recently, many continuum level models have been developed to explain stress fibre contractility [11, 112–115]. In addition, there are a few models which couples the focal adhesion growth with stress fibre contractility [53, 116], while a few even include the feedback loop for the calcium signalling which dictates the stress fibre growth [12, 117]. The continuum models [10, 12] have shown the phenomenon of stress fibre reorientation due to uniaxial cyclic loading applied to the attached substrate. Some of the models have also shown the influence of geometry of the substrate on cellular behaviour [118]. Statistical mechanics based models have been developed, which can simulate the contrasting behaviour of stress fibre growth in 2D and 3D environments [114]. Some of the models consider cell as a fluid [119], while some consider it as a solid body [12, 53], and some assume cells to be a porous material with fluid-structure interactions [10, 113]. Research is also being performed on modelling the

FA-ECM bond, which controls the behaviour of cells [87, 120, 121]. Some models have been developed to consider the effect of nucleus on mechanotransduction, including the interaction between cytoskeleton, and nucleus [21, 122].

Even though most of the continuum or discrete models developed to simulate SF coupled with FA growth involves a set of differential equations, little effort has been made on studying the solution schemes. Most of the current models use commercial finite element packages to solve the involved coupled differential equations. Since the models involve coupling different sub-cellular structures, the overall model becomes either a multi-physics or a multi-scale problem. In this regard, it is very important to have an understanding of how the solver treats the coupled system, and which algorithm is followed in solving it. In the field of fluid-structure interaction, a number of well documented research exists that addresses carefully the numerical aspects [123, 124] of the multi-physics problem, including biomedical applications [125, 126]. But, in the field of cell mechanics, there has been a little effort in understanding the numerical aspects in order to develop a robust numerical scheme that can provide accurate and reliable solutions. Thus, equations leading to a multi-physics problem can be coupled following either a staggered or a monolithic approach. In this regard, the model [12] has been solved following a monolithic coupling, while [53] has been solved following a staggered approach. A detailed comparison of monolithic and staggered approaches for the problem of stress fibre-focal adhesion growth has been carried out in [13].

3. Cyclic loading experiments on cells

Due to the complexity of cell physiology, mechanotransduction experiments rely on developing *in vitro* techniques with *in vivo* type stimuli in order to understand the nature of the response of cells. One of the fundamental studies in understanding the cellular response is to investigate the dynamics of mechanotransduction by the application of dynamic load. Thus, *in vitro* cell stretching assays, where the cyclic load can be applied to a membrane upon which the cells are cultured, form an important class of experimental device. The underlying principle is that cells experience the applied mechanical loading and respond based on its magnitude and direction. In this chapter, a DIY design of a device that can apply the uniaxial cyclic load to cells, cell stretcher, is developed. Using the additive manufacturing process to manufacture the device makes it highly cost effective. Experiments are performed on fibroblast and osteoblast cell types and the results are quantified using statistical measures.

3.1. Mechanical stimuli to cells *in vitro*

The concept of *in vitro* mechanical stimulation to study cell behaviour has been used for many decades [17]. Traditionally, micropipette, atomic force microscope, and tweezers have been used to study the cellular response to mechanical stimuli, and thereby evaluate the mechanical properties of cells. Various loading systems were designed to apply the preferred mechanical stimuli; compressive loading systems, longitudinal stretch systems, substrate bending systems, and fluid shear systems [127]. In addition, devices have also been built specifically to stretch the cells cyclically. Many custom-made devices have been developed over the years, following different actuation technologies, reviewed in [128]. Pneumatic actuators are widely being used to stretch the membrane upon which the cells are cultured. This method demonstrates to be the most sterile way of stretching because of the lack of direct mechanical contact with cells and other parts of the device [129], which has been used even for 3D stress fibre remodelling experiments [130]. Another popular actuation technique is the electromagnetic actuator, where an electromagnet is used to control the displacement of the membrane [131, 132]. Servo and stepper motors are also used for uniaxial [133, 134] and biaxial loadings [18, 135], which happens to be the most popular method for reorientation experiments [7, 136]. Recently, commercial systems are available, using similar actuation methods, that promise to be adaptable for a variety of loading conditions, and boast well characterised strain profiles (FlexCell, Strex Inc., AS One International Inc.). With improvements in laser technology, optical actuators are being used to apply force directly on cells [137, 138]. Microelectromechanical systems(MEMS) have been developed for this purpose as well [139, 140]. Thus, overall, the cell stretchers have served as a mini gymnasium, wherein different types of loading could be applied on cells, and has served to be very useful in understanding the nature of their responses.

Even though the commercially available cell stretching devices can apply a variety of loading signals, the main drawback is that these devices are expensive. These devices are usually designed for specific microscopes in order to have the live imaging capability, and additional accessories are required to suit any other microscopes. Most of the custom-made devices act as a good alternative, but require a sufficiently large incubator space to place the device while it is running, as seen in [141], or require a custom made incubator [7]. Hence, there was a need to develop a device, which is compact and is capable of applying different cyclic loadings while maintaining a sufficient level of accuracy. In this regard, a very compact cell stretcher has been designed and manufactured using the 3D printing technology. The solution that has been presented is very easy to manufacture and highly cost effective.

3.2. Cell Stretcher : Design

The design of the cell stretcher had to satisfy the following constraints:

- Compact : The device had to be designed to be able to fit into the onstage incubator of the microscope system in the lab.
- Accurate : The device should allow for the precise evaluation of the strain due to the applied displacement.
- Assembly : The device should be easy to assemble.

- Imaging : The device should allow for the live imaging of cells.
- Loading : The device should be capable of applying a variety of loading patterns.
- Adaptability : The design of the device should be capable of being easily adaptable to any microscope system.

Most of the modern microscope systems come with an onstage incubator. Usually these incubators are small with a surface area of $100 - 200\text{cm}^2$ and a depth of $3 - 5\text{cm}$. Hence, by designing the cell stretcher to fit into such incubators, it would be possible to run the experiment under the microscope with the live imaging capability. The onstage incubator supporting the EVOS microscope system (Thermo Fisher), present in the lab, has a vessel holder with a dimension of 128mm X 86mm, which is the standard size for a 96-well plate. The cell stretcher was hence designed with these dimensions resulting in its fitting to any standard fluorescence microscopic system. In addition, the device also has constraints due to: 1) the limited working distance of the lens, and 2) the depth of the incubator chamber. Hence, care was taken to limit the height of the device to 5cm and the membrane upon which the cells were cultured to be placed within 5mm from the base of the cell stretcher. The base plate of the cell stretcher designed satisfying these constraints is shown in Fig. 3.1.

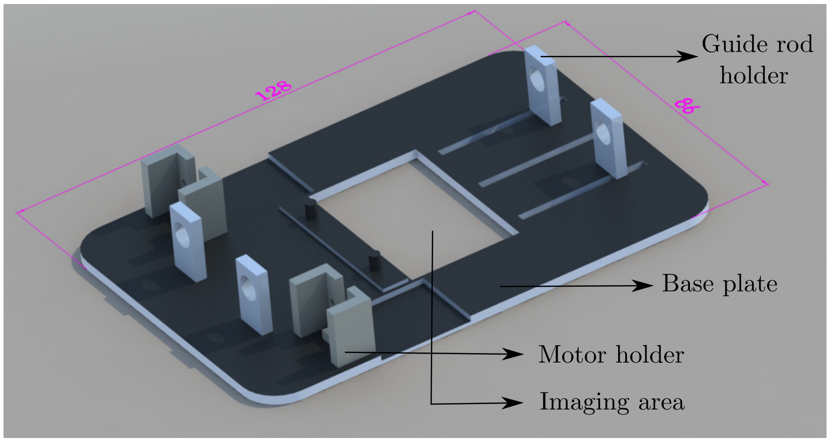

Fig. 3.1: CAD design of the base plate of the cell stretcher. It has a dimension of 128mm X 86mm, matching the size of a 96-well plate, in order to fit it in the incubator vessel holder.

The next step was to attach a mechanism for applying the cyclic stretch. In order to avoid the sinusoidal motion produced by the slider-crank [142], a simple nut-bolt combination was used. Since the pitch of the bolt is fixed, each rotation would hence displace the nut by the same amount as that of the pitch, making the device calibration process very simple. The rotation of the bolts was controlled using stepper motors regulated by Arduino Uno (Arduino). A micro metal geared stepper motor (12V, 0.6kgcm, PiHut) was chosen because of its small size and precise rotation control. The elastic membrane upon which the cells were cultured was fixed at one end while moveable at the other. The part which holds the moveable end of the membrane, has protrusions which fit into the grooves designed in the base plate of the cell stretcher, as shown in Fig. 3.2.

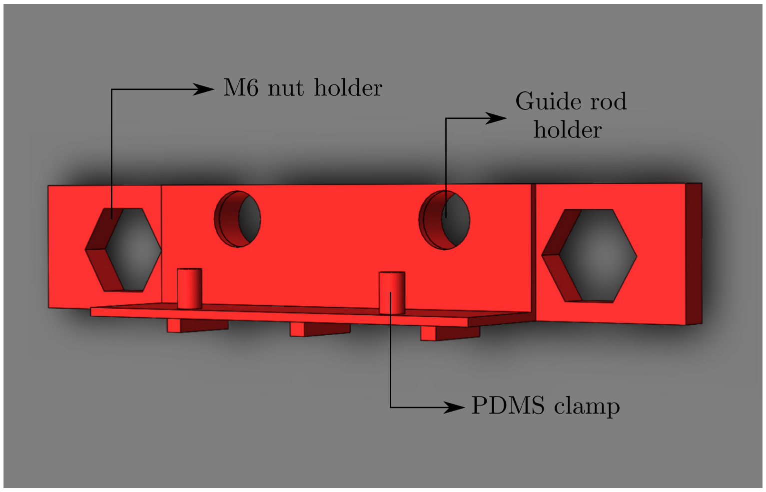

Fig. 3.2: CAD model of the membrane holder. It has extrusions to constrain the motion of the membrane. Pillars make the clamping and removal of the membrane easy and safe.

These grooves present in the base plate guide the motion of the membrane and keep it straight. In order to improve the accuracy of the stretcher, and prevent the out of plane movement of the membrane holder, steel rods were used as guides. The CAD model of the complete assembly is shown in Fig. 3.3, and the working[1] of the manufactured cell stretcher is shown in Fig. 3.4. The stl files of the design can be found at `https://www.thingiverse.com/thing:3343050`.

Assembly of the experimental setup before performing the experiments is very easy as well. The elastic membrane has to be fixed between the clamps, and steel rods are to be placed in their respective positions and screwed up. The assembly can then be placed in the onstage incubator and the motors can be switched on. With the help of an Arduino sketch, any loading can be applied, within the working range of the motor.

---

[1] Animation is played only in the electronic copy, and viewed with Adobe Acrobat Reader.

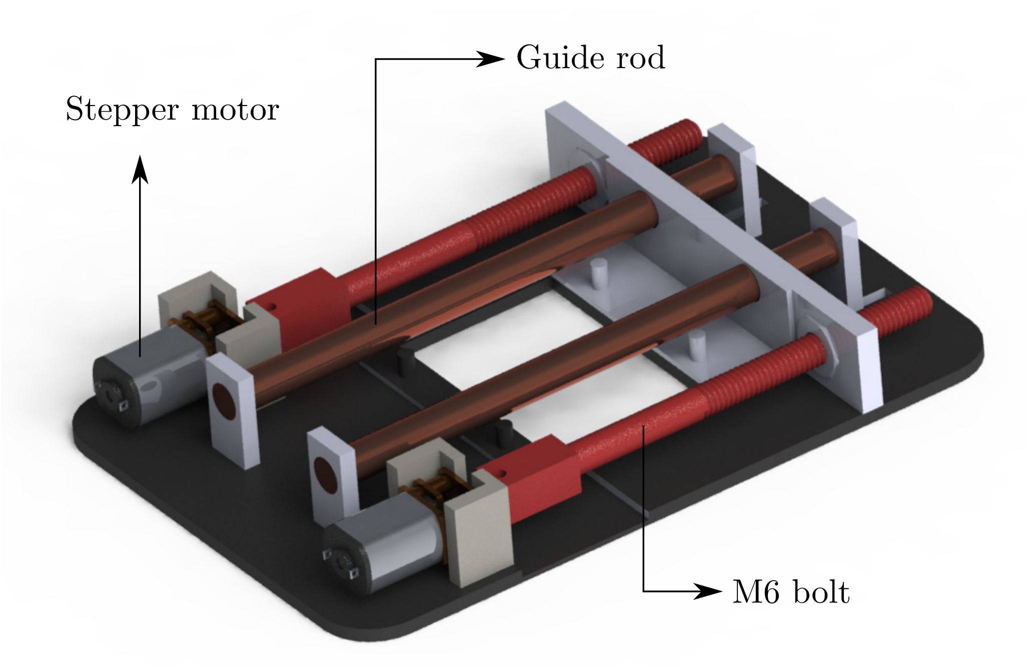

Fig. 3.3: Complete Assembly of the cell stretcher. Motors are connected to the coupler which in turn is attached to the screw.

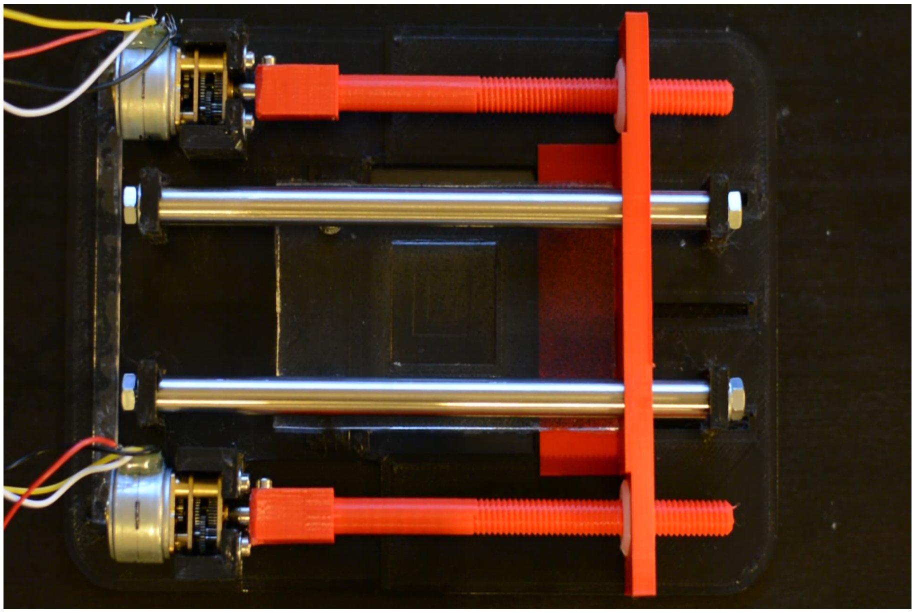

Fig. 3.4: Working of additively manufactured Cell stretcher. Polycarbonate is black in colour and PLA is red in colour.

3.3. Cell Stretcher : Manufacturing and calibration

The design of the cell stretcher explained in Sec. 3.2 was additively manufactured using the 3D printing technology. 3D printing is a cheaper and quicker alternative to testing the design, and manufacturing prototypes and functional parts. The printer used for this purpose was the Ultimaker 3 (Ultimaker), which is a fused deposition modelling (FDM) type printer. In this method of printing, a material, usually a type of plastic, is melted and deposited on a hot bed plate. To begin with, the CAD design is sliced into layers using a slicing software, Cura (Ultimaker), which outputs the coordinates where the molten material is to be extruded. Based on the settings that could be set in the software, such as temperature of the nozzle and the bed plate; percentage of infill, layer thickness, the quality of the print can be controlled. Materials used in the manufacture of the cell stretcher are polycarbonate (PC), and polylactic acid (PLA), properties of which are given in Appendix.

Calibration of the cell stretcher had to be performed in order to quantify the strain being applied to the cells attached to the elastic membrane. In order to measure the strain in the elastic membrane, a technique termed Digital Image Correlation (DIC) was followed. In this technique, the structure to be analysed is sprayed with a paint creating speckle pattern, to be used as a reference for measurement. In this regard, the membrane was sprayed with a black paint as shown in Fig. 3.5.

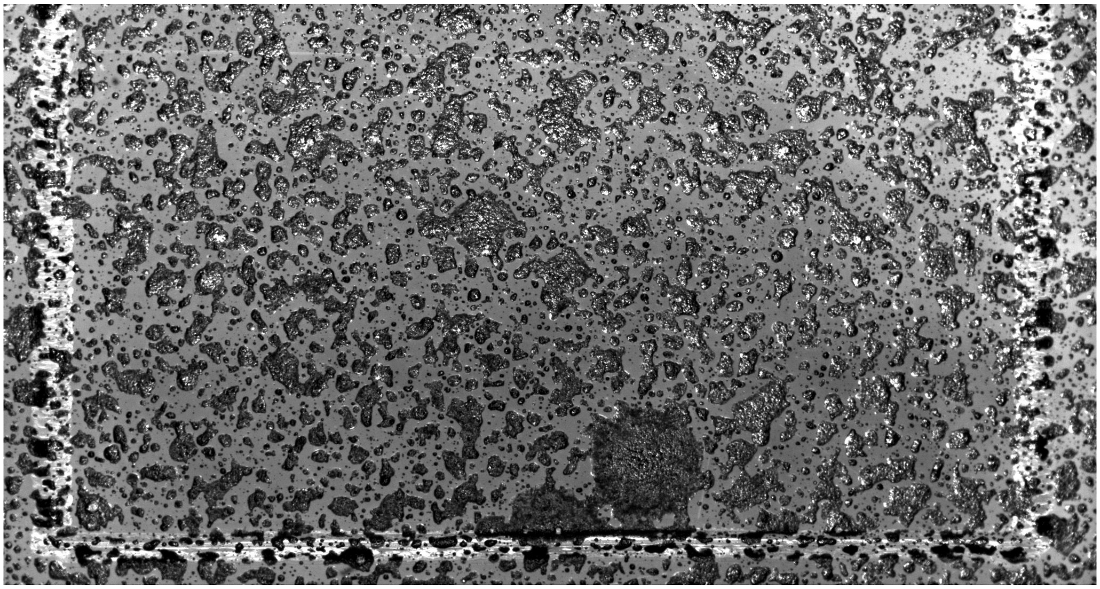

Fig. 3.5: Reference image of the membrane, sprayed with black paint for DIC. The speckle pattern plays a very prominent role in DIC. Size of the image is 11.2mmX5.9mm.

The stretcher is then connected to the Arduino and a required signal is supplied. A series of images, with a time interval of 1s between each image, was taken during the deformation of the membrane that could be correlated to the reference image and displacements, and strains can thus be measured. A digital camera (40mm WD, 1X, Edmund Optics) was used to image the membrane being stretched. A commercial package, GOM-Correlate (GOM) was used for the evaluation of displacements and strains. The images were fed into the software which measured the movement of particles in order to evaluate strains and displacements. Since, only the cells present at the central region of the well was chosen for the analysis, strain was measured in this region only. Strain (ε_{xx}) evaluated from DIC due to a 7.5mm stretch, as shown in Fig. 3.6 can be compared with the strain obtained by a linear analysis in the FE based analysis package Abaqus FEA (Abaqus.Inc), as shown in Fig. 3.7, both yielding a strain of 20%. A similar analysis performed for a 2.5mm stretch yielded 7% strain in the central region where cells were cultured. The thickness of the membrane fabricated, measured by focussing the microscope at the bottom and top layers, and evaluating the difference in their positions, was found to be 493.8(25.8)μm, and the Poisson's ratio evaluated as the ratio of ε_{yy} to ε_{xx} obtained from DIC was found to be 0.28.

Fig. 3.6: Strain distribution in the elastic membrane, obtained by DIC due to a 7.5mm stretch. The strain is plotted in the deformed image. It can be observed that strain is almost uniform in the central region of the membrane. Size of the image is 11.2mmX5.9mm. Values are expressed in percentage (%).

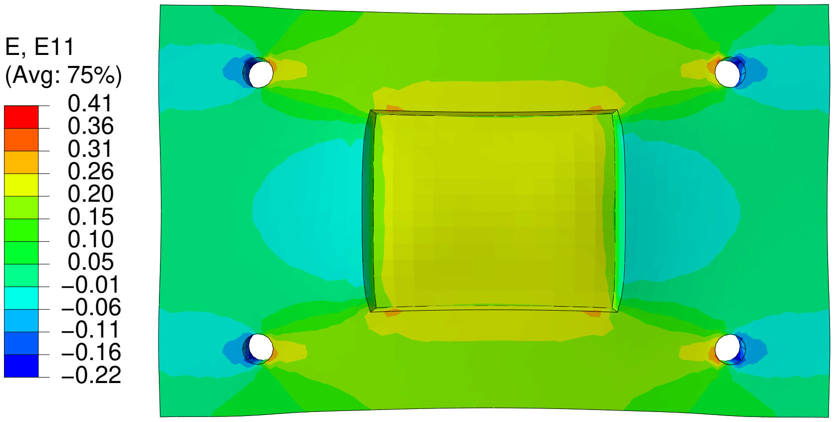

Fig. 3.7: Strain distribution in the elastic membrane, obtained by Abaqus analysis due to a 7.5mm stretch. The strain in the central region of the membrane can be compared with the strain obtained by DIC. Dimensions of the elastic membrane is 60mmX37mm.

Thus, strain in the membrane due to applied displacement could be characterised through DIC, which was validated by FE simulation as well. Strain appears to be uniform in the central region of PDMS, and hence cells cultured in this area experience same strain and therefore any cell in this area can be used for analyses.

3.4. Membrane preparation and cell culture

The elastic membrane used in the cell stretching experiments was the membrane made up of polydimethylsiloxane (PDMS). It is a silicon based organic polymer which is highly biocompatible with well characterised chemical and mechanical properties. It is an elastic material, which is found to be very useful in a variety of applications such as membranes for sensors, and biomedical studies. Various studies have been performed to quantify the mechanical properties of PDMS [143]. It is prepared by mixing the PDMS liquid and cross linking agent (Sylgard 184) in the ratio 10:1 by weight. A mould, as shown in Fig. 3.8, was 3D printed with PC material, on which the PDMS-cross linking agent mixture was poured and kept in the oven at 60°C for 8 hours. Supply of constant heat leads to PDMS being cross linked and forms an elastomer, as shown in Fig. 3.9. Due to the square shape extrusion in the central region of the mould, Fig. 3.8, a well was created in the PDMS membrane, Fig. 3.9, which can hold 1mL of cell media. This prevents the media spill during the cell stretching experiments.

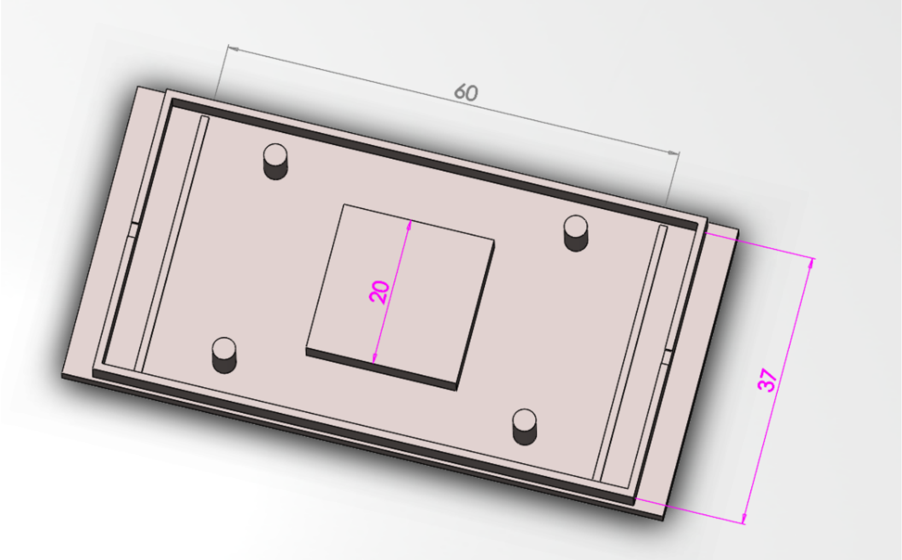

Fig. 3.8: CAD model of the mould used for fabrication of PDMS. It is 3D printed with PC, since it is stable even at very high temperatures. Central region has a square shaped extrusion, in order to create well in the PDMS.

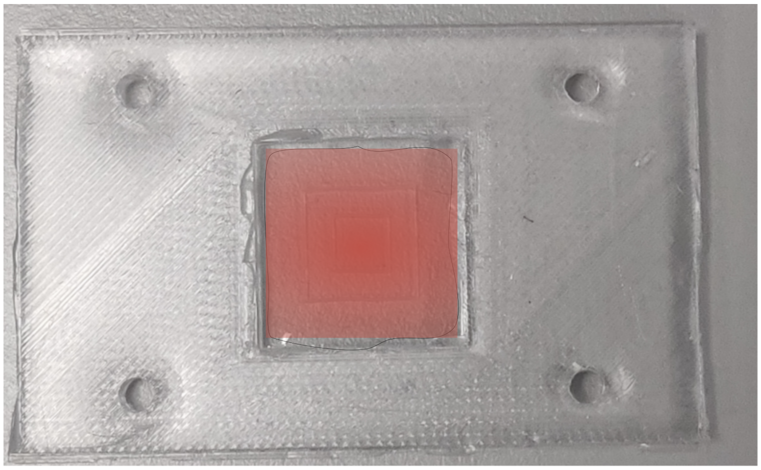

Fig. 3.9: PDMS fabricated by keeping it in oven for 8hrs at 60°C. Cells are cultured in the central well region, indicated by red colour.

PDMS by nature is hydrophobic, which is not a preferable environment for the cells to adhere and grow [144, 145] . Hence, surface treatment of PDMS has to be performed to make it hydrophilic, helping the cells to attach. In this regard, corona treatment of the PDMS surface was carried out, wherein a high frequency electric discharge changed its surface chemistry [146, 147]. The energy of the corona breaks the molecular bonds, and recombine with free radicals to form polar groups on the surface. These polar groups have increased surface energy in addition to a strong chemical affinity, improving adhesion of cells to the surface [148]. It has also been observed that, PDMS forms a nano glass-like layer on the surface due to corona degradation but cracked over time due to rubber nature of PDMS [149]. Contact angle measurements of water drops on the PDMS surface showed that corona treatment resulted in water drops to spread on the surface, which otherwise had high contact angles [147]. But, this hydrophilic character was found to be lost within hours. This process of loss of hydrophilic character of the PDMS surface is termed hydrophobic recovery, and the diffusion of uncured low molecular weight species particles (LMW) from the bulk to the surface is considered to be one of the prominent mechanisms causing this phenomena, Fig. 3.10 [146] .

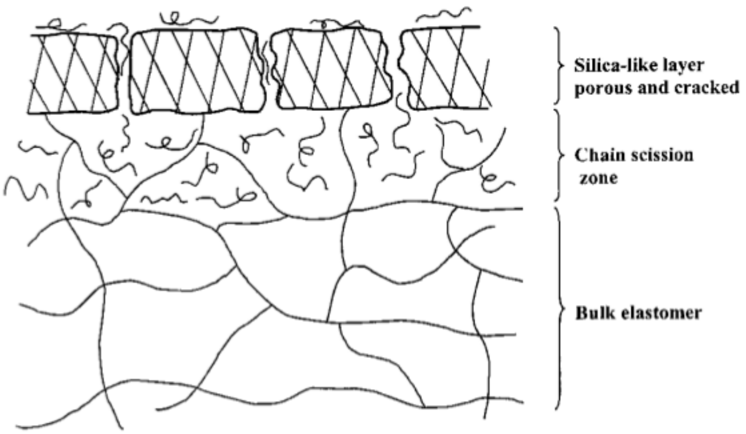

Fig. 3.10: Hydrophobic recovery is caused by uncured LMW species diffusing through the cracks to the surface of the PDMS [146].

One of the solutions for this problem is called thermal ageing, wherein the PDMS was de-moulded after 8 hours and placed back in the oven for another 48 hours, in order to cure all the LMW species [146]. Corona treatment following thermal ageing would then convert the character of the PDMS surface to hydrophilic, permanently. Then, the PDMS was UV sterilized for 20 minutes, and bovine calf serum (BCS) was added, resulting in protein adsorption on the surface of the PDMS, helping in cell adhesion. It was then incubated at 37°C overnight before seeding the cells.

Cell types chosen for the experiments are the NIH3T3 fibroblasts, and MC3T3 osteoblasts. Fibroblasts and osteoblasts were initially grown in a flask in Dulbecco's Modified Eagle's Medium (DMEM) with 10% BCS, and 1% penicillin streptomycin (p/s) and Minimum Essential Medium Eagle - alpha (MEM-alpha) with 10% fetal bovine serum (FBS), and 1% p/s, respectively. Once cells reached the required confluence, they were seeded onto the PDMS at a density of 4000 cells/cm^2. The PDMS was then incubated again at 37°C, 5% CO_2, and 80% humidity overnight to allow cells to adhere to the surface, before placing it on the cell stretcher for experiments. In order to label the nucleus, NucBlue Live ReadyProbes Reagent (Thermofisher) was used, and imaged using fluorescence microscopy at 360nm excitation and 460nm emission (DAPI channel). After the cyclic stretching, cells were fixed for 10 minutes using 4% Paraformaldehyde and stained for Actin using Alexa Fluor 488 Phalloidin (1:200 in PBS), to be imaged using fluorescence microscopy at 490nm excitation and 525nm emission (GFP channel).

3.5. Seeding density

Because the cyclic loading was applied to the elastic membrane, it is necessary for the cells to be well adhered to the substrate. It was observed that irrespective of the type of cell chosen, right seeding density had to be maintained in order to obtain proper adhesion of cells to the substrate. Cells with a seeding density of 10000 cells/cm^2 resulted in a high confluency when incubated for 48 hours. They were found to be well adhered to the surface as well as to its neighbouring cells, as shown in Fig. 3.11. Cyclic loading of such a group of cells that were attached to each other resulted in re-alignment without any detachment from the substrate, but their response could not be analysed as individual cells. Alternatively, when cells were incubated just overnight in order have less confluency, they were found to detach from the substrate when subjected to cyclic stretching.

In order to avoid the formation of sheet of cells, which was found to be formed as a result of cyclic stretching highly confluent cells, seeding density was reduced to 4000 cells/cm^2, and incubated overnight. This resulted in individual cells that were well adhered to the PDMS substrate, without being attached to its neighbouring cells, as shown in Fig. 3.12. In order to stain the nucleus, 30 minutes before the start of the experiment, NucBlue drops were added to the media, and incubated. After clamping the PDMS membrane onto the cell stretcher and setting up the guides, it was placed in the EVOS onstage incubator. Membrane was slightly stretched in order to remove any wrinkles that might have formed. Phase contrast and fluorescence images were taken through the PDMS membrane, which provided a reference configuration to compare the cells after the deformation.

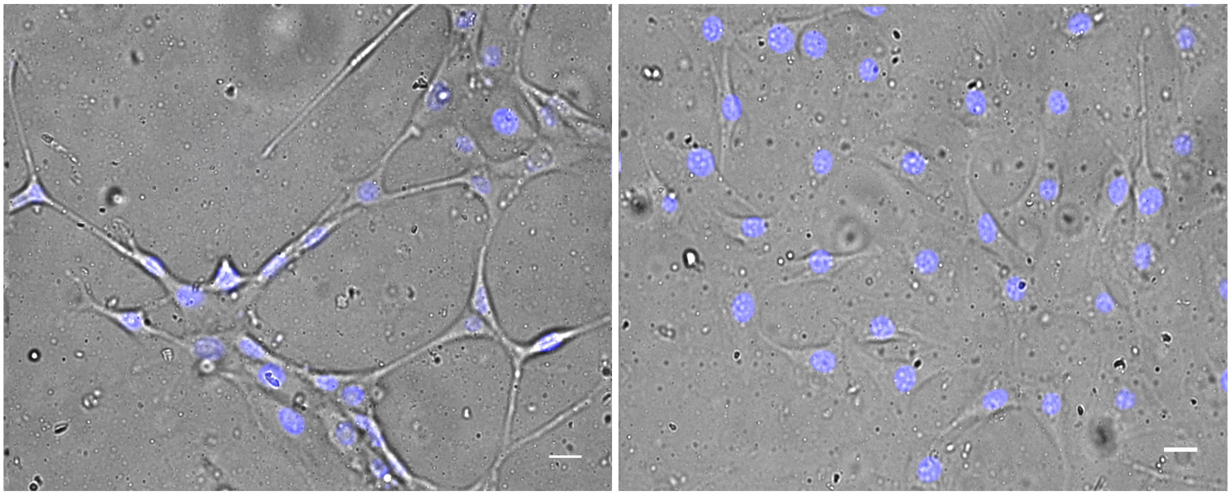
(A) (B)

Fig. 3.11: Representative merged image of nucleus, indicated by blue stain and cell, by phase contrast image of (a) Fibroblast cells and (b) Osteoblast cells seeded with a seeding density of 10000 cells/cm^2. It can be seen that cells are attached to each other even before they are subjected to cyclic stretching. Scale bar = 25μm

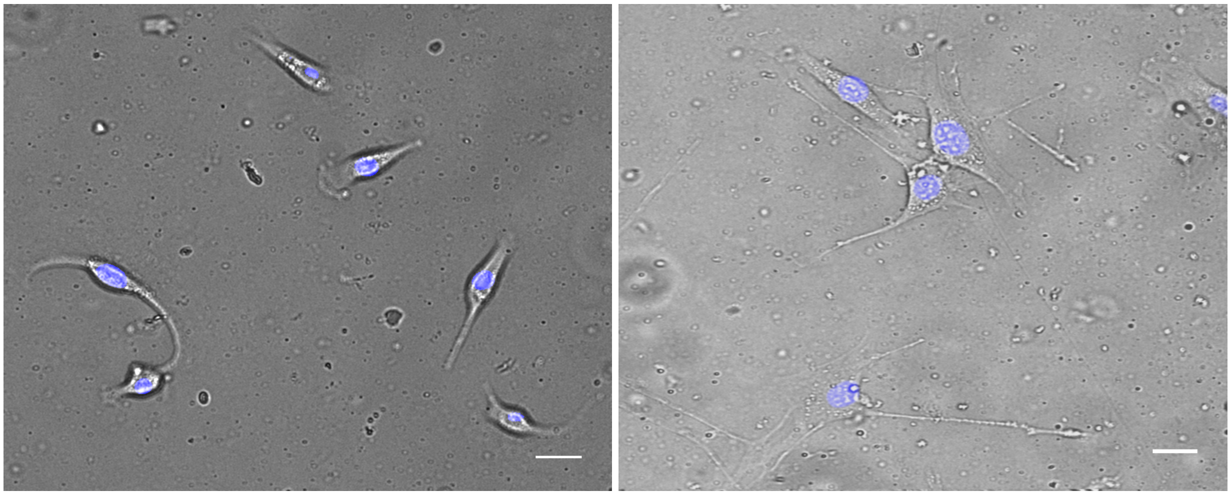

(a) (b)

Fig. 3.12: Representative merged image of nucleus, indicated by blue stain and cell, by phase contrast image of (a) Fibroblast cells and (b) Osteoblast cells seeded with a seeding density of 4000 cells/cm^2. It can be seen that the chosen seeding density allows cells to be individual, while adhered to the membrane. Scale bar = 25μm.

Soon after imaging, Arduino was powered on, which supplied the necessary current to run the stepper motors following the sketch written in Arduino IDE. The incubator within which the cell stretcher was placed, provided a benign ambience for the cells to survive, while experiencing the cyclic stimuli. Based on several experimental observations on the duration of stretching, it was found that stress fibres had reached a steady state after 6 hours for fibroblast cells, and 8 hours for osteoblast cells, and hence all the cyclic loading experiments presented in this chapter are performed for 6 hours, and 8 hours for fibroblast, and osteoblast cell types respectively. During the experiment, the media was constantly monitored, and fresh media was added if need be. Once the experiment was completed, cells were imaged again through the PDMS membrane, followed by fixing the cells and staining for actin. The cells were then imaged using fluorescence microscopy, to observe the properties of actin. Representative images showing fixed cells in their reference state is shown in Fig. 3.13. It can be observed that cells are not clumped and hence, single cells could be considered for analysis. The response of such single cells would be due to cell-matrix adhesion rather than cell-cell interactions.

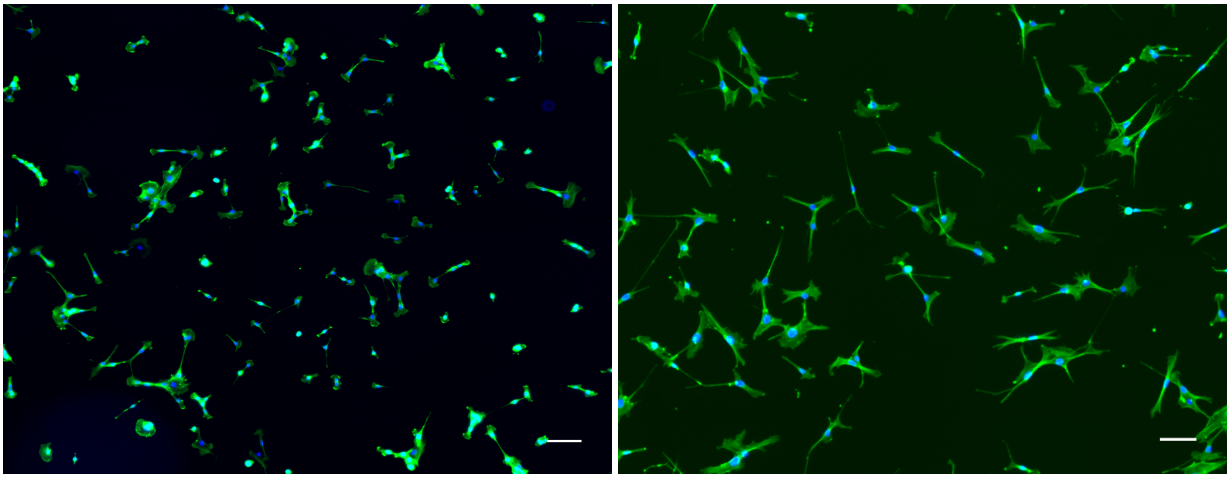

(A) (B)

Fig. 3.13: Representative images of cells in their reference state, fixed and stained for actin (green), and nucleus (blue) of (A) Fibroblast and (B) Osteoblast cells. Scale bar = 50μm

Preliminary objectives of the experiments were to observe the response of cells due to *in vitro* cyclic loading stimuli, using the cell stretcher that was custom built through the additive manufacturing process. The results from the experiments were to be used for validating the numerical model developed for simulating such behaviours. As discussed in Sec. 2.8, it has been observed in literature that cells reorient away from the direction of loading due to uniaxial cyclic stretch, which is found to depend on the cyclic loading parameters as well. In this regard, two loading cases were considered to study their effects on fibroblast and osteoblast cells. Fibroblasts are found to be dispersed in connective tissues throughout the body. They perform the function of healing the injury by migrating to the wound and producing a large amount of collagenous matrix, which helps to isolate and repair the damaged tissues [27]. Fibroblasts are one of the easiest type of cells to culture in the laboratory, providing a robust cell type for the *in vitro* experiments. Osteoblasts are bone cells, responsible for the growth of a new bone. They secrete bone matrix, which is deposited over the existing matrix that is rapidly combined with calcium phosphate crystals forming a new layer of bone [27]. Both these cell types experience cyclic mechanical stimuli through out their life spans, resulting in physiological significance of cyclic *in vitro* mechanical stimuli studies of these cell types. Orientation analysis of stress fibres was performed using the OrientationJ plugin [150] in Fiji, an image processing software [151], a distribution of ImageJ [152].

3.6. Cyclic uniaxial stretch

Pre determined cyclic stretch was applied to the membrane, which is transferred to the cells through focal adhesions that develop the contact between the cell and the substrate. The parameters of the applied loading cycles are given in Table. 3.1.

Case	Stretch(mm)	ε(%)	f(mHz)
OL, FL	2.5	7	7.9
OH, FH	7.5	20	7.9

Table 3.1: Parameters for cyclic loading. OL and OH cases indicate osteoblast cells subjected to low and high amplitude loads, while FL and FH indicate fibroblast cells subjected to low and high amplitude loads.

The experiments performed on osteoblast cells are indicated by OL, and OH, representing the stretch applied on osteoblast cells with low amplitude and high amplitude respectively. Similarly, experiments performed on fibroblast cells are indicated by FL and FH, representing the stretch applied on fibroblast cells with low and high amplitudes respectively, as given in Table. 3.1. OL and FL experienced 7% strain while OH and FH experienced 20% strain. As given in Table 3.1, the amplitude is varied keeping the frequency constant. The results of cyclic loading experiments were analysed through statistical measures. As explained in [153], in order to handle large sample sizes, suitable circular statistical tests have to be adopted. In this regard, as observed in [7], circular variance has been found to be a good measure to quantify the orientation of stress fibres. Following [153], if a unit circle is subdivided into k arcs of equal length such that ϕ_i $(i = 1, 2, ..., k)$ represents the angle of the midpoint of the ith arc, the rectangular components of the unit vector corresponding to ϕ_i can be written as

$$x_i = \cos\phi_i, \ y_i = \sin\phi_i. \tag{3.1}$$

In order to deal with stress fibre orientation, which is a set of diametrically bimodal circular data, angles are doubled, resulting in

$$x_i = \cos 2\phi_i, \ y_i = \sin 2\phi_i. \tag{3.2}$$

If n_i is the sample frequency measured in each of the k arcs, the mean of the rectangular components can then be evaluated as

$$\bar{x} = \frac{1}{n}\sum_{i}^{k} n_i \cos 2\phi_i, \ \bar{y} = \frac{1}{n}\sum_{i}^{k} n_i \sin 2\phi_i \tag{3.3}$$

where, n represents the sample size, evaluated as

$$n = \sum_{i}^{k} n_i. \tag{3.4}$$

Circular variance can then be defined as

$$CV = 1 - \sqrt{\bar{x}^2 + \bar{y}^2}. \tag{3.5}$$

Value of CV is 1 if the distribution is uniform and 0 if it is oriented about a particular angle. Experiments were performed on cells seeded with 4000 cells/cm^2 seeding density. Cells fixed at the end of the loading cycles were imaged using the EVOS microscope with 40x objective(Olympus). 100 individual cells were chosen, and the orientation results $\gamma_i(\phi)$ were obtained using a macro written in ImageJ which uses the OrientationJ plugin, where γ indicates the amount of stress fibres in cell i at an angle ϕ. It evaluates angular distribution of stress fibres from $-\pi/2$ to $\pi/2$ with a step of 0.5 degree. The results were then averaged by normalising the value for each cell ($\bar{\gamma}(\phi)$), which could then be presented as bar, and circular histograms

$$\bar{\gamma}(\phi) = \frac{1}{N}\sum_{i}^{N} \frac{\gamma_i(\phi)}{\max(\gamma_i(\phi))} \ .$$

NIH3T3 Fibroblasts

To begin with, fibroblast cells were subjected to 7% uniaxial cyclic strain, indicated by FL, for 6 hours. At the end of the loading cycle, it was observed that cells have reoriented to directions away from the direction of loading, as seen in Fig. 3.14(A). The cells, which were then fixed and stained for actin showed that distinct stress fibres were formed following the reoriented direction of cells, as shown in Fig. 3.14(B). By choosing 100 cells at random, average histogram of the stress fibre orientation was evaluated, as shown in Fig. 3.14(D). It can be seen that stress fibres exhibit two dominant directions, one at 50°, and the other at $-54°$. The result can be expressed in terms of a circular histogram as well, Fig. 3.14(C), where stress fibre in every measured direction can be obtained by evaluating the corresponding vector. Double headed arrow in Fig. 3.14(C) indicates the direction of loading, representing 0°. Circular variance can then be evaluated as given in Eq. 3.5, leading to a value of 0.89, as shown in Fig. 3.14(C), for the particular loading condition and cell type. This indicates that although all fibres are not aligned along a particular direction, they are not uniformly distributed, which could be seen by Fig. 3.14(D) as well. In sum, it was observed that cyclic loading resulted in stress fibres being formed in directions away from 0°, which is the direction of loading.

When the amplitude of the cyclic load was increased such that the strain was 20%, denoted by FH, it was found that the dominant angles of stress fibre orientation were 65°, and -70°, as seen in Fig. 3.15(D). The phase contrast image, Fig. 3.15(A) shows the cells aligned away from the direction of loading, and the fluorescence image of actin stained cell shows the stress fibre, Fig. 3.15(B). Circular histogram with a evaluated circular variance of 0.83 can be seen in Fig. 3.15(C) indicating that more stress fibres are aligned than that obtained with the FL case. It can also be observed that, with an increase in the amplitude of the stretch, the dominant angle shifted more from the direction of loading. Due to the presence of two dominant angles with different magnitudes, the circular histogram obtained is asymmetric too. Thus, it was seen that with an increase in the amplitude of the cyclic loading, keeping the frequency constant, orientation angle shifted more from the direction of loading.

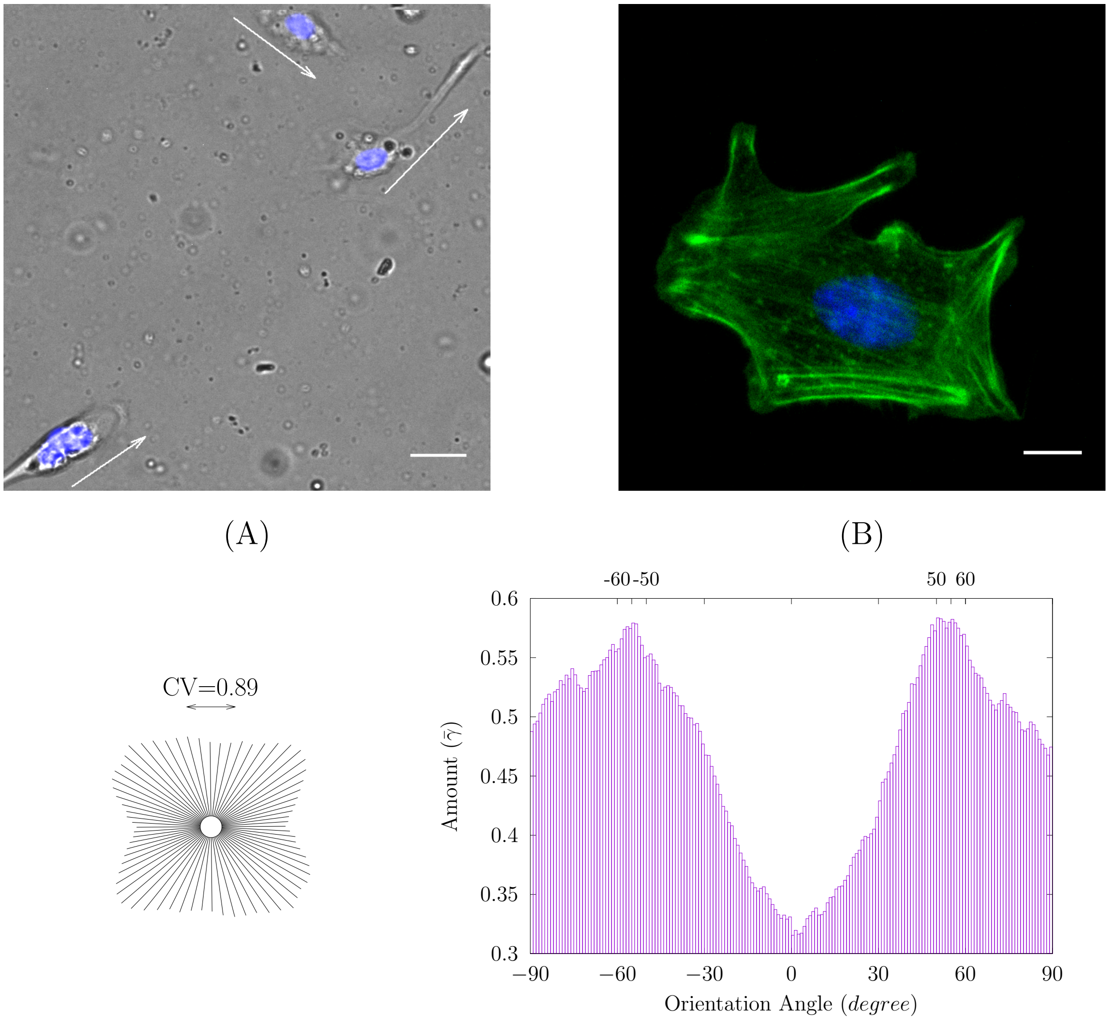

(A) (B)

(C) (D)

Fig. 3.14: (A) Phase contrast image of fibroblast cells subjected to FL loading condition. Arrows indicate the direction of alignment of each cell. (Scale bar = 25μm) (B) Representative image of stress fibres subjected to FL load case. (Scale bar = 20μm). (C) Circular histogram representing the amount of fibre in each angle with its circular variance. Double headed arrow indicates the direction of loading, representing 0°. (D) Bar histogram obtained by averaging angular values of 100 cells. Direction of loading ⟷.

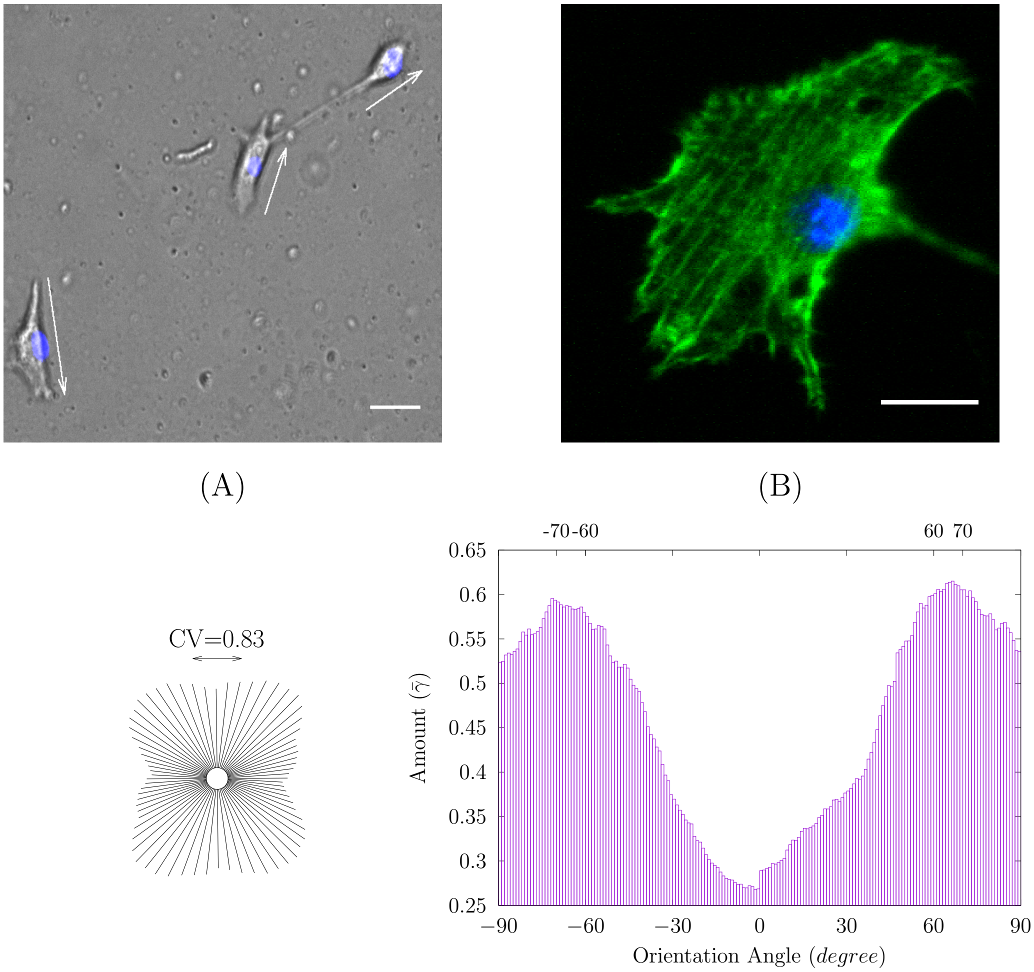

(A) (B)

(C) (D)

Fig. 3.15: (A) Phase contrast image of fibroblast cells subjected to FH loading condition. Arrows indicate the direction of alignment of each cell. (Scale bar = 25μm) (B) Representative image of stress fibres in a fibroblast cell subjected to FH load case. (Scale bar = 20μm). (C) Circular histogram representing the amount of fibre in each angle with its circular variance. Double headed arrow indicates the direction of loading, representing 0°. (D) Bar histogram obtained by averaging angular values of 100 cells. Direction of loading $\longleftrightarrow$.

MC3T3 osteoblasts

Osteoblasts were subjected to similar loading conditions, denoted by OL and OH in Table. 3.1, for 8 hours. It was observed that osteoblast cells responded more slowly compared to fibroblast cells. Phase contrast image of cells subjected to a cyclic load, case OL, at the end of 8 hours is given in Fig. 3.16(A). The fluorescent image of a cell with stress fibres, is shown in Fig. 3.16(B), along with the bar histogram Fig. 3.16(D), obtained by averaging 100 cells. It can be seen that osteoblast cells orients to two dominant angles 63°, and $-50°$, even though less distinct as compared to fibroblast cells. The circular histogram with its circular variance of 0.93 can be seen in Fig. 3.16(C), along with double headed arrow indicating the direction of loading, at 0°. The circular variance is higher than that of fibroblasts indicating the loss of dominant directions of stress fibre orientation, as observed with fibroblast cells.

When osteoblast cells were subjected to 20% cyclic strain, indicated by OH, dominant angles were higher than that obtained for the OL case, a behaviour similar to that observed in fibroblasts as well, as seen in the phase contrast image of Fig. 3.17(A). The dominant directions were now found at 50°, and $-85°$, as shown in Fig. 3.17(D). The circular histogram shows the distribution of stress fibres with its evaluated circular variance to be 0.92, Fig. 3.17(C). This indicates that the stress fibre alignment is more dominant towards particular directions than it was observed during the OL loading condition. But the difference in circular variance and hence the re-alignment of stress fibres was not as drastic as observed in fibroblast cells. This can be explained by the observation that in experiments on osteoblast cells with a seeding density of 10000 cells/cm^2, distinct stress fibres were formed only in a few cells in contrast to fibroblasts where stress fibres were present in most of the cells at the end of the stretching experiment, as shown in Fig. 3.18. This might be due to low frequency of the cyclic load being applied.

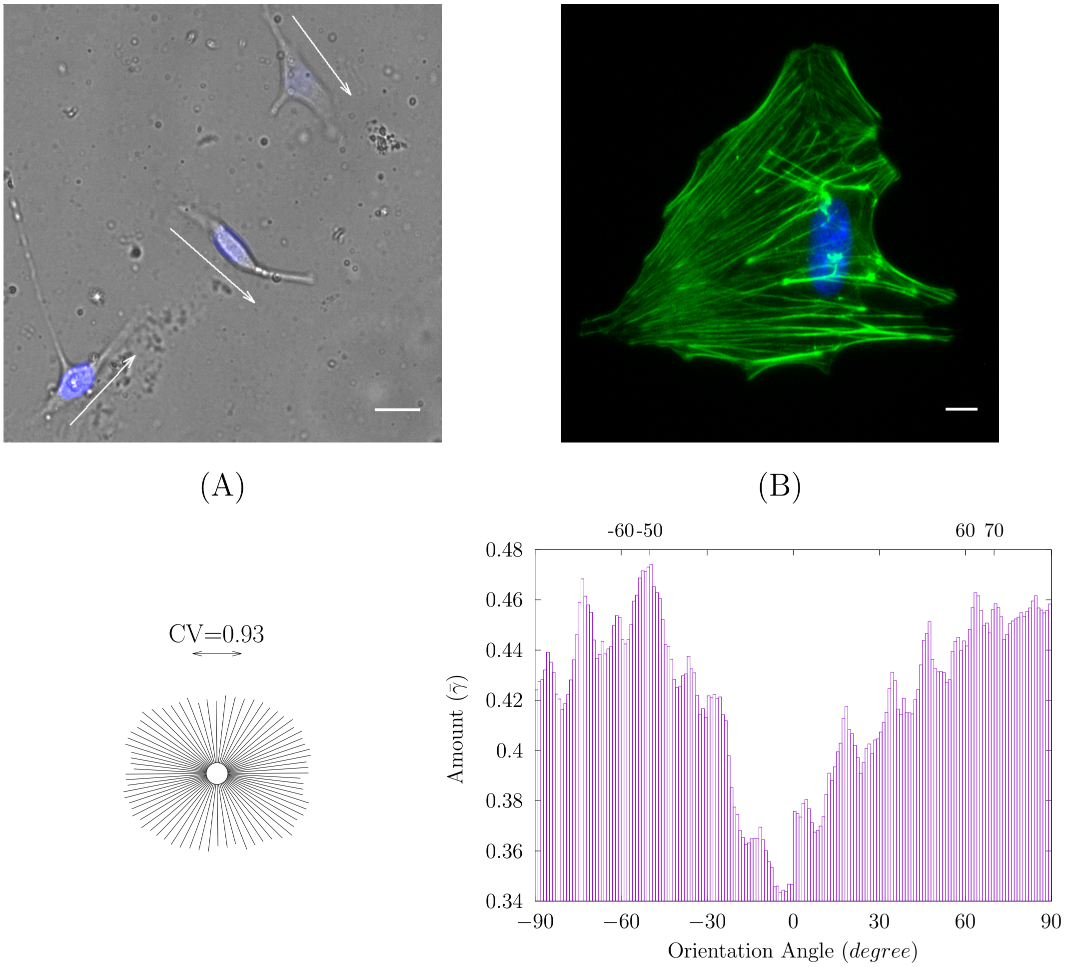

(A) (B)

(C) (D)

Fig. 3.16: (A) Phase contrast image of osteoblast cells subjected to OL loading condition. Arrows indicate the direction of alignment of each cell. (Scale bar = 25μm) (B) Representative image of stress fibres subjected to OL load case. (Scale bar = 20μm). (C) Circular histogram representing the amount of fibre in each angle with its circular variance. Double headed arrow indicates the direction of loading, representing 0°. (D) Bar histogram obtained by averaging angular values of 100 cells. Direction of loading $\longleftrightarrow$.

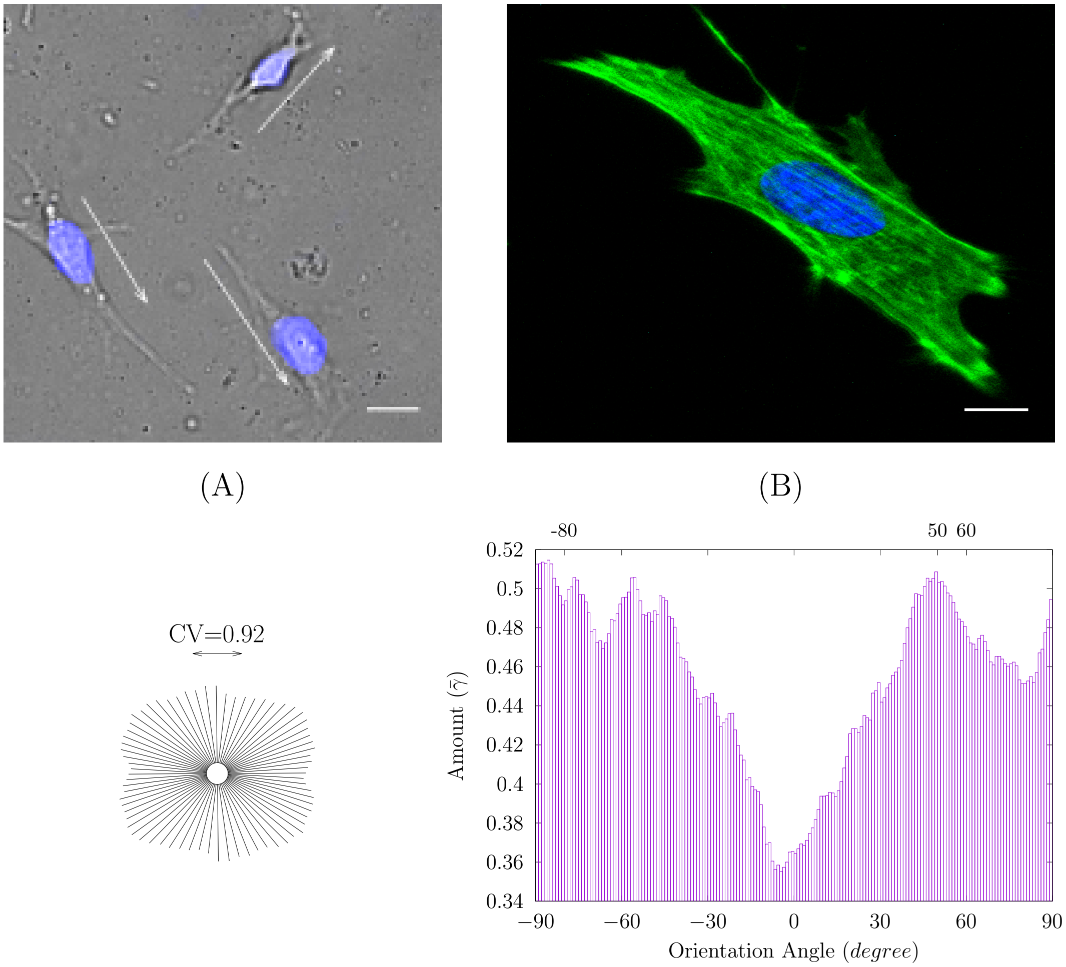

(A) (B)

(C) (D)

Fig. 3.17: (A) Phase contrast image of osteoblast cells subjected to OH loading condition. Arrows indicate the direction of alignment of each cell. (Scale bar = 25μm) (B) Representative image of stress fibres subjected to OH load case. (Scale bar = 20μm). (C) Circular histogram representing the amount of fibre in each angle with its circular variance. Double headed arrow indicates the direction of loading, representing 0°. (D) Bar histogram obtained by averaging angular values of 100 cells. Direction of loading $\longleftrightarrow$.

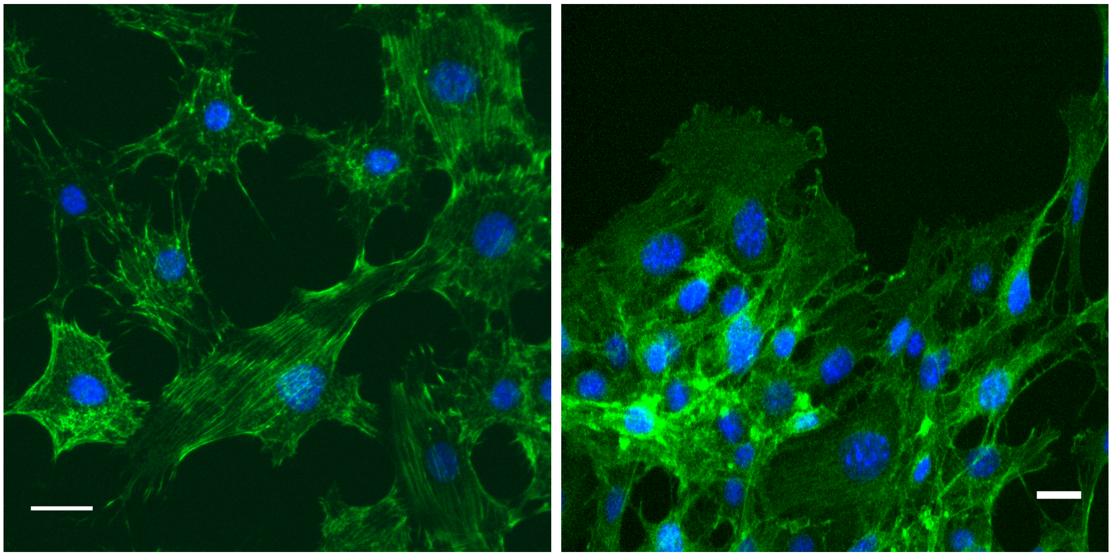

(A) (B)

Fig. 3.18: (A) Only a fraction of osteoblast cells, seeded at 10000 cells/cm^2, subjected to 20% strain formed dominant stress fibres. (B)But, in case of fibroblast cells, stress fibres are formed in almost all cells, and even cells are aligned in the dominant directions away from the direction of loading. Scale bar = 25μm. Direction of loading $\longleftrightarrow$.

In order to quantify the different orientation responses of cells to different amplitudes, average value of cos2θ is evaluated for each cell as given in Eq. 3.3, which is then averaged over all the cells considered for analysis ($\langle\cos 2\theta\rangle$). As explained in [7], the value of $\langle\cos 2\theta\rangle = 0$ for uniform or randomly distributed cells, while the value is +1 and -1 for cells that are oriented along the direction of loading and orthogonal to it respectively. In addition, statistical tests were performed by ANOVA followed by multiple comparison test in order to determine if the datasets are significantly different.

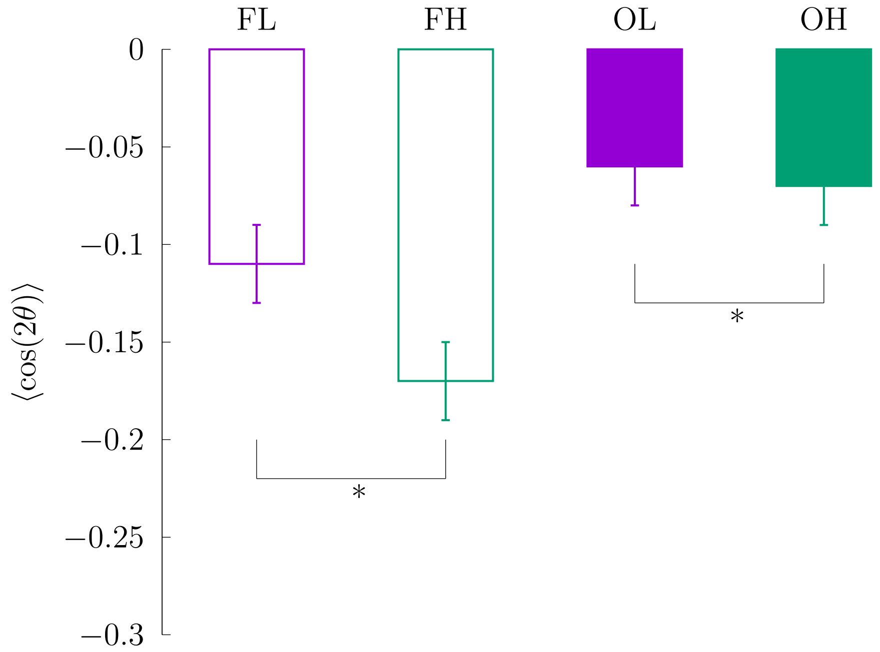

Fig. 3.19: Distribution of $\langle \cos 2\theta \rangle$ for different cell types and loading conditions, expressed as mean±SEM. * indicates that the data is significantly different as obtained by ANOVA followed by multiple comparison test.

It can be seen from Fig. 3.19 that the value of $\langle \cos 2\theta \rangle$ is -0.11 for fibroblast cells subjected to the load case FL. As the amplitude is increased, case FH, the value is increased to -0.17 indicating that the orientation of stress fibres tends to become aligned, and away from the direction of loading. A similar behaviour was observed even in osteoblast cells, where, with increase in amplitude of cyclic loading, $\langle \cos 2\theta \rangle$ changed from -0.06 to -0.07. Statistical tests to determine the difference between data sets indicated a significant difference between different cases, as indicated by $*$ in Fig. 3.19. Results of ANOVA followed by multiple comparison tests are given in Appendix.

The images of fixed cells were further analysed by considering a random area of cells and evaluating the circularity parameter in ImageJ by considering 750 cells. Circularity is defined as

$$Circularity = 4 * \pi * \frac{area}{perimeter^2} \tag{3.6}$$

which is 1 for a perfect circle and a value of 0 indicates an infinitely long ellipse or a straight line. It can be seen in Fig. 3.20 that the circularity of fibroblast cells subjected to the load case FL is 0.79, while with increase in amplitude, circularity falls to 0.71. This indicates that with increase in the amplitude of stretching, cells become more elongated. Surprisingly, cells which were not subjected to any external loading, indicated by FR in Fig. 3.20, gave a circularity value of 0.74, which is lower than that of the cells subjected to the load case FL. A similar behaviour was observed even with osteoblast cells, where OR cells gave a circularity value of 0.78 while OL and OH gave circularity values of 0.79 and 0.77 respectively. This shows that the cyclic loading results in an increase in the circularity of cells, when subjected to low amplitude loads, but decreases when the amplitude is increased.

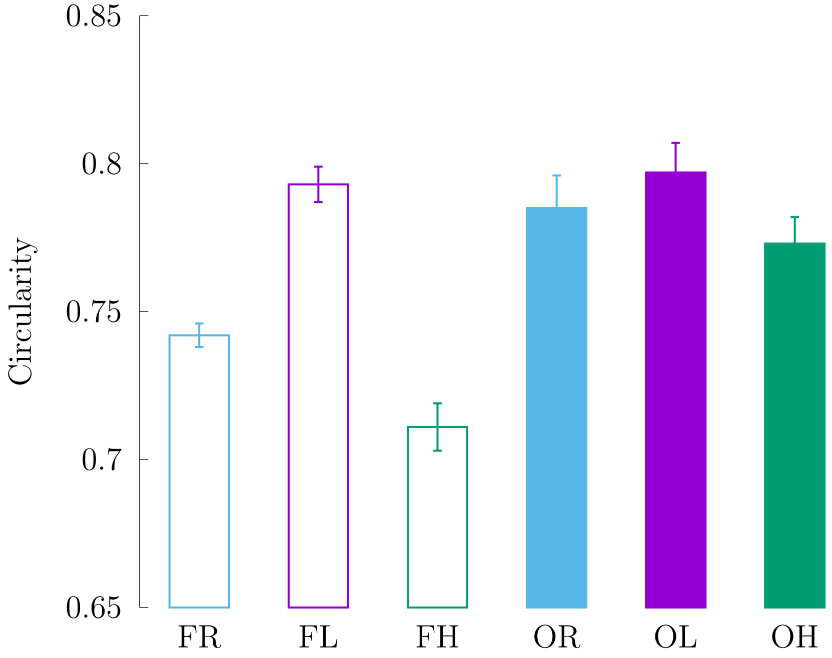

Fig. 3.20: Circularity of fibroblast and osteoblst cells for different amplitudes. Circularity of control cells (FR, OR) was lower than that of low amplitude loadings (FL, OL) which reduced with further increase in amplitude (FH, OH). Data is expressed as mean±SEM.

3.7. Live cell reorientation

In literature, several uniaxial stretching experiments have been performed, but due to the lack of live imaging capability of the device, not all experiments have been able to observe the reorientation phenomenon. In this regard, taking advantage of the live imaging capability of the additively manufactured cell stretcher, cells were imaged through the

PDMS by pausing the cyclic stretch. The experiments were performed on both fibroblast, and osteoblast cell types. Due to uniaxial cyclic stretch, cells change its shape such that they align away from the direction of loading, and as seen from the images of fixed cells, even stress fibres were formed in the same direction. An attempt was made to transfect the cells for actin to perform live imaging of stress fibre growth. But, due to auto flourescence of PDMS in the green channel, it was not possible to view stress fibre orientation live, using the EVOS autofluorescence microscope system. It can be seen from Fig. 3.21 that when cells were subjected to uniaxial cyclic load in the horizontal direction, they change their shape, migrate, form cell-cell adhesion with the neighbouring cells and align in a direction to avoid the applied load. Similar behaviour was observed even with osteoblast cells as seen in Fig. 3.22.

It can be observed from Fig. 3.21, and Fig. 3.22 that with the same applied cyclic load, fibroblast cells respond faster than osteoblast cells. Cells were found to reorient away after 5 hours of cyclic loading in case of fibroblasts, while the reorientation was observed only after 8 hours in case of osteoblasts. The observed difference might be due to the physiological function of each type of cells. The difference in circularity results between osteoblast and fibroblast cells can also be observed from Fig. 3.21, and Fig. 3.22. It was observed in [8] that initially stress fibres were formed in directions away from loading, followed by cell orientation. In this regard, it would be fair to assume that stress fibres have reached a steady state at the end of loading cycle while cells might further migrate if the cyclic loading would have been continued.

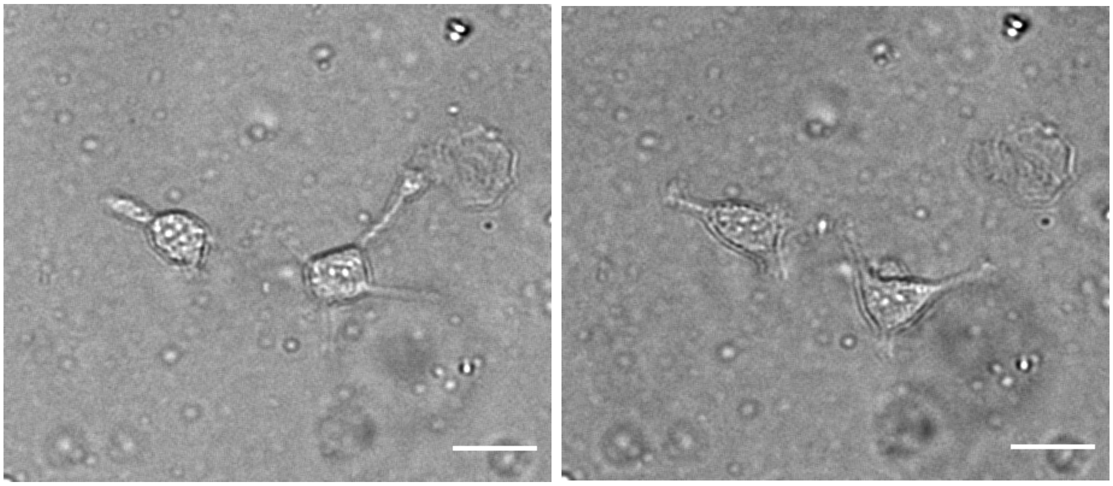

t = 0 min

t = 30 min

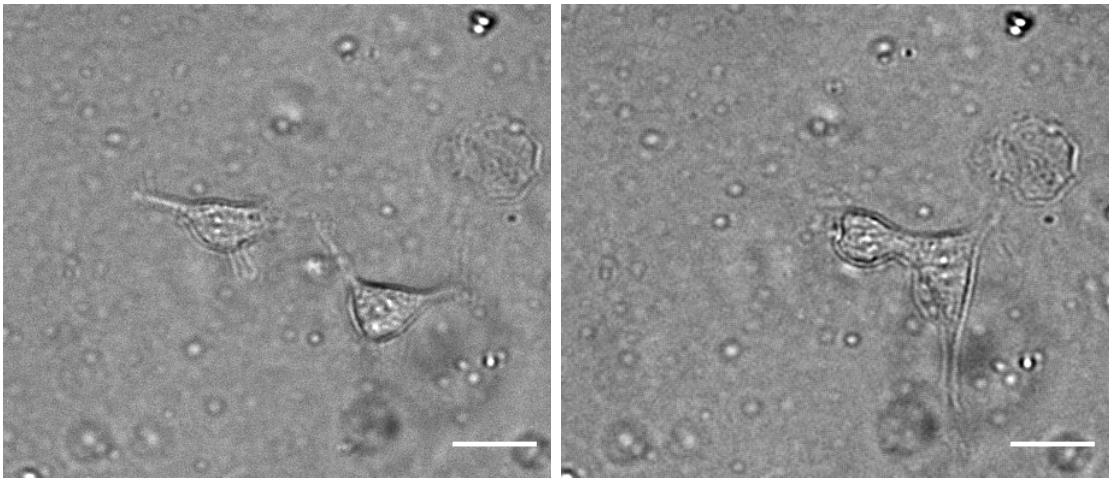

t = 60 min

t = 120 min

t = 180 min

t = 300 min

Fig. 3.21: Evolution of fibroblast cells over time. Cells reorient and migrate in direction away from the loading direction. Direction of loading $\longleftrightarrow$. Scale bar = 25μm

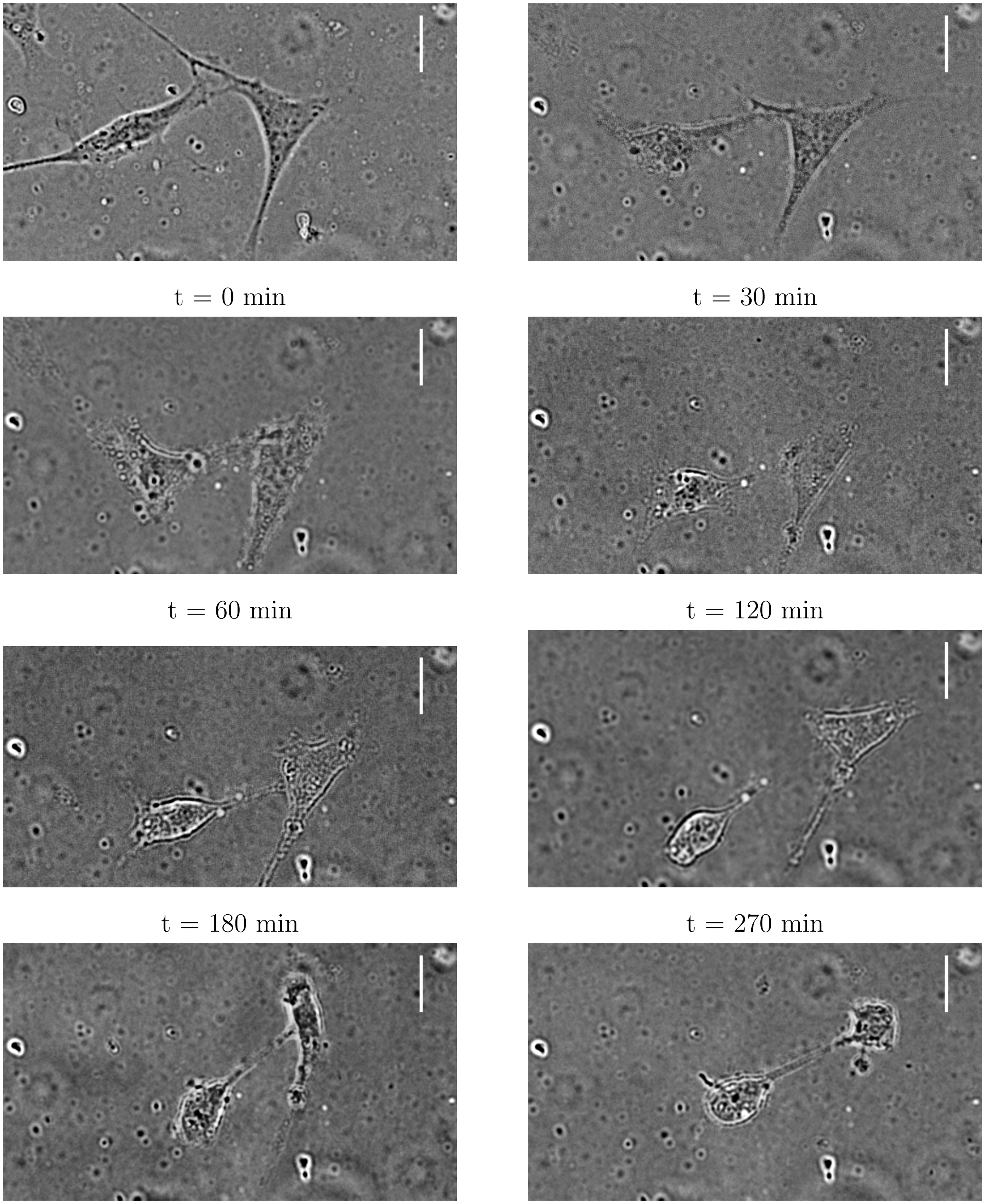

t = 0 min

t = 30 min

t = 60 min

t = 120 min

t = 180 min

t = 270 min

t = 420 min

t = 480 min

Fig. 3.22: Evolution of osteoblast cells over time. Cells reorient and migrate in direction away from the loading direction. Direction of loading ↕. Scale bar = 25μm.

3.8. Summary

In this chapter, a novel device to apply the uniaxial cyclic loading on cells has been designed and manufacturing process has been elaborated. Additive manufacturing process using the 3D printing technology has made the device cost effective along with the ability to place the device within the onstage incubator of the microscope system. Using stepper motors controlled by Arduino has made it possible to apply cyclic loading with varying parameters. Thus, compared to either commercially available cell stretchers or other open source alternatives available, this design is compact and robust with high level of accuracy. Using this device, experiments have been performed on two types of cells, fibroblasts, and osteoblasts, and quantitative analysis was performed using atleast 100 cells. PDMS, a biocompatible elastic membrane was used as a substrate for the cells to adhere. Different amplitudes of cyclic load was applied to study their responses. Analysis of cells subjected to uniaxial cyclic loading showed that stress fibres were formed primarily in directions away from the direction of stretch. The orientation was found to be more dominant with increase in amplitude of the cyclic load. In addition, live imaging of the response of cells to such loading could be performed, where it was observed that osteoblast cells responded slower than fibroblast cells. Thus, the response of cells was found to depend on the parameters of the cyclic load in congruence to their physiological behaviour. Understanding such a variety of cell reorientation behaviours can help in developing artificial tissues. In order to design and develop right experiments and understand the intricate relationships between different components of the cell, it is necessary to make use of the numerical simulations. In this regard, the following chapters will deal with developing a numerical model that can simulate the behaviour of cells subjected to a variety of mechanical loading conditions.

4. Mathematical modelling of stress fibre reorientation

The external mechanical stimulus is experienced by the cell at focal adhesions. The external stimuli causes chemical reactions within the cytoplasm, resulting in the growth of stress fibres. Growth of stress fibres, which is therefore dependent on the mechanical stimuli, varies based on the type of loading, further affects focal adhesion, thus completing a feedback loop. In this chapter, a mathematical model for the stress fibre growth coupled with focal adhesion formation and the feedback loop controlling the cytoplasmic calcium concentration is introduced, as developed in [12]. Numerical examples will be solved to observe the behaviour of stress fibre and focal adhesion growth under a variety of loading and environment conditions, including the cyclic loading experiments as performed in Chapter 3.

4.1. Modelling Assumptions

As explained in Chapter 2, bio-chemical processes occurring within a cell involve various proteins and their complex interactions. Developing a mathematical model which includes chemistry of all the reactions would make it highly cumbersome and might be very complicated to obtain a meaningful solution. In this regard, it is common to make assumptions which can simplify the model without losing physics of critical processes. In the current formulation, only stress fibre and focal adhesion growths are considered to influence the behaviour of cells. It is assumed that the cytoplasm consists of actin-myosin stress fibres only, and the active processes of other organelles such as microtubules and nucleus are neglected. The actin and myosin proteins needed for the formation of stress fibres is assumed to never deplete. In addition, focal adhesion proteins are assumed to consist of integrins only. With these assumptions, though it is not possible to extract the exact nature of cell biology, it is sufficient to understand the overall nature of the response of cells to particular stimuli types. Hence, the model attempts to simulate the behaviour of cells to particular mechanical loadings using stress fibre and focal adhesion, along with their interaction.

4.2. Stress fibre growth

The following three assumptions are considered for the development of the stress fibre model:

(i) One of the prominent functions of stress fibres is to transfer the stress from cytoskeleton to ECM, thereby ensuring the mechanical equilibrium of the cell. Hence, stress fibres must be connected to the ECM at focal adhesion which can happen in ventral stress fibres only. The term stress fibres used in the mathematical model thus implies ventral stress fibres. On the other hand, actin staining experiments show all types of stress fibres and therefore it can be assumed that sufficient actin and myosin are present in the cytoplasm for the stress fibre growth. Extending this hypothesis, it can be assumed that during stress fibre reorientation process, the reduction of stress fibre concentration in one direction does not influence the concentration in other directions. That is, the formation of stress fibre in one direction does not curtail the availability of actin to form stress fibres in other directions.

(ii) Due to the difference in the way stress fibres contract compared to muscle sarcomeres, as explained in Chapter 2, the solution for the stress fibre growth during contraction is obtained by allowing rapid cycles of dissociation and re-association of α-actinin to actin filaments. Thus, it can be assumed that, an increase in contractile stress leads to reduced dissociation rather than a direct increase in association.

(iii) The free calcium ions present in the cytoplasm play an important role in stress fibre contractility as observed in [154] and [155].

Based on these assumptions, the stress fibre growth model is formulated in terms of a directional stress fibre concentration rate, cf [112]:

$$\dot{\eta}(\phi) = \begin{cases} (1-\eta(\phi))\, C\, k_f - (1-\kappa)\, \eta(\phi)\, k_b & \text{if } \kappa < 1 \\ (1-\eta(\phi))\, C\, k_f & \text{if } \kappa \geq 1 \end{cases} \tag{4.1}$$

where,

$$\kappa \;=\; \frac{\sigma^a(\phi)}{\sigma_0(\phi)} \tag{4.2}$$

is the ratio of active stress $\sigma^a(\phi)$ in the stress fibre due to the actin-myosin bridge to the isometric stress $\sigma_0(\phi)$, and where

$$\sigma_0(\phi) \;=\; \eta(\phi)\,\sigma_{max} \tag{4.3}$$

with σ_{max} being the maximum stress allowed in the stress fibre. The stress fibre concentration at an inclination angle ϕ is denoted with $\eta(\phi)$, $(0 \leq \eta(\phi) \leq 1)$. Furthermore, C represents the calcium concentration available for contractility within the cytoplasm, and k_f and k_b are rate constants related to the association and dissociation of stress fibres, respectively. Since it has been observed that stress fibres are absent in a cell which is not stressed, it can be assumed that, $\eta(\phi) = 0$ at $t = 0$ to be an appropriate initial condition.

From Eq. 4.1 the following principal behaviours for the growth model can be deduced:

(i) as the concentration of stress fibre increases, the rate of stress fibre association reduces.

(ii) the association of stress fibres is directly dependent on the calcium concentration.

(iii) if the active stress in the stress fibre is less than the isometric stress, an increase in the active stress prevents further dissociation of stress fibres.

(iv) if the active stress is greater than or equal to the isometric stress, it is assumed that no further dissociation is possible, and hence the dissociation part becomes zero, thereby preventing the collapse of stress fibre, and supporting the tensegrity model [107].

4.2.1. Effect of calcium signalling

To study the influence of calcium signal C on the stress fibre concentration η, the ratio of active stress to isometric stress, κ in Eq. 4.1 is set to 0 in order to nullify the influence of active stress on the stress fibre growth. To illustrate the behaviour of Eq. 4.1, an exponentially decaying ad-hoc calcium signal is considered:

$$C = \exp\left(-\frac{t}{\theta}\right) \tag{4.4}$$

where t represents the instantaneous time and θ its time constant. By choosing k_f and k_b to be $10/s$ and $1/s$ respectively, stress fibre growth is evaluated and compared with that obtained when calcium signal is kept constant, $C = 1$. Accordingly, it can be seen that when an exponential signal is applied, stress fibre concentration decays with time, while it reaches a peak and remains constant when calcium is held constant as shown in Fig. 4.1(a). It can also be seen that, when calcium activation signal is applied multiple times, even the stress fibre concentration follows the calcium signal, as shown in Fig. 4.1(b).

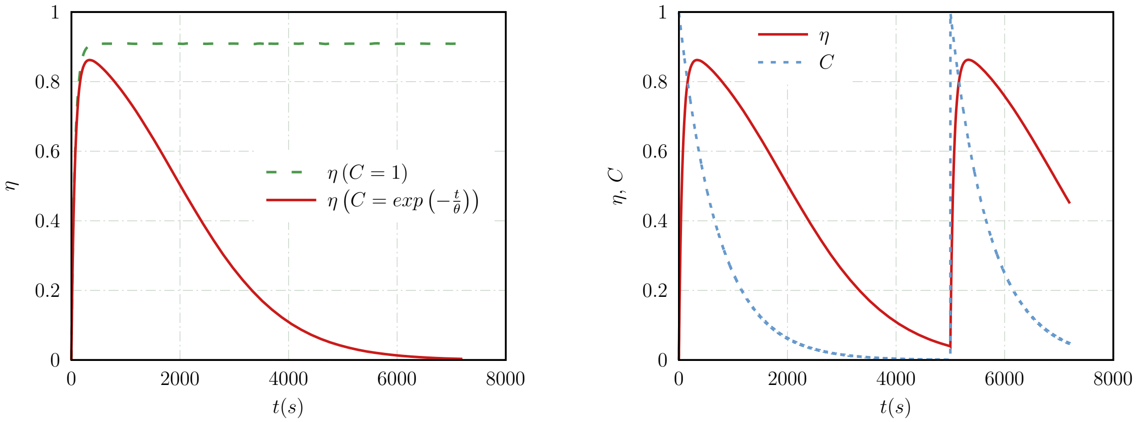

(a) Stress fibre growth for a single activation signal

(b) Stress fibre growth behaviour when multiple activation signals are applied

Fig. 4.1: Comparison of stress fibre growth for (a) single calcium activation signal (b) multiple activation signals, with $\kappa = 0$.

In addition, it can be seen that when dissociation is made zero by setting $\kappa = 1$, stress fibre reaches a steady state and does not dissociate even with an exponentially decaying calcium signal, as shown in Fig. 4.2, showing that stress fibre growth depends on both the cytoplasmic calcium and the instantaneous active stress.

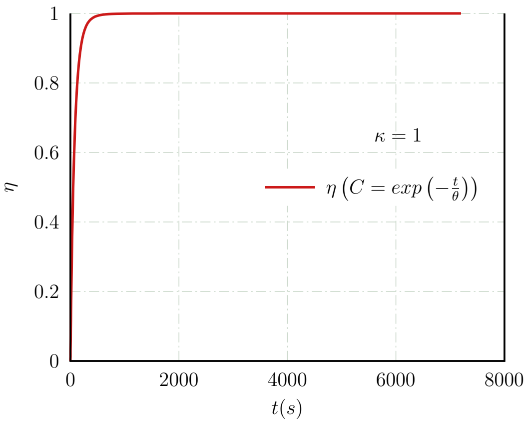

Fig. 4.2: Stress fibre growth when dissociation term is nullified ($\kappa = 1$).

The high structural and behavioural similarities between muscle sarcomeres and stress fibres justifies the use of models which were derived for the growth of stresses in muscle sarcomeres, to describe the fundamental relations between kinematic and static components. The state of stress in these models was found to be dependent on both, the strain [156], and the strain rate [103]:

$$\frac{\sigma^a}{\sigma_0} = f(\varepsilon)\, g(\dot{\varepsilon}) \tag{4.5}$$

where $f(\varepsilon)$ and $g(\dot{\varepsilon})$ are two independent functions depending on the strain (ε) and the corresponding strain rate ($\dot{\varepsilon}$), respectively.

4.2.2. Stress-strain rate relation:

The function $g(\dot{\varepsilon})$, which represents the growth of stress in the stress fibres due to the strain rate is assumed to follow a Hill-type growth. Here, a modified, smooth non-linear version of the Hill model [10, 103, 115], based on the linear piecewise continuous model [112], is used:

$$g(\dot{\varepsilon}) = \frac{1}{1+\frac{S_{exp}}{\sqrt{(S_{exp}^2+1)}}}\left(1+\frac{\bar{k}_v\frac{\dot{\varepsilon}}{\dot{\varepsilon}_0}+S_{exp}}{\sqrt{\left(\bar{k}_v\frac{\dot{\varepsilon}}{\dot{\varepsilon}_0}+S_{exp}\right)^2+1}}\right) \tag{4.6}$$

where S_{exp} is an expansion parameter which introduces a uniform behaviour for both positive and negative strain rates with $S_{exp} = 0$ and a non-uniform behaviour for $S_{exp} > 0$, as shown in Figure 4.3.

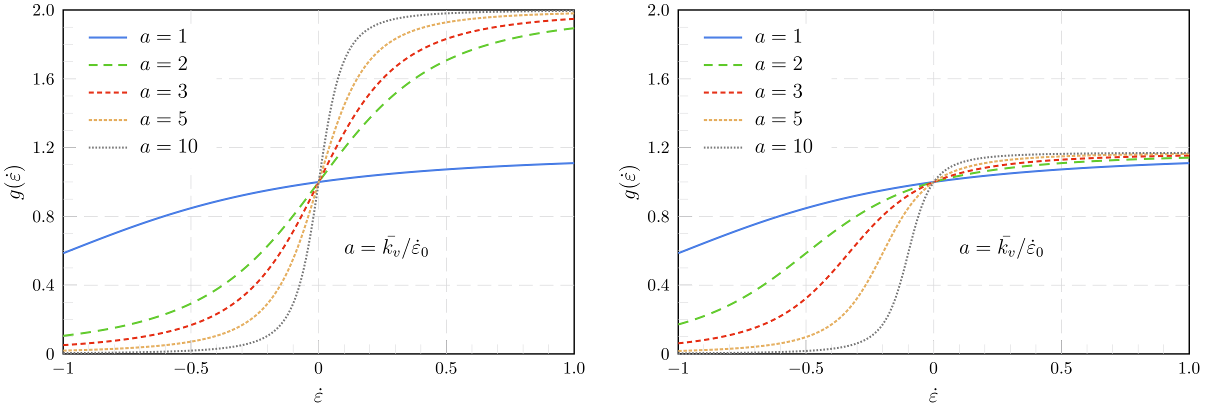

$S_{exp} = 0$ $S_{exp} = 1$

Fig. 4.3: Hill model behaviour for different values of expansion parameter S_{exp}. Behaviour is uniform for $S_{exp} = 0$, while it is non-uniform for $S_{exp} = 1$.

The expansion parameter S_{exp} becomes significant only when the cell is subjected to cyclic loading [10, 113], and hence in all the numerical examples presented in this thesis, S_{exp} is chosen to be 1 for problems with cyclic loading and 0 otherwise. The Hill constant $\bar{k}_v$ is a dimensionless constant for the dissociation of contraction and $\dot{\varepsilon}_0$ is a parameter representing the strain rate sensitivity. From Eq. 4.6 and Fig. 4.3, the following overall model behaviour can be observed:

(i) the function g tends to zero when the strain rate increases to minus infinity:

$$\dot{\varepsilon} \to -\infty : \qquad g(\dot{\varepsilon}) \to 0 \tag{4.7}$$

This implies that the stress fibre dissociates and the stresses cannot grow when the stress fibre is subjected to a very high negative strain rate.

(ii) as the strain rate increases positively, $g(\dot{\varepsilon})$ converges towards a stationary point

$$\dot{\varepsilon} \to +\infty : \qquad g(\dot{\varepsilon}) \to \frac{2}{1 + \frac{S_{exp}}{\sqrt{(S_{exp}^2 + 1)}}} \tag{4.8}$$

which is a constant greater than or equal to one. The corresponding plateau value depends on the expansion parameter S_{exp} and is equal to 2 for $S_{exp} = 0$.

(iii) For a zero strain rate, i.e. the isometric state, for all values of S_{exp},

$$g(0) \;=\; 1. \tag{4.9}$$

reducing the model to a purely static model response.

4.2.3. Stress-strain relation:

It was observed that, in addition to the strain rate of the applied loading, stress in muscle sarcomeres are found to depend on the strain as well [156]. Hence the model has to be updated by including stress-strain relation. The stress-strain relation can be derived in analogy to the characteristics of cables which are stiff in tension but which have no stiffness in compression. Thus, the stress will drop to zero for an increase of negative strains and will evolve for a positive strain value. A function for such a behaviour can be written as, cf [113]:

$$f(\varepsilon) = \begin{cases} \exp\left(-\left(\frac{\varepsilon}{\varepsilon_0}\right)^2\right) & \text{if } \varepsilon < 0 \\ \exp\left(-\left(\frac{\varepsilon}{\varepsilon_0}\right)^2\right) + \left(\frac{\varepsilon}{\varepsilon_1}\right)^2 & \text{if } \varepsilon \geq 0 \end{cases} \tag{4.10}$$

where ε_0 is a decay constant for the contraction when the strain becomes negative and where the constant ε_1 characterizes the passive strain hardening. Following [113], the ratio $\varepsilon_1/\varepsilon_0$ is kept constant at a value of 1.4. For $\varepsilon = 0$, $f(\varepsilon) = 1$, maintaining the unit value at the isometric state. With Eq. 4.3 and the relations 4.6 and 4.10 the active stress follows as

$$\sigma^a(\phi) \;=\; \eta(\phi)\,\sigma_{max}\, f(\varepsilon) g(\dot{\varepsilon}) \tag{4.11}$$

representing the active stress in a stress fibre in the direction ϕ.

In order to describe the anisotropic stress fibre contraction within the cell, a 2-dimensional homogenization is used to evaluate the stress tensor:

$$\boldsymbol{\sigma} \;=\; \frac{1}{\pi}\begin{bmatrix} \sigma_{11} & \sigma_{12} \\ \sigma_{21} & \sigma_{22} \end{bmatrix} \tag{4.12}$$

with

$$\begin{aligned}\sigma_{11} &= \int_{-\pi/2}^{\pi/2} \sigma^a(\phi)\, cos^2(\phi)\, d\phi \\ \sigma_{12} &= \int_{-\pi/2}^{\pi/2} \frac{1}{2}\sigma^a(\phi)\, sin(2\phi)\, d\phi \\ \sigma_{11} &= \int_{-\pi/2}^{\pi/2} \frac{1}{2}\sigma^a(\phi)\, sin(2\phi)\, d\phi \\ \sigma_{22} &= \int_{-\pi/2}^{\pi/2} \sigma^a(\phi)\, sin^2(\phi)\, d\phi.\end{aligned}$$

The strain and strain rate along the fibre with inclination angle ϕ are obtained by a similarity transformation in the 2D-plane using the inclined basis vectors:

$$\begin{aligned}\varepsilon(\phi) &= \varepsilon_{11}\, cos^2(\phi) + \varepsilon_{22}\, sin^2(\phi) \\ &\qquad + \varepsilon_{12}\, sin(2\phi) \qquad (4.13) \\ \dot{\varepsilon}(\phi) &= \dot{\varepsilon}_{11}\, cos^2(\phi) + \dot{\varepsilon}_{22}\, sin^2(\phi) \\ &\qquad + \dot{\varepsilon}_{12}\, sin(2\phi). \qquad (4.14)\end{aligned}$$

The contractile deformation of the stress fibres is confined by the passive resistance of the cytoskeleton through the intermediate filaments and other components in the cytoplasm. For simplicity, material offering such resistance is assumed to be isotropic and the stress-strain behaviour as linear elastic,

$$\sigma^p = E\,\varepsilon \qquad (4.15)$$

where σ^p denotes the passive stress, E is the passive elastic modulus and ε is the axial fibre strain. In three dimensions, total stress can be written as the sum of active and passive stress components:

$$\Sigma_{ij} = \sigma^a_{ij} + \left(\frac{E\nu}{(1-2\nu)(1+\nu)}\, \varepsilon_{kk}\delta_{ij} + \frac{E}{1+\nu}\varepsilon_{ij} \right) \qquad (4.16)$$

where ν denotes the Poisson's ratio and δ_{ij} is the Kronecker delta. Mechanical equilibrium can be evaluated by solving Eq. 4.17 using plane stress condition.

$$\Sigma_{ij,j} = 0 \tag{4.17}$$

2D cell supported by springs: Consider a cell supported by linear springs at the corners as shown in Fig. 4.4(A). When the system is initiated by an ad-hoc exponentially decaying calcium signal, stress fibre starts to grow. Solving the model by applying the traction boundary conditions exerted by the springs,

$$T_i = -K_E U_i \tag{4.18}$$

where T represents the traction exerted by the spring with stiffness K, and U represents the displacement, it can be seen that stress fibre concentration is higher near the edges where springs are connected than at other regions of the cell, as seen in Fig. 4.4(B). The average value of stress fibre concentration ($\bar{\eta}$) is evaluated by averaging the value over the range $-\pi/2$ to $\pi/2$.

$$\bar{\eta} = \frac{1}{\pi} \int_{-\pi/2}^{\pi/2} \eta(\phi)\, d\phi \tag{4.19}$$

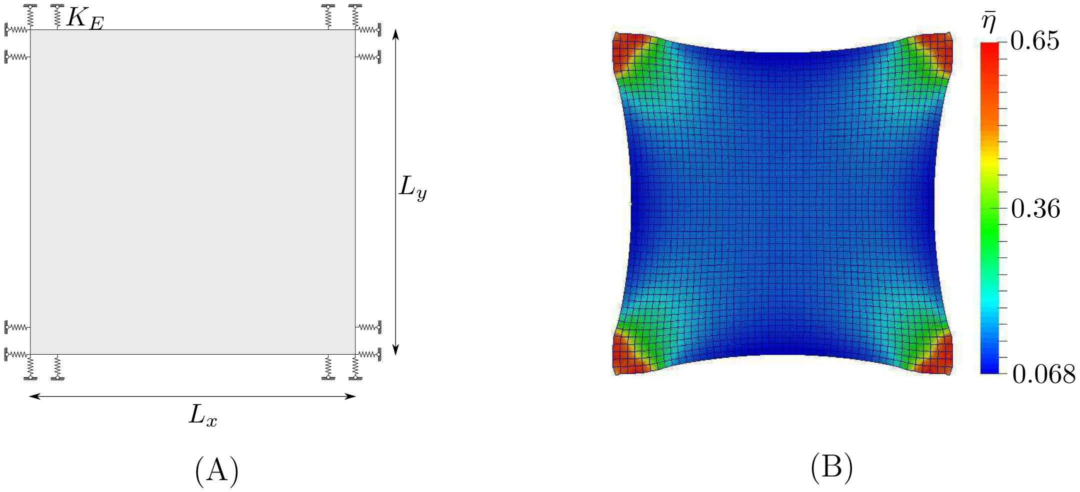

(A) (B)

Fig. 4.4: (A) Schematic of a cell supported by springs at the corners. $K_E = 1e5 N/m^2; L_x = 25e-6m; L_y = 25e-6m$. (B) Stress fibre concentration $\bar{\eta}$ shows that the concentration is higher at the corners (Scale factor=2).

Though this numerical example showed that the stress fibre model could predict right stress fibre growth response based on the substrate properties, in reality, cells are not placed on springs whose properties are known. But cells have spring like structures on the cell membrane, termed focal adhesions, to sense the stimuli exerted by the extra cellular matrix.

4.3. Focal adhesion growth

Focal adhesions are made up of multi-protein structures, containing integrins at the bottom most layer, that form a mechanical link between the cytoskeleton and the extra cellular matrix [52]. Experiments reveal that integrins exist in two conformational states: (i) a low affinity or bent state and (ii) a high affinity or straight state. Integrins in the straight state are assumed to form a bond with the substrate, while integrins in the bent state are free. Thus, for modelling purposes, the high affinity integrins can be assumed to represent the focal adhesions which form a bond between the cell and the substrate as shown in Fig. 4.5.

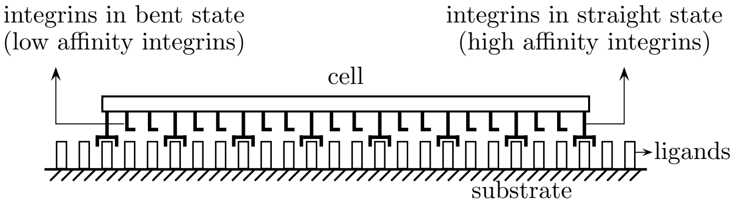

Fig. 4.5: Low and high affinity integrins in a 1-D cell attached to a soft substrate where the high affinity integrins are assumed to represent the focal adhesions.

The modelling of the focal adhesions follows a thermodynamical approach represented by the chemical potential for low and high affinity integrins [53, 116]:

$$\mu_L = \mu_L^R + k\,T\ ln\left(\frac{\xi_L}{\xi_0}\right) \tag{4.20}$$

$$\mu_H = \mu_H^R + k\,T\ ln\left(\frac{\xi_H}{\xi_0}\right) + \Phi - \bar{F}\,\Delta \tag{4.21}$$

where μ_L and μ_H are the chemical potentials of the low and high affinity integrins, respectively. Furthermore, μ_L^R and μ_H^R are the reference chemical potentials while ξ_L and ξ_H

are the concentrations of the low and high affinity integrins, respectively. The Boltzmann constant is denoted by k and the absolute temperature by T. Furthermore, ξ_0 denotes the reference integrin concentration [53]. A comparison of (4.20) and (4.21) reveals two additional terms in (4.21) which result from the fact that, due to bonding with the substrate the potential of the high affinity integrins depends on the tensile force they are subjected to [52]. The bond energy is denoted with Φ, while $(\bar{F}\,\Delta)$ denotes the work done by the bond while being stretched by Δ. Thus, the force exerted by the bond can be evaluated from the bond energy Φ as

$$\bar{F} \;=\; \frac{\partial \Phi}{\partial \Delta} \quad . \tag{4.22}$$

The model is based on the following assumptions and relations:

- at thermodynamic equilibrium, the chemical potentials of high and low affinity integrins must be equal. Thus,

  $$\mu_H \;=\; \mu_L \tag{4.23}$$

  will result in the inter-conversion of integrins from a low to a high affinity state and vice versa. From (4.20), (4.21) and (4.23), the relation between high and low affinity integrins reduces to

  $$\frac{\xi_H}{\xi_L} \;=\; \exp\left(\frac{\mu_L^R - \mu_H^R - \Phi + \bar{F}\,\Delta}{k\,T}\right) . \tag{4.24}$$

- In the FA models of [53, 116], low affinity integrins were assumed to move along the cell membrane which was modelled by a diffusion equation, satisfying zero-flux boundary conditions. Since the diffusion of low affinity integrins does not contribute to the focal adhesion formation through inter-conversion of integrins, the diffusion of integrins was neglected and the conservation of the total number of integrins was assumed through

  $$\xi_0 \;=\; \xi_L + \xi_H \tag{4.25}$$

  where ξ_0 is the total number of integrins in the system which is inter-converted between low affinity and high affinity integrins based on their potential. Substitution of Eq. (4.25) into (4.24) gives:

$$\xi_L = \frac{\xi_0}{1+\alpha} \tag{4.26}$$

$$\xi_H = \frac{\xi_0 \alpha}{1+\alpha} \tag{4.27}$$

with

$$\alpha = \frac{\xi_H}{\xi_L} \quad . \tag{4.28}$$

- the bond energy Φ in the high affinity integrins is assumed to depend on the stretch quadratically:

  $$\Phi = \frac{1}{2}\lambda_s \Delta_e^2 \tag{4.29}$$

  where $\Delta_e = \sqrt{\Delta_1^2 + \Delta_2^2}$ is the effective stretch, and Δ_1 and Δ_2 represent the stretches in x_1 and x_2 directions, respectively, while λ_s represents the bond stiffness; so that:

  $$\bar{F} = \lambda_s \Delta \quad . \tag{4.30}$$

- the stretch rate is related to the rate of displacement as

  $$\dot{\Delta} = \begin{cases} \dot{u} & \Delta_e \leq \Delta_{max} \\ 0 & \text{otherwise} \end{cases} \tag{4.31}$$

  where Δ_{max} is the maximum allowable stretch in the stress fibres.

In summary, the FA model reflects the following behaviour: integrins subjected to an external force, respond either by the formation or dissociation of focal adhesions. If more focal adhesions are needed to maintain equilibrium, low affinity integrins are converted to high affinity integrins through the thermodynamic equilibrium. The total number of integrins in the system is preserved.

Solution to the problem of cell contractility coupled with focal adhesion growth can be obtained by solving the mechanical equilibrium subjected to traction due to focal adhesion as given in [53],

$$b \, \Sigma_{ij,j} = -T_i \tag{4.32}$$

where Σ is the total stress in the stress fibre as given in Eq. 4.16, b is the thickness of the cell, and T_i is the traction force exerted by focal adhesion on the cell, evaluated as

$$T_i = -\xi_H \bar{F}_i \tag{4.33}$$

where, ξ_H is the high affinity integrin concentration and $\bar{F}_i$ is the force exerted by the cell, evaluated as

$$\bar{F}_i = \lambda_s \Delta_i \tag{4.34}$$

where, Δ represents the stretch of the high affinity integrins, as given in Eq. 4.31.

4.4. Calcium signalling growth and feedback

Essential processes of a living cell such as mechanosensing or the growth of stress fibres involve multiple proteins including adaptor proteins such as talin, and vinculin; kinase, and phosphatase such as FAK; cytoskeletal components such as actin filaments, and microtubules and their interactions [157]. Though the behaviour of each of these individual proteins is clear to some extent, the combined actions and its effect on the cellular properties are not understood completely. Integrins on the cell membrane receive signals from the ECM resulting in the activation of inositoltriphosphate (IP3) messenger molecules. The IP3 molecules diffuse through the cytoplasm and attach themselves to the receptors on the endoplasmic reticulum and release free calcium ions (Ca^{2+}). The Ca^{2+} ions thus available in cytoplasm bind to the calcium modulated protein calmodulin and activate the calmodulin dependent protein kinase (CaMKII), which leads to the activation of the small GTPase enzyme RhoA [158]. Further, RhoA and its downstream effector Rho-associated kinase (ROCK) act as principal mediators for the growth of tension in the cytoskeleton [159]. ROCK is found to attach to myosin phosphatase, inhibiting phosphatase activity and thereby increasing myosin phosphorylation. In addition, they are also attached to LIM kinase (LIMK) which generates actin monomers, together promoting stress fibre contractility through the formation of an acto-myosin bridge complex [160], cf Fig. 2.2.

The formed actomyosin complex will generate stress fibres which lead to focal adhesion growth [54]. Simultaneously, the focal adhesion growth manipulates the RhoA signalling and hence the growth of stress fibres. In [161] it was shown that cells placed in suspension showed an increased level of RhoA, but low phosphorylation and hence low stress fibres. This indicates that the mechanisms in the cell are interconnected and there exists a feedback loop between the focal adhesion formation, the calcium concentration, the myosin phosphorylation and the stress fibre generation as illustrated in Fig. 4.6. The concentration of calcium which is released from the endoplasmic reticulum stores into the cytoplasm is regulated by mitochondria, thus keeping its concentration under a limit.

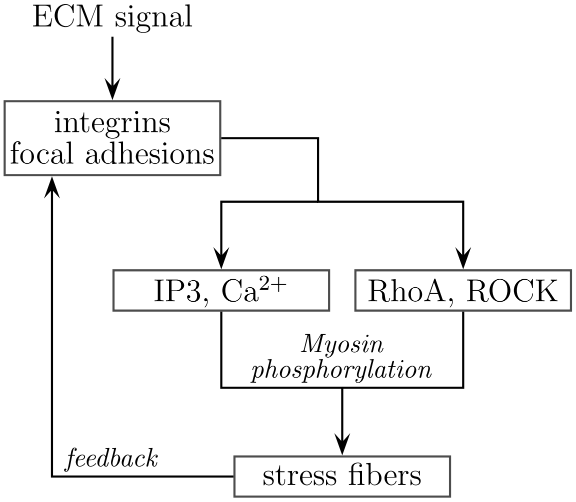

Fig. 4.6: Signalling feedback within a cell. Signal coming from ECM, sensed by focal adhesion, results in the diffusion of IP3 leading to growth of Ca^{2+}. In the presence of RhoA, and ROCK, myosin phosphorylates to form stress fibres, which leads to change of focal adhesion concentration, resulting in a feedback loop.

Due to different time scales of each of these processes, periodic spikes are observed over time in the calcium concentration [162] which are lost again with an increasing degree of stimulation of the receptor. Since the focal adhesions are assumed to be fully grown and play the role of receptors, high receptivity can be assumed and thereby neglect the spiking behaviour of calcium.

In Fig. 4.7, the generation of calcium within the cytoplasm is illustrated depicting the following mechanism: (i) the receptor-initiated hydrolysis of phosphatidylinositol 4,5-bisphosphate (PIP2) by phospholipase C (PLC) results in the formation of inositol 1,4,5-triphosphate (IP3) and diacylglycerol. (ii) IP3 is further hydrolysed to be released as IP2, while some of IP3 molecules attach themselves to the calcium gates at the endoplasmic reticulum (ER). This attachment opens the calcium channels and releases calcium to the cytoplasm. (iii) In order to maintain the calcium concentration within the cytoplasm, the ER absorbs some of the calcium ions in the cytoplasm, while some of the calcium passes the cell membrane through mitochondria. Thus, calcium present in the cytoplasm results in the myosin phosphorylation, which, in turn, leads to the formation of stress fibres and focal adhesion as described in Section 4.3.

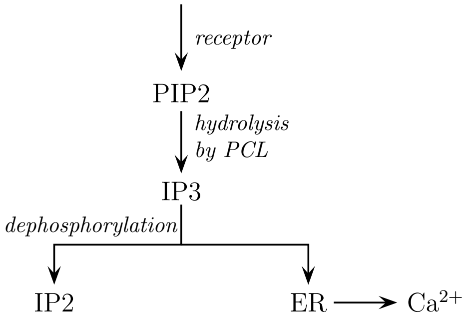

Fig. 4.7: Generation and release of calcium. Hydrolysis of PIP2 molecules results in the formation of IP3. It further dephosphorylates, and attach to endoplasmic reticulum leading to release of Ca^{2+} into the cytoplasm.

From a mechanobiology point of view, the generation of calcium within the cytoplasm can be considered as a two-step process, where the generation of IP3 is modelled by a reaction-diffusion equation followed by a rate equation representing the calcium growth. In this regard, the calcium growth model which includes a mechanosensitive feedback [117] is used:

$$\dot{\bar{S}} \;=\; m_s\,k\,T\,\frac{\partial^2 \bar{S}}{\partial x_i^2} - k_d\,\bar{S} + \frac{\alpha_c}{b}\,max(0,\dot{\xi}_H) - \bar{S}\,\dot{\varepsilon}(\phi) \tag{4.35}$$

where $\bar{S}$ is the IP3 concentration, $x_i\,(i = 1, 2)$ is the spatial coordinate and m_s is the mobility of IP3. The reaction terms involve the rate constant k_d for the hydrolysis of IP3 into IP2, a non-dimensional proportionality constant α_c and the rate value $\dot{\xi}_H$ representing the change of the FA concentration. The strain rate of the stress fibres at an angle ϕ is represented by $\dot{\varepsilon}(\phi)$.

From equation (4.35), it follows that some of the produced IP3 is diffused through the cytoplasm to reach the endoplasmic reticulum gates and some of the produced IP3 is hydrolysed to IP2 without having an effect on calcium generation. The growth of IP3 is affected only when new focal adhesions are formed but remains unaffected when focal adhesions are dissociated. The growth of calcium depending on the available IP3 can be written as given in [117]:

$$\dot{C} \;=\; \lambda_f \, \frac{\bar{S}}{\bar{S}_0} \, (1 - C) - \lambda_b \, C \tag{4.36}$$

where C represents the calcium concentration and λ_f and λ_b are the forward and backward rate constants, respectively. The boundary condition is chosen to be $\nabla \bar{S}.\mathbf{n} = 0$, with $\mathbf{n}$ representing the unit normal vector, on all boundaries of the analysis domain and the initial condition at $t = 0$ is chosen as $\bar{S}(0) = \bar{S}_0$ and $C(0) = 0$. From (4.36) it follows that $C = 0$ when $\bar{S} = 0$. This implies that there is no calcium without IP3, and hence no phosphorylation.

The calcium concentration C obtained from Eq. (4.36) is used in Eq. (4.1) to evaluate the stress fibre concentration. Thus, equations Eq. (4.35) and Eq. (4.36) together represent the feedback loop that exist within the cell, where calcium concentration is affected by the focal adhesion formation that is governed by the mechanical equilibrium of the cell. The resulting calcium concentration affects the stress fibre formation which changes the focal adhesion concentration, and thereby closes the signalling cycle. Solution to the system of equations thus developed were obtained following the small strain assumption. More details about the coupling and solution schemes, and their comparisons in a generalised large displacement formulation is given in Chapter 5.

4.4.1. External force induced focal complex formation

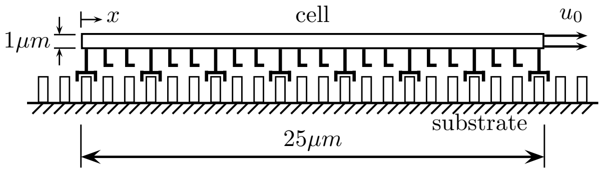

$\bar{k}_v$ = 1.0 Hill constant
k_f = $1.4e-4\,s^{-1}$ rate of formation
k_b = $1.4e-5\,s^{-1}$ rate of dissociation
ε_0 = $1.0e-2$ strain constant
$\dot{\varepsilon}_0$ = $1.0e-2\,s^{-1}$ strain rate sensitivity

Fig. 4.8: 1D cell representation with prescribed displacement.

In a series of optical trap experiments *Galbraith et al.* have revealed ‘The relationship between force and focal complex development’ [70] and shown that an external force acting

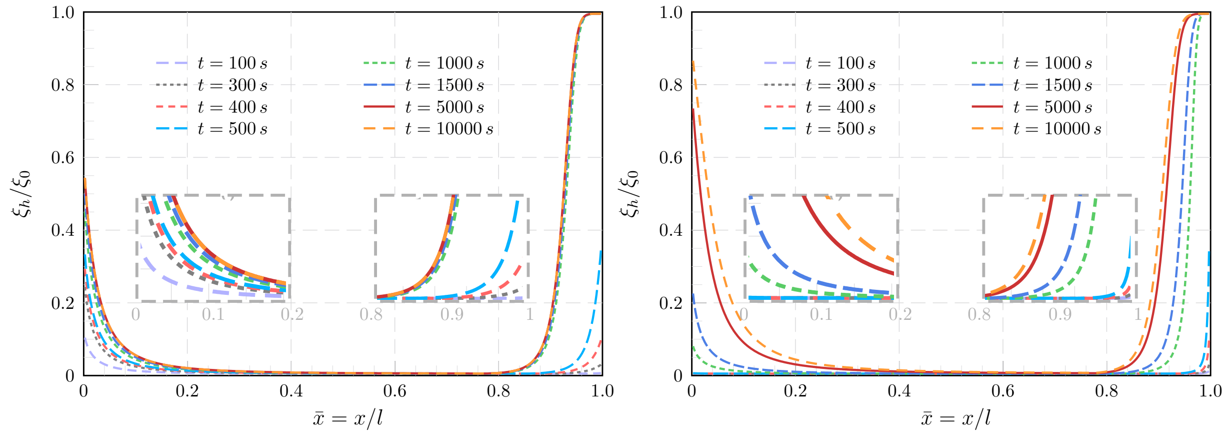

(a) *without* feedback loop (b) *with* feedback loop

Fig. 4.9: Focal adhesion growth matches the experimental observations only upon the application of a feedback loop.

on the cell results in the focal complex formation, even when placed on a ligand-coated surface where the cell is unable to develop focal adhesion complexes by itself. Furthermore, it was observed that vinculin, which is a marker for both focal complex and focal adhesion, did not change over tens of minutes, confirming the applicability of the FA model. A tight coupling of external forces and a focal adhesion formation was shown earlier in [67] and is studied in the following numerical example taken from [117].

A 1-D cell is placed on an infinite rigid substrate and is subjected to a prescribed displacement u_0 at one end of the cell, as depicted in Fig. 4.8. The material parameters are specified in Table 4.1 and additional model parameters as specified in Fig. 4.8. Pursuant to the experimental and numerical observations, the focal adhesions are expected to form initially near the end where the displacement is prescribed and eventually to form at the other end of the cell due to its mechano-sensitive properties.

The numerical experiment was performed with and without feedback loop to demonstrate its importance for a reliable and correct result. For the case where no feedback mechanism was considered, an ad-hoc calcium signal $C = \exp(-t)$ was used instead of Eq. 4.36 to trigger the stress fibre growth coupled to focal adhesion formation [112]. Without the feedback mechanism the focal adhesion concentration increases initially at the free left end of the cell while the force was applied at the right end, cf Fig. 4.9(a). Even at the loaded end of the cell growth of focal adhesions was observed only after a time greater than 500s. Conversely, an almost immediate growth was apparent at the left end of the cell. Hence, the simulated development of an initial focal adhesion growth on the left end

parameter	**symbol**	**unit**	**value**
Passive elastic modulus	E	kPa	0.08
Poisson's ratio of cell	ν		0.3
Tensile strength of stress fibres	σ_{max}	kPa	20
Maximum stretch	Δ_{max}	m	$1.30e-7$
Focal adhesion bond stiffness	λ_s	N/m	$1.50e-5$
Boltzmann constant	k_b	m^2 kg s^{-2} K^{-1}	$1.38e-23$
Temperature	T	K	310
Difference between reference chemical potentials of high and low affinity integrins	$\Delta\mu$	m^2 kg s^{-2}	$5\ k_bT$
Reference integrin concentration	ξ_0	integrins/m^2	$5.0e+15$
IP3 mobility constant	m_s	s/kg	$1.0e+10$
IP3 diffusion proportionality constant	α_s		10
IP3 de-phosphorylation rate constant	k_d	s^{-1}	$5.0e-4$
Reference IP3 concentration	s_0	molecules/m^3	$1.0e+21$
Forward rate constant of Calcium release	λ_f	s^{-1}	1.0
Backward rate constant of Calcium release	λ_b	s^{-1}	0.5

Table 4.1: Applied model parameters following [112].

of the cell contradicts the experimental observations.

Next, the ad-hoc calcium signal was replaced with the feedback loop as given by eqs. (4.35) and (4.36). The effect of the feedback loop is illustrated in Fig. 4.9(b). The concentration of cytoplasmic calcium changes within the cytoplasm which affects the growth of stress fibres and hence the focal adhesions. Initially, the focal adhesion concentration was higher at the right end of the cell where the prescribed force was applied. Eventually, focal adhesions grew on the other end of the cell as well. At the state of equilibrium, the focal adhesion concentration was highest at the boundary of the cell, matching the experimental observations [69].

4.4.2. Interdependence of focal adhesions and stress fibres

With the next numerical experiment, the feedback-loop extended model is used to demonstrate the dynamic coupling of stress fibres and focal adhesions. To this end, the effect of ROCK inhibition is simulated which will demonstrate the suspension of focal adhesion growth and thus, of stress fibre growth.

ROCK (Rho-associated protein kinase) is an enzyme which plays a major role in the stress fibre formation, cf. section 4.4. In [163] it was shown that ROCK inhibition diminishes the myosin phosphorylation within the cytoplasm and hence reduces the measured tractions by almost 50%. This reduces the cytoskeletal tension and hence the stress fibre concentration. It was also found by vinculin staining that the ROCK inhibitor results in a reduced concentration of focal adhesion. Further, it was observed in suspended cells that the activity of RhoA is high, but the concentration of stress fibres is low due to reduced phosphorylation [161]. Furthermore, adhesion is required for the GTP-bound RhoA to activate ROCK [159]. In summary, these experimental observations show that by suspending the growth of stress fibres through ROCK inhibition, the focal adhesion growth is suspended. Based on the inter-dependence between calcium, stress fibres and focal adhesion as illustrated in 4.4.1, it could be hypothesized that stress fibre growth is suppressed by inhibition of focal adhesion growth.

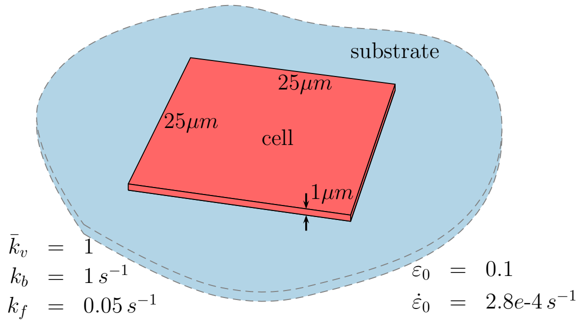

Fig. 4.10: Square cell model on an infinite substrate.

In the model, the strong link between ROCK and myosin phosphorylation is brought about by calcium signalling through the feedback loop as given by eqs. (4.35) and (4.36). The phosphorylation leading to stress fibre growth is activated by a signalling calcium concentration which can be derived from reference concentrations of IP3 and ξ_H. The stress fibre growth leads to a new equilibrium state for the cell, which again changes the focal adhesion concentration and thus completes the feedback loop. When the focal adhesion growth is inhibited, either indirectly by ROCK inhibitors or by keeping the cell in a suspension, the calcium signal decays and prevents further growth of stress fibres which indicates the absence of phosphorylation. Alternatively, by inhibiting the growth of focal adhesion, an increase in the traction force $\xi_H F$ is prevented. This affects the mechanical equilibrium and results in reduced contractile stress, and hence an increased stress fibre dissociation.

The influence of focal adhesion on stress fibres is considered with a two-dimensional cell placed on an infinite substrate depicted in Fig. 4.10. In addition to the parameters shown in the figure, the material parameters are used according to Table 4.1. Two different conditions are taken into consideration: with the first condition the focal adhesion is allowed to grow as a force-dependent mechanism, following the thermodynamic equilibrium of (4.23), while in the second condition, the focal adhesion is maintained at its initial value ξ_0. The second condition represents the behaviour of cells subjected to ROCK inhibition or cells in a suspended state.

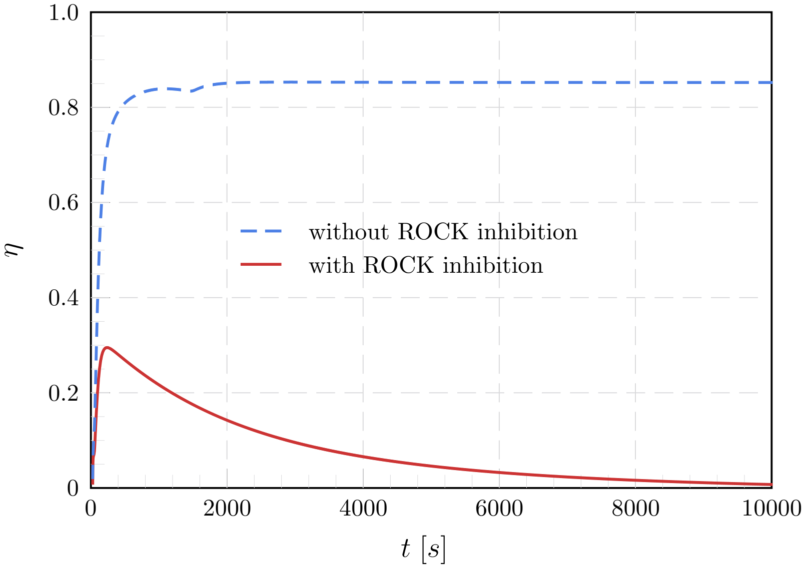

Fig. 4.11: Stress fibre growth over time: Stress fibres collpase due to ROCK inhibition.

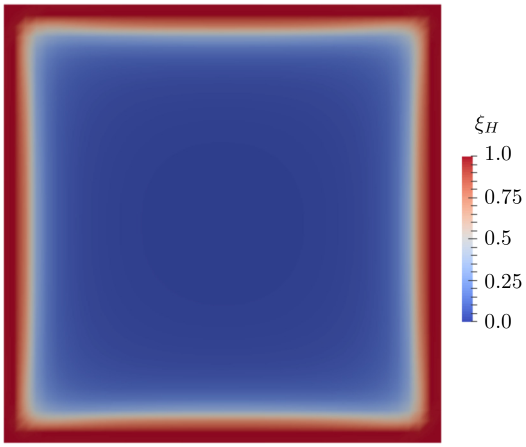

Fig. 4.12: Focal adhesion growth on a square cell.

The results of the stress fibre growth analysis are depicted in Figure 4.11. The stress fibre concentration of cells under contraction considering ROCK inhibition drops due to the absence of focal adhesion growth. In contrast, when focal adhesion growth is not restrained, stress fibres are formed significantly. Due to the different time scales of focal adhesion and IP3 growth, the stress fibre growth without ROCK inhibition exhibits a small kink around $t = 2000s$. But, since this did not affect the equilibrium nature of the cell, the rate constants were not changed. The growth of focal adhesion on the square test cell is depicted in Fig. 4.12. The focal adhesion growth is higher on the boundary of the cell than at the centre which fully corresponds to the observed experimental growth pattern presented in [69].

4.5. Stress fibre reorientation

The cyclic loading experiments presented in Chapter 3 showed that, when cells were subjected to a uniaxial cyclic loading, stress fibres were formed in directions away from the direction of loading. And the cells were found to reorient along the direction of stress fibres. The degree of reorientation was found to depend on the substrate and the loading parameters as observed in Chapter 3 and also in literature [7, 8]. The potential of the model developed in earlier sections will be shown by simulating the problem of stress fibre reorientation. Cyclic loading in uniaxial and biaxial directions will be considered with changing loading and substrate properties.

Experimental studies, performed on cells subjected to cyclic loading, usually involve a large number of samples followed by evaluating a statistical average to estimate the quantitative behaviour. To this end, cells are grown on a substrate, which is attached to the loading mechanism, applying necessary cyclic loading. Cells are then fixed, stained for actin and imaged using fluorescence microscope. The results are presented as circular histogram, which represent the mean behaviour of cells. Thus, since the model presented in this thesis is deterministic, results are assumed to simulate such average results. In the following study, a 2D cell placed on a supporting substrate is modelled, cf. Fig. 4.13. A strain loading is applied to the substrate which leads to evaluating substrate stresses according to

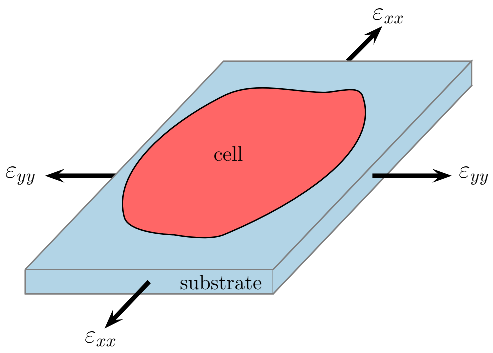

Fig. 4.13: Cell placed on a substrate which is subjected to in-plane loading $\varepsilon_{ii}, i = x, y$, representing a strain loading applied on the substrate.

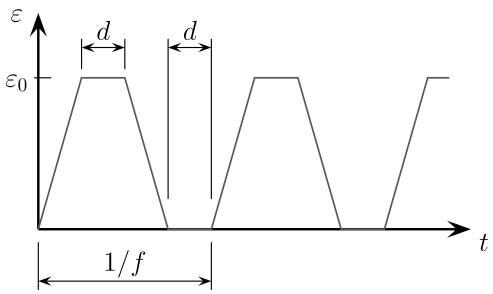

Fig. 4.14: Principle cyclic stretch loading. ε_0 indicates the maximum amplitude of the applied cyclic load, f denotes the frequency.

$$\sigma_{ij}^{sub} = C_{ijkl}^{sub}\, \epsilon_{kl}^{0} \tag{4.37}$$

where C_{ijkl}^{sub} is the plane-stress elasticity tensor of the substrate and ϵ_{kl}^{0} is the strain applied to the substrate. The substrate stress is then added to the total stress, to update Eq. 4.32 as

$$b\, \left(\Sigma_{ij} + \sigma_{ij}^{sub}\right)_{,j} = -T_i \; . \tag{4.38}$$

It is to be noted here that including substrate stress in the mechanical equilibrium equation implies that substrate is part of the cell, which appears to be non-physical. The addition of substrate stress to the total stress in the cell is thus a simplification carried out, which otherwise would be a problem involving contact between the cell and the substrate and thereby would involve solving for their equilibriums individually. The computed results are compared qualitatively with the average experimental results. Stress fibres in 20 orientations distributed uniformly between 0 and $\pi/2$ are considered. In accordance with the experiments the analysis results are presented with circular histograms in which the inclination of each line represents the corresponding stress fibre orientation and the magnitude of the length of the line represents the stress fibre concentration η in that direction. Unlike the results in Chapter 3 where fibres were analysed over $-\pi/2$ to $\pi/2$, the model considers only a quarter of the analysis domain using symmetry boundary conditions. The circular histogram between $\pi/2$ and 2π follows from the symmetry conditions. As observed during the experiments, at equilibrium, the orientation of a cell and stress fibres match each other, and hence the terminology cell and stress fibre reorientation, respectively, can be used interchangeably.

Direction of loading: In [78] it was observed that cells subjected to biaxial loading do not exhibit a significant realignment while cells subjected to uniaxial loading do, which is usually termed *strain avoidance*. In a first analysis, a horizontal uniaxial linear triangular cyclic loading is applied to the substrate, depicted in Fig. 4.14. The substrate has a stiffness of 20 kPa and all loading conditions were considered for uniaxial loading according to Table 4.2 in which d denotes a time span as defined in Fig. 4.14.

	frequency [mHz]	amplitude ε_0	d [s]
(a)	52	0.049	3
(b)	34	0.084	3
(c)	21	0.140	3
(d)	9	0.320	3

Table 4.2: Different applied cyclic loading conditions.

In Fig. 4.15 the results of the horizontal uniaxial loading is shown in terms of circular histograms. With increasing load amplitude, the stress fibres increasingly realign in directions away from the loading direction. In the stress fibre model, the dissociation of stress fibres depends on the active stress. Thus, with increasing amplitude, the effect of dissociation is much more pronounced than the effect of association which matches the experimental observations presented in [8].

Generally, the active stress increases during the loading phase of a cycle and decreases during unloading. In Fig. 4.16, decrease of stress in the direction of loading is higher than in the orthogonal direction. The figure shows the variation of the active stress for

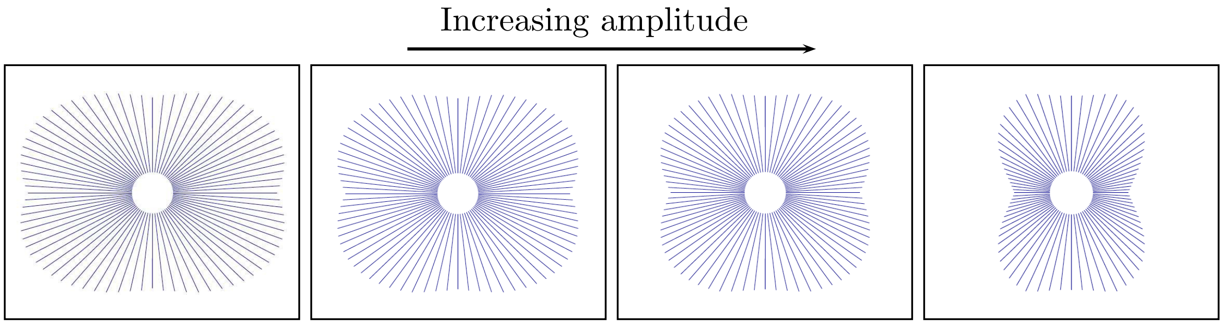

$\varepsilon_0 = 0.049$ $\varepsilon_0 = 0.084$ $\varepsilon_0 = 0.14$ $\varepsilon_0 = 0.32$

Fig. 4.15: Stress fibre reorientation due to uniaxial loading in the horizontal direction ($\longleftrightarrow$). Alignment becomes significant with increasing amplitude.

the last five loading cycles. The pronounced decrease of stress and the higher contractile strain results in a higher dissociation of stress fibres along the loading direction. Thus, at equilibrium, the stress fibre concentration is lower in the direction of loading compared to the orthogonal direction.

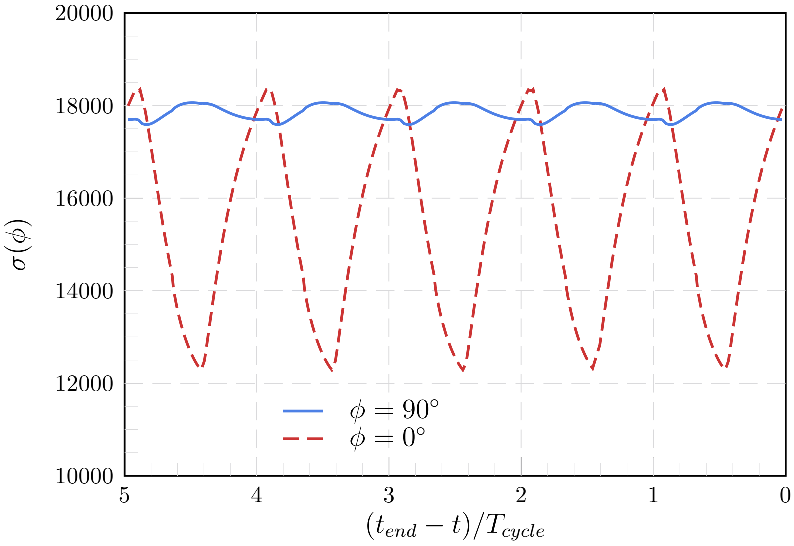

(a)Active Stress

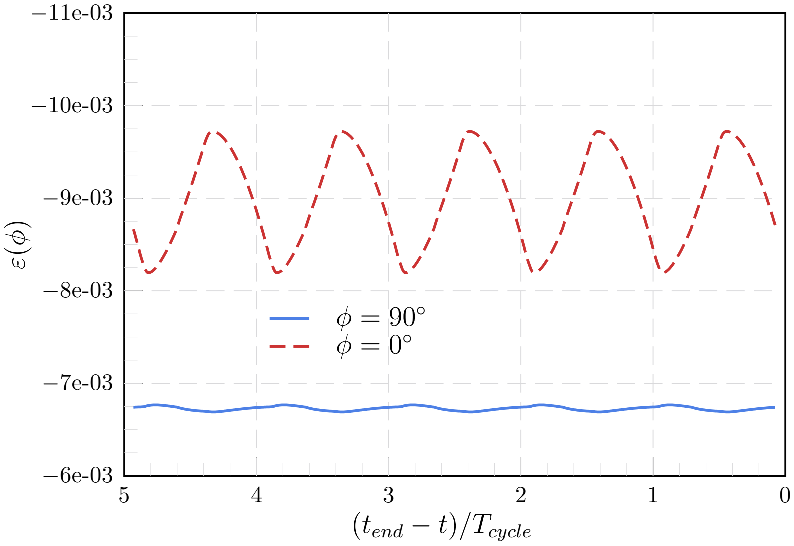

(b)Strain

Fig. 4.16: (a) Active stress and (b) strain in stress fibres along the loading and orthogonal directions and corresponding strain variation for the last five loading cycles.

Next, in order to study the realignment of stress fibres subjected to biaxial loading, cyclic loading is applied according to the condition (d), cf. Table 2, in both, horizontal and vertical directions, keeping all the material parameters constant. The stress fibre orientation for such a biaxial loading is shown in the circular histogram of Fig. 4.17. A strong contrast is observed between uniaxial loading and biaxial loading for the same loading parameters. It can be inferred that, cells do not exhibit a preferred reorientation angle, when subjected to biaxial loading as seen during the uniaxial loading.

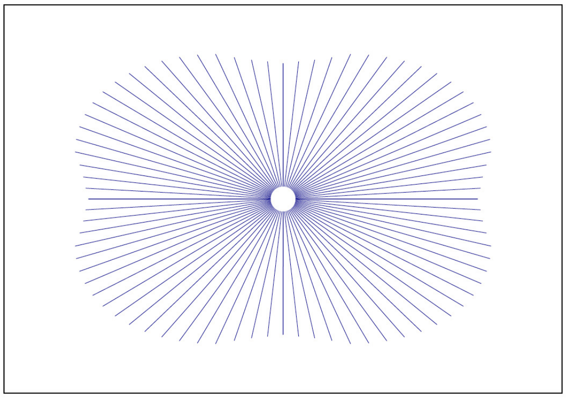

Fig. 4.17: Stress fibre orientation due to biaxial loading. Stress fibres exhibits no preferred direction when they are subjected to load in both x and y directions.

4.5.1. Effect of substrate properties

It has been observed experimentally that the properties of the substrate plays a prominent role in deciding the cellular reorientation response. In [8], it was observed that cells placed on substrates with stiffness values less than 11 kPa did not exhibit reorientation. In another set of experiments [7], it was shown that the stress fibres align along the direction of loading when the substrate was a soft collagen gel, and divert from the loading direction when the substrate is a stiff silicone rubber. In [102], stress fibres modelled as catch-bonds, also showed an increase of the contractile force with increasing substrate stiffness. To investigate this effect numerically, cell was placed on the substrate and uniaxial cyclic loading was applied as given in Fig. 4.14. Calculations were carried out for different values of substrate stiffness while all other material parameters were held constant. It was observed that the effect of applied cyclic loading becomes significant as the substrate stiffness increases, as seen in Fig. 4.18.

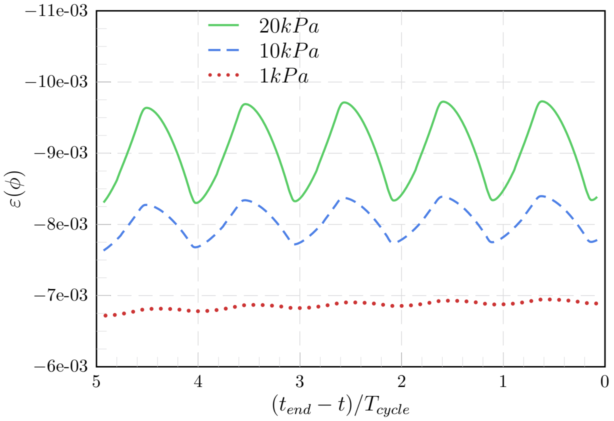

Fig. 4.18: Strain in stress fibres at $\phi = 0$ for the last 5 loading cycles. Influence of cyclic loading on contractile strain increases with substrate stiffness.

4.6. Summary

In this chapter, a mathematical model was introduced, developed as an extension of the existing models, that can simulate the cell contractility phenomenon leading to mechanotransduction behaviour observed in cells. It is a continuum level phenomenological model simulating the coupled effect of stress fibre and focal adhesion growths, including the feedback loop through the cytoplasmic concentration. The prominent features of the model were the dependence of the active stress in stress fibres on both the strain and the strain rate, in addition to the focal adhesion growth on the cell membrane. These fields were coupled through a feedback loop involving the cytoplasmic calcium concentration. Focal adhesion was assumed to be made up of integrins existing in two conformational states, in thermodynamic equilibrium. Evaluating the total stress in the cell and solving the mechanical equilibrium, unknown concentrations were obtained along with the displacement field. External strain loading applied to the substrate is transferred to the cell by adding the substrate stress to the total stress in the cell. Numerical examples illustrated the effect of feedback loop on the stress fibre growth. It was also possible to use the model to simulate the response of cells subjected to uniaxial cyclic loading. The effect of substrate stiffness on the response of cells and the direction of loading has been simulated using a single set of parameters. It has to be noted here that the solution to the numerical problems presented in this chapter were obtained following the small strain assumption, and monolithic coupling. In the following chapter, different coupling schemes and large displacement formulation will be derived, and the solution schemes will be compared.

5. Monolithic and staggered coupling schemes

The study of different solution methods for the bio-chemo-mechanical equations would reveal essential solution properties with regard to robustness and accuracy. In this chapter, solution methods, staggered and monolithic which follow different ways of coupling the governing equations are considered, as described in [13]. In this regard, consistent variational formulations and the corresponding algebraic equations tailored to the different solution methods have been considered for the cell contractility problem, described in Chapter 4. The basic differences of the solution schemes will be considered in terms of algorithmic aspects and are illustrated with a number of numerical experiments, including model refinement in space and time. Furthermore, sensitivity of the solution with regard to parameter variations representing different model properties and applied cyclic loading to understand the mechanisms of the stress fibre growth has been studied.

5.1. Coupling schemes

The mechanical equilibrium, Eq. (4.32), and the focal adhesion growth, Eq. (4.23), constitute a coupled model for the analysis of stress fibre growth through focal adhesion formation. The solution of the governing equations requires to consider the influence of one solution field on the other. The coupling can be performed following either *staggered* or *monolithic* approach, as depicted in Fig. 5.1.

In a staggered approach, cf. Fig. 5.1(a), the problem is solved in consecutive steps. The mechanical equilibrium assumes the focal adhesion formation, in terms of its high affinity integrin concentration (ξ_H), to be constant as obtained at the end of the previous time step t_{n-1}. The ξ_H concentration of the current time step t_n is used to evaluate the displacement field $\mathbf{u}$ of the following time step, t_{n+1}. Using the new displacement solution, the stretch is evaluated to update the ξ_H concentration. The coupling of $\mathbf{u}$ and ξ_H is done explicitly, which limits the size of the time step that can be used to ensure a stable and reliable solution.

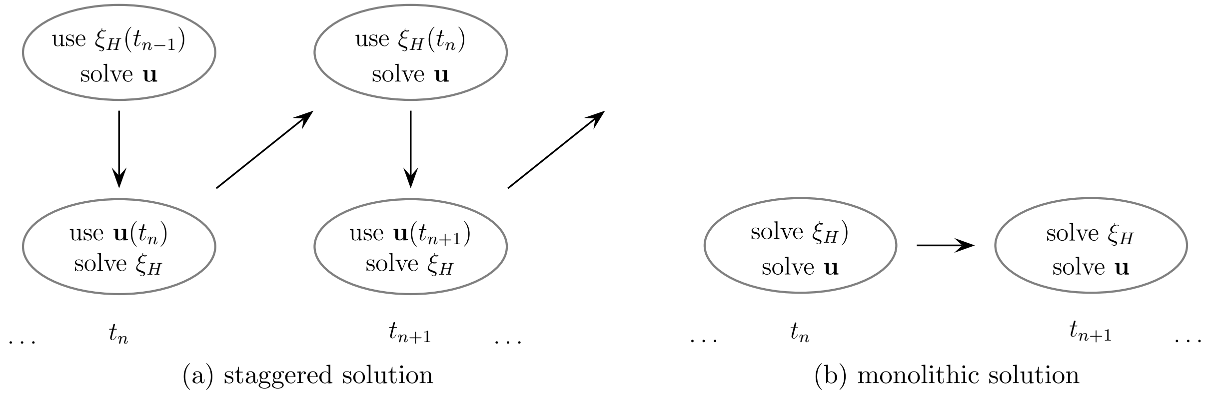

(a) staggered solution (b) monolithic solution

Fig. 5.1: Solution schemes for the coupled cell contractility and focal adhesion formation for (a) staggered solution, where the unknowns are solved for in two steps and (b) monolithic solution, where the unknowns are solved for in a single step.

Alternatively, the monolithic solution approach, cf. Fig. 5.1(b), couples the governing equations, Eq. (4.32) and Eq. (4.23) in a common system of equations to allow for the simultaneous solution of the unknown displacements $\mathbf{u}$ and high affinity integrin concentration ξ_H. Thus, both solution fields are assumed to be varying and thereby equilibrium is established together in an iterative solution scheme. In comparison with the staggered scheme, the size of the time step used in the monolithic scheme has minor effect on the solution quality since both solution fields are coupled implicitly and updated in a common step. In particular, the tight coupling of displacements and integrin concentrations ensures a high level of robustness of the solution process.

5.2. Geometrically non-linear variational formulation

The *in vitro* experiments on the contractility response of cells are commonly performed on elastic membrane, where large stretch is applied, as described in Chapter 3. Hence, in the following variational formulation of the coupled governing equations, large displacements of the *in vitro* tested cells is taken into account and a geometrically non-linear formulation is developed. A detailed representation of the underlying non-linear kinematics concepts can be found in e.g. [164], while a brief overview is given in the following subsections.

5.2.1. Kinematics

In Fig. 5.2, a body is depicted in an undeformed configuration at time $t = 0$, denoted with $\mathcal{B}^0$, and a deformed configuration at time $t \neq 0$, denoted with $\mathcal{B}$. In the following, the initial configuration $\mathcal{B}^0$ is used as a reference configuration in a Total-Lagrangian formulation.

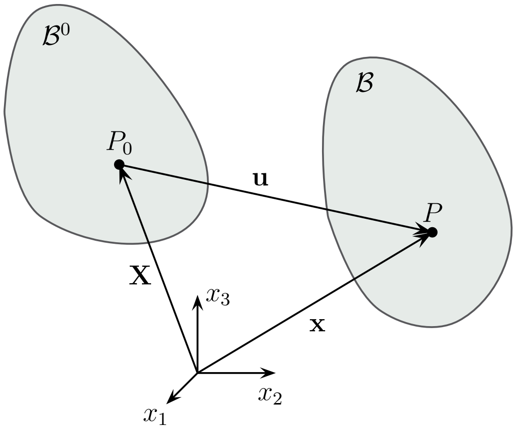

Fig. 5.2: Undeformed reference configuration $\mathcal{B}^0$ and deformed configuration $\mathcal{B}$ of a body. Position of a point P_0 is denoted by $\mathbf{X}$ in the reference configuration while it is denoted by $\mathbf{x}$ in the current configuration.

Material points of the reference configuration $\mathcal{B}^0$ are identified by a location vector $\mathbf{X}$ measured with respect to a stationary reference frame (x_1, x_2, x_3), with the basis vectors

$$\mathbf{e}_i = \frac{\partial \mathbf{X}}{\partial x_i} \qquad i = 1, 2, 3\,. \tag{5.1}$$

Material points of the current configuration $\mathcal{B}$ are identified correspondingly by a location vector $\mathbf{x}$. With the change of the configuration of the body, the displacement state $\mathbf{u}$ and the deformation gradient $\mathbf{F}$ follow as

$$\mathbf{u} = \mathbf{x} - \mathbf{X} \tag{5.2}$$

$$\mathbf{F} = \frac{\partial \mathbf{x}}{\partial \mathbf{X}}\,. \tag{5.3}$$

Using the deformation gradient, Eq. (5.3), the Green-Lagrange strain tensor is defined conventionally as

$$\mathbf{E} = \frac{1}{2}\left(\mathbf{F}^T\mathbf{F} - \mathbf{I}\right) \tag{5.4}$$

$$E_{ij} = \frac{1}{2}\left(\frac{\partial u_i}{\partial X_j} + \frac{\partial u_j}{\partial X_i} + \sum_k \frac{\partial u_k}{\partial X_i}\frac{\partial u_k}{\partial X_j}\right) \qquad i,j,k = 1,2,3\,. \tag{5.5}$$

5.2.2. Statics

The energetic conjugate stress measure to the Green-Lagrange strains are the 2^{nd} Piola-Kirchhoff stresses which are computed using the three-dimensional constitutive relations. A linear relation between stress and strain rates can be established with the assumption of small strains

$$\dot{\mathbf{S}} = \mathbb{C} : \dot{\mathbf{E}} \tag{5.6}$$

$$\dot{S}_{ij} = C_{ijkl}\,\dot{E}_{kl} \tag{5.7}$$

where $\mathbb{C}$ is a fourth order material tensor [164]. The 2^{nd} Piola-Kirchhoff stresses refer to the known reference configuration $\mathcal{B}^0$ without having a physical interpretation. The true stresses of the deformed body are the Cauchy stresses $\boldsymbol{\tau}$ which refer to the unknown current configuration $\mathcal{B}$. They are determined from the 2^{nd} Piola-Kirchhoff stresses by the transform

$$\boldsymbol{\tau} = \frac{\rho}{\rho_0}\,\mathbf{F}\,\mathbf{S}\,\mathbf{F}^T \tag{5.8}$$

where ρ and ρ_0 denote the material density in the current and reference configuration, respectively.

5.2.3. Governing equations

In the following sections, the variational formulation, of the model introduced in Chapter 4, on the basis of the Principle of Virtual Work will be introduced and the corresponding linearised equations are derived for an incremental iterative solution with a staggered and with a monolithic solution approach. The geometry considered in the analysis refers to a square domain representing the cell and the focal adhesion distribution. As explained in Chapter 4, symmetry of the solution domain is considered and therefore only a quarter of the domain is modelled as depicted in Fig. 5.3. The governing equations follow a coordinate representation of a plane state of stress in which the Einstein summation convention is applied and indices take values $\{1, 2\}$.

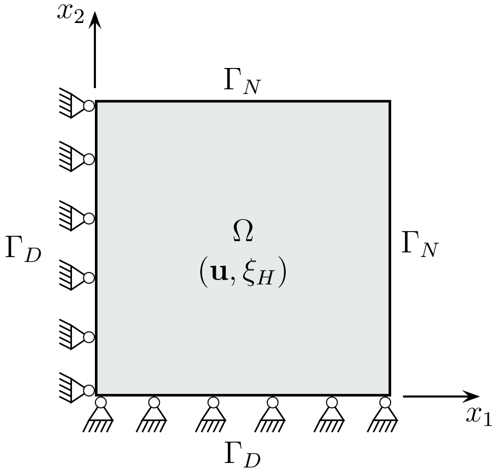

Fig. 5.3: Solution domain Ω with symmetric Dirichlet boundary Γ_D and Neumann boundary Γ_N, solved for the state variables $\mathbf{u}$ and ξ_H.

5.2.4. Staggered solution approach

In the staggered approach, the equations governing the mechanical equilibrium and the focal adhesion growth are considered in separate solution steps. The Total Lagrangian formulation of the virtual work of the equilibrium Eq. (4.32) refers all quantities to the reference configuration $\mathcal{B}^0$:

$$\delta\mathcal{W} \;=\; 0 \;=\; b\int_{\Omega_0} S_{ij} \,:\, \delta E_{ij}\, d\Omega + \int_{\Omega_0} (\xi_H\, \bar{F}_i)\, \delta u_i\, d\Omega \tag{5.9}$$

where the 2^{nd} Piola-Kirchhoff stress $S_{ij} = S^a_{ij} + S^p_{ij}$ represents the sum of active and passive stress in the stress fibre, and Ω_0 represents the domain in the reference configuration.

The equation Eq. (5.9) is non-linear and requires a stepwise incremental solution. A consistent linearisation of the governing equations expresses the *unknown* instant state of a variable $\hat{a}$ at time $(t + \Delta t)$ in terms of its *known* value a of the instant configuration at time t and the *unknown* incremental growth Δa from time t to $t + \Delta t$. Neglecting all higher order non-linear terms the linearised incremental equations follow as:

$$
\begin{aligned}
0 &= \delta\mathcal{W}_{(L\Delta)} + \delta\mathcal{W}_{(N\Delta)} - \delta\mathcal{W}_{(L)} && (5.10)\\
\delta\mathcal{W}_{(L\Delta)} &= b\int_{\Omega_0}\left(C^a_{ijkl}\,\Delta E^L_{kl}\right)\,\delta(\Delta E^L_{ij})\,d\Omega + b\int_{\Omega_0}\left(C^p_{ijkl}\,\Delta E^L_{kl}\right)\,\delta(\Delta E^L_{ij})\,d\Omega \\
&\quad + \int_{\Omega_0}\xi_H\left(\frac{\partial(\Delta\bar{F}_i)}{\partial(\Delta u_j)}\Delta u_j\right)\,\delta(\Delta u_i)\,d\Omega && (5.11)\\
\delta\mathcal{W}_{(N\Delta)} &= b\int_{\Omega_0} S^a_{ij}\,\delta(\Delta E^N_{ij})\,d\Omega + b\int_{\Omega_0} S^p_{ij}\,\delta(\Delta E^N_{ij})\,d\Omega && (5.12)\\
\delta\mathcal{W}_{(L)} &= b\int_{\Omega_0} S^a_{ij}\,\delta(\Delta E^L_{ij})\,d\Omega + b\int_{\Omega_0} S^p_{ij}\,\delta(\Delta E^L_{ij})\,d\Omega \\
&\quad + \int_{\Omega_0}\xi_H\,\bar{F}_i\,\delta(\Delta u_i)\,d\Omega && (5.13)
\end{aligned}
$$

where the subscripts $(L\Delta)$ and $(N\Delta)$ indicate the terms to be linear and non-linear in the displacement increments (Δu), respectively, and subscript (L) denotes quantities which refer to the known instant configuration at time t, representing the equilibrium of the previous step. The superscripts (L) and (N) indicate strain tensor split into linear and non-linear components respectively. The first term of Eq. (5.11) represents the linearisation of the active stress contribution which follows from the evaluation of the *Hill*-type growth model, Eq. (4.11), whereas the second term represents the passive stress contribution corresponding to a linear elastic material behaviour.

Discrete equations of the staggered solution

The domain is discretised with quadrilateral elements using bi-linear *Lagrange* functions to interpolate the unknown displacement increments:

$$
\begin{aligned}
\Delta\mathbf{u} &= \sum_{k=1}^{n} N_k(x_1,x_2)\,\Delta\mathbf{U}_k &&= \mathbf{N}\,\Delta\mathbf{U} && (5.14)\\
\delta(\Delta\mathbf{u}) &= \sum_{k=1}^{n} N_k(x_1,x_2)\,\delta(\Delta\mathbf{U}_k) &&= \mathbf{N}\,\delta(\Delta\mathbf{U}) && (5.15)
\end{aligned}
$$

where N_k represent the bi-linear shape functions assembled in a matrix $\mathbf{N}$ and $\mathbf{U}_k$ the k^{th} unknown nodal degrees of freedom in the plane, assembled in a vector $\mathbf{U}$. Taking the derivatives of Eq. (5.14) and Eq. (5.15) with respect to the global coordinates provides an interpolation rule for the incremental strain coordinates and corresponding variation which are assembled in matrices $\mathbf{B}_L$ and $\mathbf{B}_N$ to account for the linear and non-linear contributions, respectively. A detailed representation of the interpolation matrices can be found in e.g. [164]. Substitution of the discretisation into the governing equations Eq. (5.10) and assembly ($\mathcal{A}_e$) of all elements yields:

$$\mathcal{A}_e\{\mathbf{0} \;=\; \delta(\Delta\mathbf{U})^T\,(\mathbf{K}_L+\mathbf{K}_N)\,\Delta\mathbf{U}-\delta(\Delta\mathbf{U})^T\mathbf{F}_{int}\} \tag{5.16}$$

with the element contributions:

$$\begin{aligned}\mathbf{K}_L \;&=\; b\int_{\Omega_0}\mathbf{B}_L^T\mathbf{C}^p\,\mathbf{B}_L\,d\Omega+b\int_{\Omega_0}\mathbf{B}_L^T\mathbf{C}^a\mathbf{B}_L\,d\Omega \\ &\qquad +\int_{\Omega_0}\xi_H\mathbf{N}^T\frac{\partial\bar{\mathbf{F}}}{\partial\mathbf{U}}\mathbf{N}\,d\Omega \qquad (5.17)\\ \mathbf{K}_N \;&=\; b\int_{\Omega_0}\mathbf{B}_N^T\mathbf{S}^a\,\mathbf{B}_N\,d\Omega+b\int_{\Omega_0}\mathbf{B}_N^T\mathbf{S}^p\,\mathbf{B}_N\,d\Omega \qquad (5.18)\\ \mathbf{F}_{int} \;&=\; b\int_{\Omega_0}\mathbf{B}_L^T\hat{\mathbf{S}}^a\,d\Omega+b\int_{\Omega_0}\mathbf{B}_L^T\hat{\mathbf{S}}^p\,d\Omega+\int_{\Omega_0}\xi_H\mathbf{N}^T\bar{\mathbf{F}}\,d\Omega \qquad (5.19)\end{aligned}$$

where, $\hat{\mathbf{S}}^a$ and $\hat{\mathbf{S}}^p$ are the active and passive stress tensors in Voigt notation and $\bar{\mathbf{F}} = \lambda_s\,\boldsymbol{\Delta}$ denotes the interaction force contribution which results from the bond between focal adhesion and cell, not to be confused with the deformation gradient $\mathbf{F}$, Eq. (5.3), and $\boldsymbol{\Delta}$ corresponds to the stretch, cf eq. (4.22). The last term of Eq. (5.17) contains the linearisation of the interaction force $\bar{\mathbf{F}}$ which is evaluated subject to the condition given in Eq. (4.31), which relates the evolution of stretch and displacement assuming a perfect bond of the integrins and the cell membrane. Using a *first order forward Euler* approach, a numerical approach where the value evaluated at the current time step depends only on the value in the previous time step, to express the unknown stretch and corresponding linearisation renders the last integral term of Eq. (5.17) as:

$$\int_{\Omega_0}\xi_H\mathbf{N}^T\frac{\partial\bar{\mathbf{F}}}{\partial\mathbf{U}}\mathbf{N}\,d\Omega \;=\; \int_{\Omega_0}\xi_H\,\lambda_s\mathbf{N}^T\mathbf{N}\,d\Omega\,. \tag{5.20}$$

Finally, the assembled element contributions result in a linear system of equations representing the governing incremental equations of the mechanical equilibrium:

$$\Big[\mathbf{K}_T\Big]\,\Big[\Delta\mathbf{U}\Big] \;=\; \Big[\mathbf{R}\Big] \tag{5.21}$$

where $\mathbf{K}_T$ is the tangent stiffness matrix assembled from the linear and non-linear element stiffness contributions and $\mathbf{R}$ is the residual at the beginning of the solution step for the unknown instant configuration at time $t + \Delta t$. At the end of each time step the known displacement field is used to evaluate the stretch which allows the computation of the integrin ratio Eq. (4.23) and thereby to update the higher affinity integrin concentration, cf. Eq. (4.27).

5.2.5. Monolithic solution approach

The monolithic solution approach solves the mechanical equilibrium and the focal adhesion growth in a common solution step. In addition to the chemo-mechanical equilibrium Eq. (4.32), the conservation of the total number of integrins, Eq. (4.25), must be satisfied by the unknown high affinity integrins, which leads to a coupling of mechanical equilibrium and focal adhesion growth. The virtual work expression Eq. (5.9) is extended by a corresponding term from Eq. (4.27):

$$\begin{aligned} \delta\mathcal{W} \;=\; 0 \;=\; & b\int_{\Omega_0} S_{ij} \,:\, \delta E_{ij}\, d\Omega + \int_{\Omega_0} (\xi_H\, \bar{F}_i)\, \delta u_i \, d\Omega \\ & + \int_{\Omega_0} \xi_H \, \delta\xi_H \, d\Omega - \int_{\Omega_0} \xi_0 \frac{\alpha}{1+\alpha}\, \delta\xi_H \, d\Omega\,. \end{aligned} \tag{5.22}$$

The consistent linearisation of the non-linear equilibrium Eq. (5.22) follows the principles introduced in sub-section. 5.2.4 and leads to the following contributions:

$$0 \;=\; \delta\mathcal{W}^{(u)}_{(L\Delta)} + \delta\mathcal{W}^{(u)}_{(N\Delta)} - \delta\mathcal{W}^{(u)}_{(L)} + \delta\mathcal{W}^{(\xi)}_{(L\Delta)} - \delta\mathcal{W}^{(\xi)}_{(L)} \tag{5.23}$$

$$\begin{aligned} \delta\mathcal{W}^{(u)}_{(L\Delta)} \;=\; & b\int_{\Omega_0} \left(C^a_{ijkl}\, \Delta E^L_{kl}\right)\, \delta(\Delta E^L_{ij})\, d\Omega + b\int_{\Omega_0} \left(C^p_{ijkl}\, \Delta E^L_{kl}\right)\, \delta(\Delta E^L_{ij})\, d\Omega \\ & + \int_{\Omega_0} \xi_H \left(\frac{\partial(\Delta\bar{F}_i)}{\partial(\Delta u_j)} \Delta u_j\right)\, \delta(\Delta u_i)\, d\Omega \end{aligned} \tag{5.24}$$

$$\delta\mathcal{W}^{(u)}_{(N\Delta)} \;=\; b\int_{\Omega_0} S^a_{ij}\, \delta(\Delta E^N_{ij})\, d\Omega + b\int_{\Omega_0} S^p_{ij}\, \delta(\Delta E^N_{ij})\, d\Omega \tag{5.25}$$

$$\begin{aligned}\delta\mathcal{W}^{(u)}_{(L)} &= b\int_{\Omega_0} S^a_{ij}\,\delta(\Delta E^L_{ij})\,d\Omega + b\int_{\Omega_0} S^p_{ij}\,\delta(\Delta E^L_{ij})\,d\Omega \\ &\qquad + \int_{\Omega_0} \xi_H\,\bar{F}_i\,\delta(\Delta u_i)\,d\Omega \qquad (5.26)\end{aligned}$$

$$\delta\mathcal{W}^{(\xi)}_{(L\Delta)} = \int_{\Omega_0} \Delta\xi_H\,\delta(\Delta\xi_H)\,d\Omega \qquad (5.27)$$

$$\delta\mathcal{W}^{(\xi)}_{(L)} = \int_{\Omega_0} \xi_0\,\frac{\alpha}{1+\alpha}\,\delta(\Delta\xi_H)\,d\Omega - \int_{\Omega_0} \xi_H\,\delta(\Delta\xi_H)\,d\Omega \qquad (5.28)$$

where the superscripts (u) and (ξ) indicate the origin of the corresponding work contribution.

Discrete equations of the monolithic solution

The unknown high affinity integrins of the governing equations are interpolated applying the same discretisation that is used for the unknown displacement field

$$\xi_H = \sum_{j=1}^{n} N_j(\Delta\xi_H)_j = \hat{\mathbf{N}}\,\Delta\boldsymbol{\xi}_H \qquad (5.29)$$

$$\delta\xi_H = \sum_{j=1}^{n} N_j\,\delta(\Delta\xi_H)_j = \hat{\mathbf{N}}\,\delta(\Delta\boldsymbol{\xi}_H) \qquad (5.30)$$

where $\hat{\mathbf{N}}$ assembles the bi-linear Lagrange shape functions in a vector and $\Delta\boldsymbol{\xi}_H$ represents scalar nodal degrees of freedom. Substitution of the discretisation into the governing equations Eq. (5.23) and assembly $(\mathcal{A}_e)$ of all elements yields:

$$\mathcal{A}_e\{\mathbf{0} = \delta(\Delta\mathbf{U})^T\,(\mathbf{K}^{uu}_L + \mathbf{K}^{uu}_N)\,\Delta\mathbf{U} + \delta(\Delta\mathbf{U})^T\mathbf{K}^{u\xi}\,\Delta\boldsymbol{\xi} \qquad (5.31)$$

$$+\delta(\Delta\boldsymbol{\xi})^T\mathbf{K}^{\xi\xi}\,\Delta\boldsymbol{\xi} - \delta(\Delta\mathbf{U})^T\mathbf{F}^u_{int} - \delta(\Delta\boldsymbol{\xi})^T\mathbf{F}^{\xi}_{int}\} \qquad (5.32)$$

with the element contributions:

$$\begin{aligned}
\mathbf{K}_L^{uu} &= b\int_{\Omega_0} \mathbf{B}_L^T \mathbf{C}^p \, \mathbf{B}_L \, d\Omega + b\int_{\Omega_0} \mathbf{B}_L^T \mathbf{C}^a \mathbf{B}_L \, d\Omega \\
&\qquad\qquad\qquad\qquad + \int_{\Omega_0} \xi_H \, \lambda_s \, \mathbf{N}^T \mathbf{N} \, d\Omega && (5.33) \\
\mathbf{K}_N^{uu} &= b\int_{\Omega_0} \mathbf{B}_N^T \mathbf{S}^a \, \mathbf{B}_N \, d\Omega + b\int_{\Omega_0} \mathbf{B}_N^T \mathbf{S}^p \, \mathbf{B}_N \, d\Omega && (5.34) \\
\mathbf{K}^{u\xi} &= \int_{\Omega_0} \mathbf{N}^T \hat{\mathbf{F}} \, \hat{\mathbf{N}} \, d\Omega && (5.35) \\
\mathbf{K}^{\xi\xi} &= \int_{\Omega_0} \hat{\mathbf{N}}^T \hat{\mathbf{N}} \, d\Omega && (5.36) \\
\mathbf{F}_{int}^{u} &= b\int_{\Omega_0} \mathbf{B}_L^T \hat{\mathbf{S}}^a \, d\Omega + b\int_{\Omega_0} \mathbf{B}_L^T \hat{\mathbf{S}}^p \, d\Omega + \int_{\Omega_0} \xi_H \mathbf{N}^T \bar{\mathbf{F}} \, d\Omega && (5.37) \\
\mathbf{F}_{int}^{\xi} &= \int_{\Omega_0} \xi_0 \frac{\alpha}{1+\alpha} \hat{\mathbf{N}}^T \, d\Omega - \int_{\Omega_0} \hat{\mathbf{N}}^T \hat{\mathbf{N}} \, \boldsymbol{\xi}_H \, d\Omega && (5.38)
\end{aligned}$$

in which the $(2N \times N)$-matrix $\mathbf{K}^{u\xi}$ is a coupling matrix relating the unknown high affinity integrins to the unknown displacements of the chemo-mechanical problem. Its transpose $\mathbf{K}^{\xi u} = \mathbf{0}$, leads to a non-symmetric system of equations. The system matrices assembled from Eq. (5.33) to Eq. (5.36) and the corresponding system vectors assembled from Eq. (5.37) and Eq. (5.38) provide the linearised system of equations of the monolithic solution approach:

$$\begin{bmatrix} \mathbf{K}^{uu} & \mathbf{K}^{u\xi} \\ \mathbf{0} & \mathbf{K}^{\xi\xi} \end{bmatrix} \begin{bmatrix} \Delta\mathbf{U} \\ \Delta\boldsymbol{\xi} \end{bmatrix} = \begin{bmatrix} \mathbf{R}^u \\ \mathbf{R}^\xi \end{bmatrix} \qquad (5.39)$$

where the incremental displacement field and the incremental high affinity integrins are solved in the same step. The established monolithic coupling is based on a one-way dependence of the high affinity integrins on the stretch of the focal adhesion induced bond.

5.2.6. Feedback loop mechanism

The feedback loop mechanism, described in Section 4.4 relates the calcium growth to the stress fibre formation in the cell and requires an independent solution of the reaction-diffusion equation Eq. (4.35) with the variational representation:

$$\begin{aligned}\int_\Omega \dot{\bar{S}}\,(\delta\bar{S})\,d\Omega &= -D\int_\Omega \frac{\partial\bar{S}}{\partial x_i}\frac{\partial(\delta\bar{S})}{\partial x_i}\,d\Omega + R \\ \text{with} \quad R &= -k_d\int_\Omega \bar{S}\,(\delta\bar{S})\,d\Omega - \dot{\varepsilon}\int_\Omega \bar{S}\,(\delta\bar{S})\,d\Omega + \frac{\alpha_c}{b}\,max(0,\dot{\xi}_H)\int_\Omega \delta\bar{S}\,d\Omega\end{aligned} \tag{5.40}$$

in which the variation of the IP3 concentration $(\delta\bar{S})$ is chosen as appropriate test function, and $D = (m_s\,k\,T)$ is the diffusion coefficient while R denotes the reaction terms. The analysis domain considers *no-flux* conditions along the Neumann boundary Γ_N and an initial domain IP3 concentration s_0 including the Dirichlet boundary Γ_D where s_0 is the reference IP3 concentration, cf Table. 4.1:

$$-D\frac{\partial\bar{S}}{\partial x_i}\,n_i = 0 \quad \forall\, x_i \in \Gamma_N \tag{5.41}$$

$$\bar{S} = s_0 \quad \forall\, x_i \in \Omega \supset \Gamma_D\,. \tag{5.42}$$

The change of the IP3 concentration with time on the left-hand side of Eq. (5.40) is resolved in terms of a first order forward Euler approach:

$$\dot{\bar{S}} = \frac{\bar{S}(t+\Delta t)-\bar{S}(t)}{\Delta t} := \frac{\bar{S}-\bar{S}^t}{\Delta t} \tag{5.43}$$

in which Δt is the time step increment and $\bar{S}^t$ is the known primal field variable of the previous time step.

The spatial discretisation follows the bi-linear approach introduced in the sub-section 5.2.4 using the interpolation approach Eq. (5.29) and Eq. (5.30) with the shape functions $\hat{\mathbf{N}}$ and their corresponding spatial derivatives $\hat{\mathbf{N}}_{,x}$ resulting in the governing algebraic equations:

$$\mathcal{A}_e\{\,\mathbf{0} = \delta\bar{\mathbf{S}}^T\,(\mathbf{M}_{\bar{S}}+\mathbf{K}_{\bar{S}})\,\bar{\mathbf{S}} + \delta\bar{\mathbf{S}}^T\,(\mathbf{F}_t+\mathbf{F}_{\xi_H})\,\} \tag{5.44}$$

with the element contributions:

$$\mathbf{M}_{\bar{S}} = \int_{\Omega} \left(\frac{1}{\Delta t} + k_d + \dot{\varepsilon} \right) \hat{\mathbf{N}}\, \hat{\mathbf{N}}^T \, d\Omega \tag{5.45}$$

$$\mathbf{K}_{\bar{S}} = \int_{\Omega} D\, \hat{\mathbf{N}}_{,x}\, \hat{\mathbf{N}}_{,x}^T \, d\Omega \tag{5.46}$$

$$\mathbf{F}_t = \int_{\Omega} \frac{\bar{S}^t}{\Delta t} \hat{\mathbf{N}} \, d\Omega \tag{5.47}$$

$$\mathbf{F}_{\xi_H} = \int_{\Omega} \left(\frac{\alpha_c}{b}\, max(0, \dot{\xi}_H) \right) \hat{\mathbf{N}} \, d\Omega \,. \tag{5.48}$$

The governing linear system of equations is solved in each time step to provide the current IP3 concentration $\bar{\mathbf{S}}$ which is used to predict the calcium production that initiates the focal adhesion growth. The calcium growth, Eq. (4.36), is solved by an embedded Runge-Kutta scheme, a single-step approach which approximates the solution considering two Runge-Kutta estimates of different order to allow for a control of the truncation error with adaptive step-size [165].

5.3. Algorithmic aspects

The governing algebraic equations of sections 5.2.4, and 5.2.5 reveal the essential differences between the staggered and the monolithic approaches, and how the coupling of the chemo-mechanical equations is established. The different schemes have direct effect on the structure and algebraic properties of the governing system of equations, and thus on the single solution steps including stability and robustness of the solution. It is to be noted here that monolithic scheme solves only the mechanical equilibrium and focal adhesion growth equations in a single step, while the reaction-diffusion equation for IP3 integrins is solved separately.

The algorithmic structure of the monolithic and staggered solution schemes is depicted in Algorithms 1 and 2, respectively. Both schemes start with entering a time step loop and the computation of the stress fibre concentration η, used to update the isometric stress σ_0 and thus the active stress σ^a in the mechanical equilibrium. The stress fibre concentration η, which is solved by an embedded Runge-Kutta-method [165], requires an update of the calcium concentration in the cell and thus the evaluation of the current IP3 concentration, Eq. (4.35), establishing the feedback loop between the focal adhesion formation and the stress fibre generation.

```
Data: model geometry and material parameter values as provided in Table. 4.1 [12]
Result: nodal displacements $\mathbf{u}$ and high affinity integrin concentrations $\boldsymbol{\xi}_H$ and
        corresponding increments at time $t = t_{end}$, assembled in a common
        solution vector $\mathbf{V} := [\mathbf{U}; \boldsymbol{\xi}_H]$ and $\Delta\mathbf{V} := [\Delta\mathbf{U}; \Delta\boldsymbol{\xi}_H]$, respectively.

% model setup and initialization
setupAnalysisModel();
$t = 0$;

% incremental time step loop
while $t < t_{end}$ do
    % mechanosensitive feedback update: evaluate IP3 concentration, Eq. (4.35)
    $\bar{S}$ = IP3Production($m_s, k, T, \alpha_c, k_d, b, \dot{\xi}_H, \dot{\varepsilon}(\Phi)$);

    % evaluate calcium concentration using an embedded
    % Runge-Kutta scheme, Eq. (4.36)
    $C$ = calciumConcentration($\bar{S}, \bar{S}_0, \lambda_f, \lambda_b$);

    % evaluate stress fibre concentration using an embedded
    % Runge-Kutta scheme, Eq. (4.1)
    $\eta$ = stressfibreConcentration($\lambda_f, \lambda_b, C, \kappa, \phi$);

    % Newton-Raphson iteration until stopping criteria is satisfied
    while $\delta^i > \varepsilon_r \, \delta^t$ do
        % solution of the governing system of equations Eq. (5.39), quantities refer
          to time $t + \Delta t$
        $\mathbf{K}^{i-1} \, \Delta\mathbf{V}^i = \mathbf{F}^{i-1}_{ext} - \mathbf{F}^{i-1}_{int}$;

        % solution update in iteration $i$ of time step $t + \Delta t$
        $\mathbf{V}^i = \mathbf{V}^{i-1}$ - $\Delta\mathbf{V}^i$;

        % update of the convergence parameters
        $\delta^i$ = max( abs($\mathbf{U}^i$ - $\mathbf{U}^{i-1}$) );
        $\delta^t$ = max( abs($\mathbf{U}^i$ - $\mathbf{U}^t$) );

        % increment iteration step
        $i = i + 1$;
    end

    % increment time step
    $t = t + \Delta t$;
end
```

Algorithm 1: Monolithic solution scheme for the analysis of the chemo-mechanical cell response.

```
Data: model geometry and material parameter values as provided in Table. 4.1 [12]
Result: nodal displacements $\mathbf{u}$ and high affinity integrin concentrations $\boldsymbol{\xi}_H$ and
        corresponding increments at time $t = t_{end}$.

% model setup and initialization
setupAnalysisModel();
$t = 0$;

% incremental time step loop
while $t < t_{end}$ do
    % mechanosensitive feedback update: evaluate IP3 concentration, Eq. (4.35)
    $\bar{S} = \mathrm{IP3Production}(m_s, k, T, \alpha_c, k_d, b, \dot{\xi}_H, \dot{\varepsilon}(\Phi))$;

    % evaluate calcium concentration using an embedded
    % Runge-Kutta method, Eq. (4.36)
    $C = \mathrm{calciumConcentration}(\bar{S}, \bar{S}_0, \lambda_f, \lambda_b)$;

    % evaluate stress fibre concentration using an embedded
    % Runge-Kutta method, Eq. (4.1)
    $\eta = \mathrm{stressfibreConcentration}(\lambda_f, \lambda_b, C, \kappa, \phi)$;

    % Newton-Raphson iteration until stopping criteria is satisfied
    while $\delta^i > \varepsilon_r \, \delta^t$ do
        % solution of the governing system of equations Eq. (5.21), quantities refer
          to time $t + \Delta t$
        $\mathbf{K}^{i-1} \, \Delta\mathbf{U}^i = \mathbf{F}^{i-1}_{ext} - \mathbf{F}^{i-1}_{int}$;

        % solution update in iteration $i$ of time step $t + \Delta t$
        $\mathbf{U}^i = \mathbf{U}^{i-1}$ - $\Delta\mathbf{U}^i$;

        % update of the convergence parameters
        $\delta^i = \max($ abs($\mathbf{U}^i$ - $\mathbf{U}^{i-1}$) );
        $\delta^t = \max($ abs($\mathbf{U}^i$ - $\mathbf{U}^t$) );

        % increment iteration step
        $i = i + 1$;
    end
    % update high affinity integrins using equations Eq. (4.24) and Eq. (4.27)
    $\xi_H = f(\xi_0, \Delta(\mathbf{U}))$

    % increment time step
    $t = t + \Delta t$;
end
```

Algorithm 2: Staggered solution scheme for the analysis of the chemo-mechanical cell response.

The monolithic scheme solves the unknown displacement field and high affinity integrins together using an incremental iterative Newton-Raphson method. In each iteration step, the tangent matrix and inner forces are updated with the total displacements to account for the non-linear cell deformation. In contrast, the staggered scheme solves only for the unknown displacement field within the Newton-Raphson iteration using the high affinity integrin concentrations of the previous time step. The integrins of the current step are updated in a follower step on basis of the current displacements.

Both algorithms use a convergence criteria which is exclusively based on the computed total displacements which is a natural choice for the staggered scheme but also a reasonable choice for the monolithic scheme since the high affinity integrins are directly dependent on the stretch and therefore dependent on the displacement field. An error constant ε_r of order 10^{-3} appeared sufficient in all computations to ensure robustness and reliability of the non-linear analysis.

5.4. Numerical Experiments

In this section, numerical experiments are performed to study the solution properties of the staggered and monolithic coupling approaches. Performance aspects for the different solution methods with respect to stability and numerical reliability are considered. To this end, the model is refined in space and time and tested for different levels of refinement. Next, the robustness of the two solution methods for different model configurations considering variation of dominant model parameters is studied. Finally the problem of stress fibre reorientation is considered to study the behaviour of solution schemes.

5.4.1. Convergence properties

The analysis domain subjected to study is depicted in Fig. 5.3 with the model properties provided in Table. 4.1. In the numerical examples presented in this chapter, this choice of parameters are denoted as *base configuration*. Symmetry boundary conditions were applied along the left and lower boundary and zero traction boundary conditions were applied along the right and upper domain boundary. The model is loaded by an initial IP3 concentration s_0 which triggers the growth of the feedback loop coupled with active stress and focal adhesion.

The focal adhesion growth is expected to form towards the boundary of the cell. Accordingly, the initial finite element mesh was refined adaptively towards the domain bound-

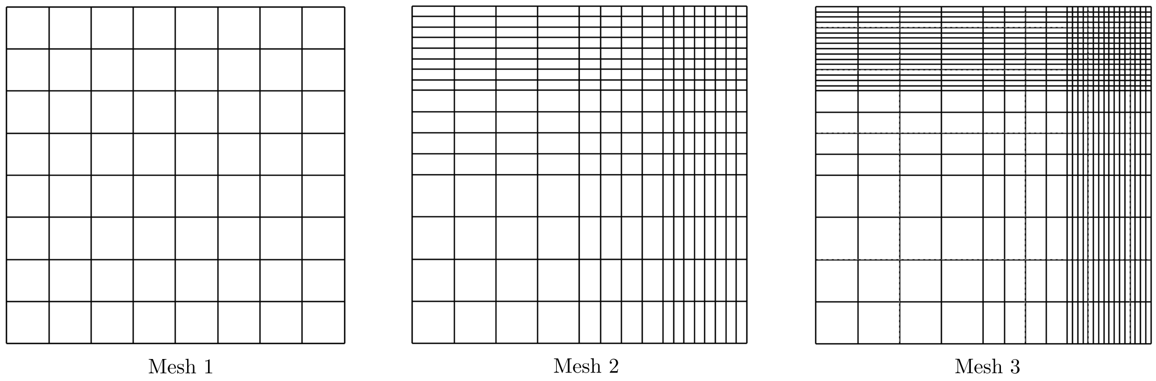

Fig. 5.4: Finite element meshes with 64 elements (mesh 1), 256 elements (mesh 2) and 576 elements (mesh 3).

ary and three different meshes were considered, cf. Fig. 5.4. It is noted that the same discretisation was used for both sub-models, the elasticity problem and the focal adhesion growth problem. The total time span of the simulation, needed to account for a steady-state solution, varies for the different model parameters between 200s and 4000s. The time step size was chosen in the interval $[0.5s, 4.0s]$.

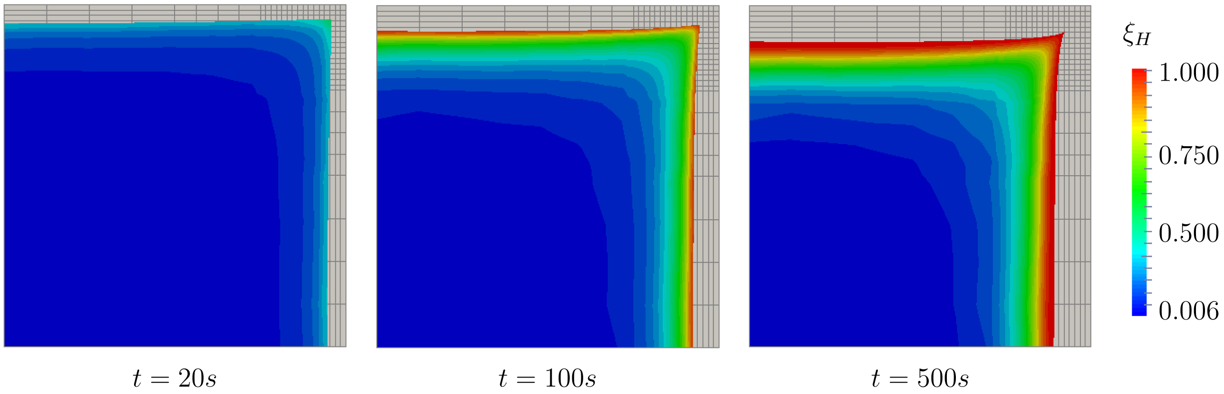

$t = 20s$ $t = 100s$ $t = 500s$

Fig. 5.5: Focal adhesion growth on the deformed cell at different time steps (scale factor = 14), superimposed on reference mesh. Focal adhesion concentration increases along the boundary with time.

The expected focal adhesion growth is evident from the results shown in Fig. 5.5. It represents the temporal evolution of the focal adhesion formation on the deformed cell at different time steps of the parameter base configuration.

The stress fibre growth for the base configuration is depicted in Fig. 5.6, indicating convergence for both solution schemes for chosen time step $\Delta t = 0.5\,s$. The refined mesh (mesh 2) shows virtually identical results for the staggered and monolithic solution methods. Even for the unrefined mesh (mesh 1), the results of the two methods have a relative difference of less than 3%. The good match of the staggered and monolithic solution scheme was observed throughout all computations which led to the same steady-state solution, irrespective of the value of the chosen time step.

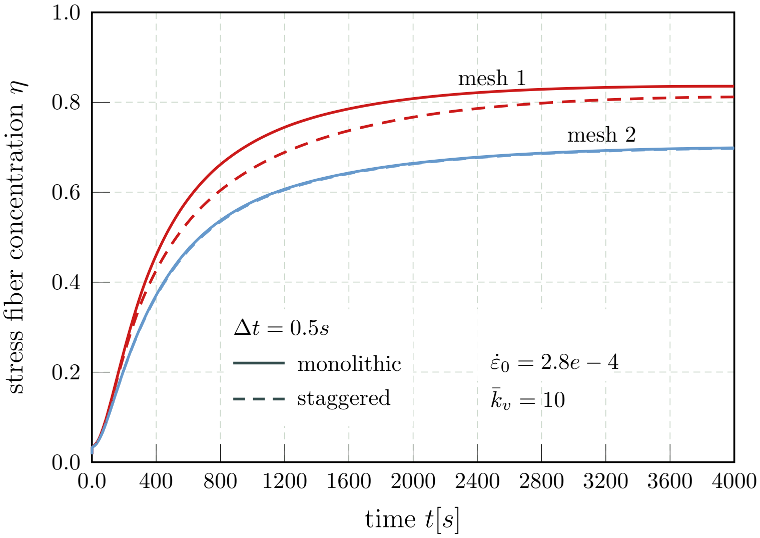

Fig. 5.6: Mesh refinement study for stress fibre growth - base configuration. Monolithic and staggered solutions converge to each other with mesh refinement.

The need for mesh refinement is evident with the results depicted in Fig. 5.6. A linear convergence rate for stress fibre concentration η was observed for all problems, showing a model error of $\approx 2\%$ for the finest discretisation using corresponding estimates for the exact steady state solution based on a Richardson extrapolation [166]. The convergence of the stress fibre concentration at the mid-point of the domain boundary is given in Fig. 5.7.

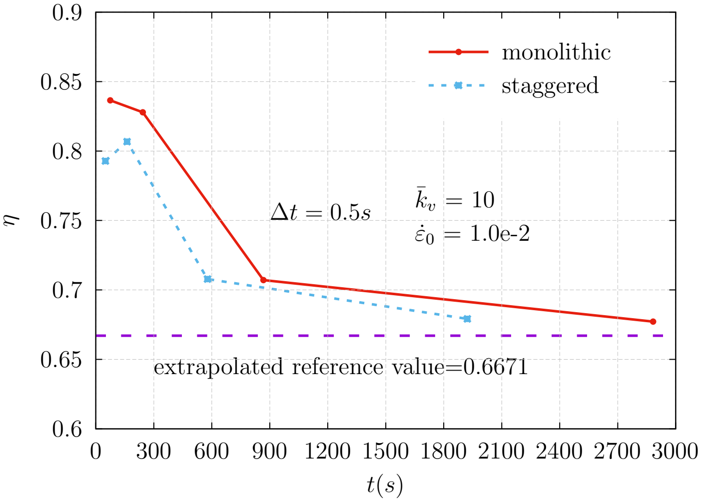

Fig. 5.7: Convergence of the stress fibre concentration with mesh refinement. The solution for the finest mesh is close to the extrapolated value.

In Fig. 5.8(a), the stress fibre growth is shown for a modified Hill constant $\bar{k}_v$, reduced from $\bar{k}_v = 10$ to $\bar{k}_v = 1$, with the effect that the steady-state solution is obtained already after one-third of the simulation time of the base configuration, cf. Fig. 5.6. An increase of the time step size from $0.5s$ to $2s$ has no influence with respect to convergence behaviour and the value of the steady-state solution.

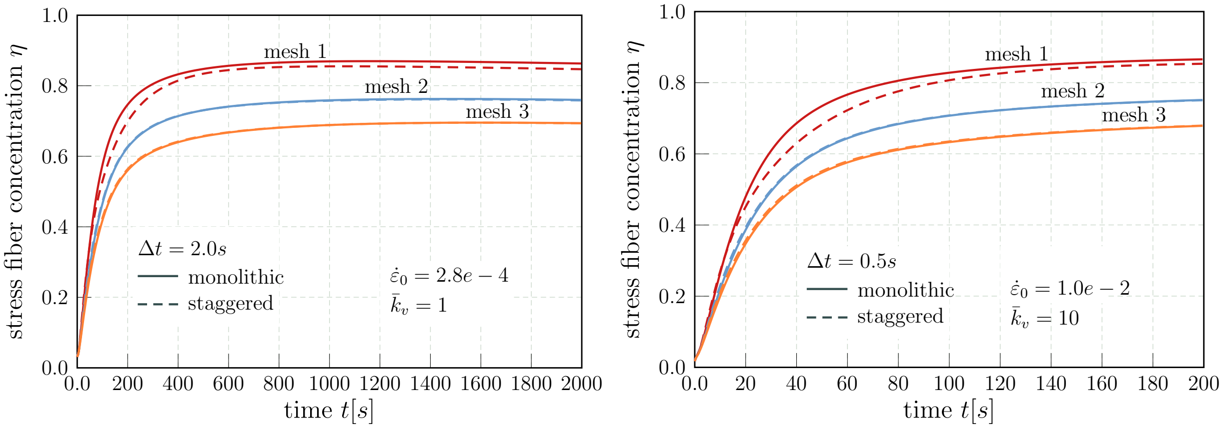

(a) modified Hill coefficient $\bar{k}_v$

(b) modified strain rate $\dot{\varepsilon}_0$

Fig. 5.8: Comparison of staggered vs. monolithic schemes for different mesh refinements. By changing the values of model parameters $\bar{k}_v$ and $\dot{\varepsilon}_0$, the maximum time step that could be used with the staggered solution for it to converge to monolithic solution upon mesh refinement, limits to (a) 2s and (b) 0.5s.

The increase of the strain rate from $\dot{\varepsilon}_0 = 2.8e-4$ to $\dot{\varepsilon}_0 = 0.01$ accelerates the growth of the stress fibre concentration even more as shown in Fig. 5.8(b). Both modifications of the base configuration lead to an increased stress fibre concentration of about 8%, which indicates a reduction of the stress fibre dissociation due to an increased active stress level, and thereby an increased activation rate. The difference in the rate of stress fibre formation can be correlated to the observation made in Chapter 3, where osteoblast cells were found to respond slower compared to fibroblast cells. Thus, by changing the parameters, the model can simulate behaviour of different cell types.

Next,the influence of the time step size on robustness, reliability and numerical effort of the analysis is considered. Time steps Δt of $0.5s, 1s, 2s$ and $4s$ were taken and a robust solution was obtained for the base configuration. Even for a time step of $\Delta t = 6s$, convergence was achieved with both schemes but only for the base configuration whereas in all other parameter configurations only the monolithic scheme succeeded. The models with modified Hill-coefficient and strain rate, depicted in Fig. 5.9(a) and Fig. 5.9(b), respectively, showed a different behaviour. For a Hill-coefficient $\bar{k}_v = 1.0$ the staggered scheme failed to compute a steady-state solution for $\Delta t = 4s$. The failure occurred during the Newton-Raphson iteration which was used for the solution of the non-linear equilibrium equations. In the case of increased strain rate to $\dot{\varepsilon}_0 = 0.01$, the staggered scheme failed already for $\Delta t = 2s$, and oscillations were found even for $\Delta t = 1s$.

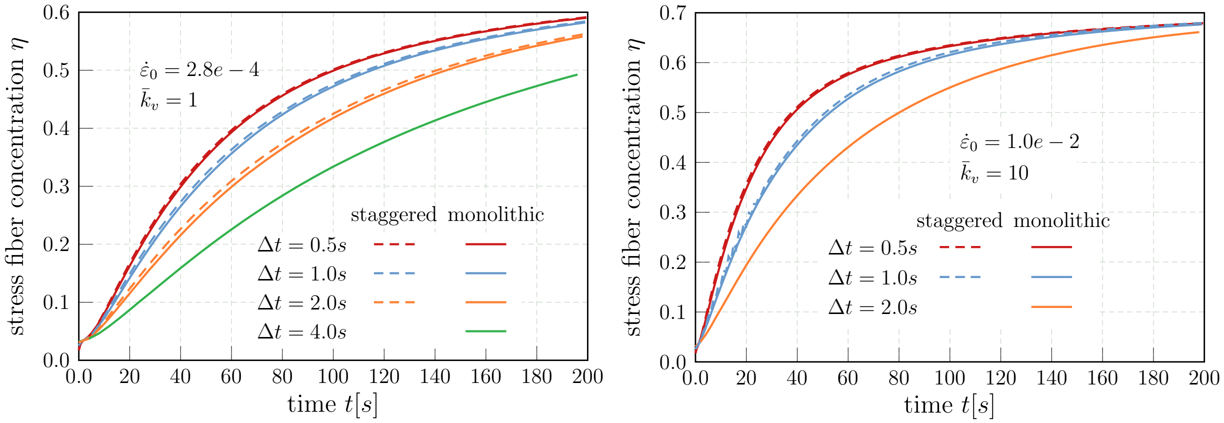

(a) modified Hill coefficient $\bar{k}_v$ (b) modified strain rate $\dot{\varepsilon}_0$

Fig. 5.9: Comparison of staggered vs. monolithic schemes for different time step increments, finest mesh. Staggered scheme does not converge in case when the time step is increased to (a) 4s while oscillations are seen even at 1s in case (b).

In sum, the robustness of the staggered scheme was weaker than that of the monolithic scheme and showed some discretisation sensitivity in terms of an oscillatory behaviour already at a time step size $\Delta t = 1s$, cf. Fig. 5.9(b), and aggravated for larger time step sizes as depicted in Fig. 5.10. This behaviour was not observed in any computation with the monolithic scheme, irrespective of the chosen time step size and mesh density.

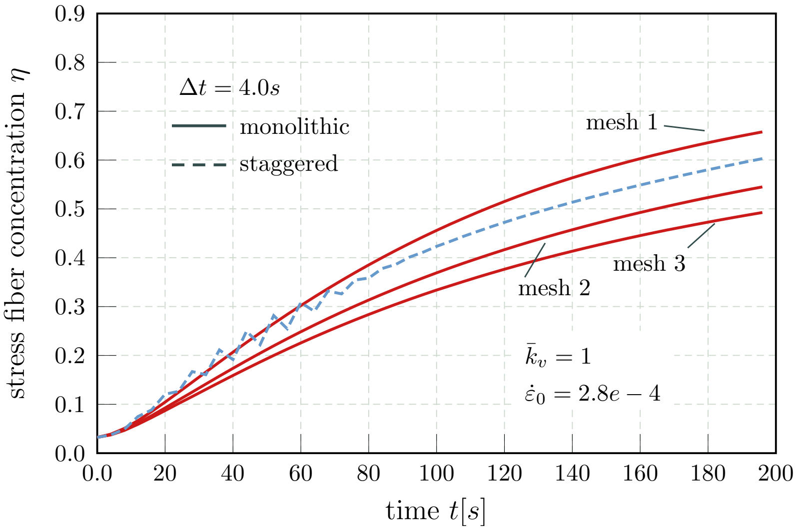

Fig. 5.10: Oscillatory behaviour of the staggered solution scheme. Oscillations are found with staggered solution even with the coarsest mesh.

The higher robustness of the monolithic scheme compared to the staggered scheme is clearly visible from the comparison of Fig. 5.11 which shows virtually no difference in the focal adhesion growth for the staggered solution scheme using a time step of $\Delta t = 0.5s$ and for the monolithic approach with a time step $\Delta t = 4s$.

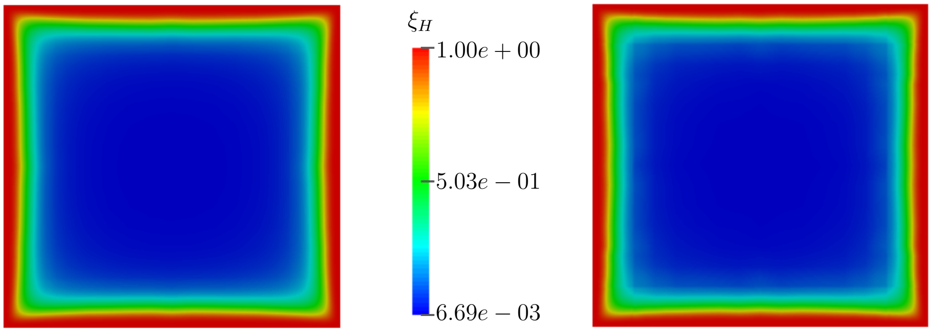

(a) staggered solution, $\Delta t = 0.5s$

(b) monolithic solution, $\Delta t = 4.0s$

Fig. 5.11: Focal adhesion growth for staggered and monolithic methods at $t = 2000s$. No difference is found between the solution obtained by (a) staggered scheme with a time step of 0.5s and (b) monolithic scheme with a time step of 4s.

5.4.2. Cyclic loading

In this section, the staggered and monolithic solution schemes will be tested for the cyclic loading test as described in Sec. 4.5. The solution of the numerical problem shows that during the unloading phase, the stress fibre concentration along the direction away from the loading direction is higher than that of the loading direction. This behaviour is visible from Fig. 5.12 where the $\phi = 90°$ curves cut the $\phi = 0°$ curves at the level of $\eta \approx 0.2$ which was simulated by both solution schemes but at different conditions. In Fig. 5.12, the stress fibre concentration for the steady state response is depicted after $1500s$ in the direction of loading ($\phi = 0°$) and perpendicular to it ($\phi = 90°$). The chosen time steps of $\Delta t = 4s$ for the monolithic scheme and $\Delta t = 1s$ for the staggered scheme reveal differences in amplitude and phase. The large time step size of the monolithic scheme exceeds the core length ($d = 3s$) of the trapezoidal loading function which leads to a constant phase shift. For smaller time steps $\Delta t \leq 2s$ the response curves are congruent.

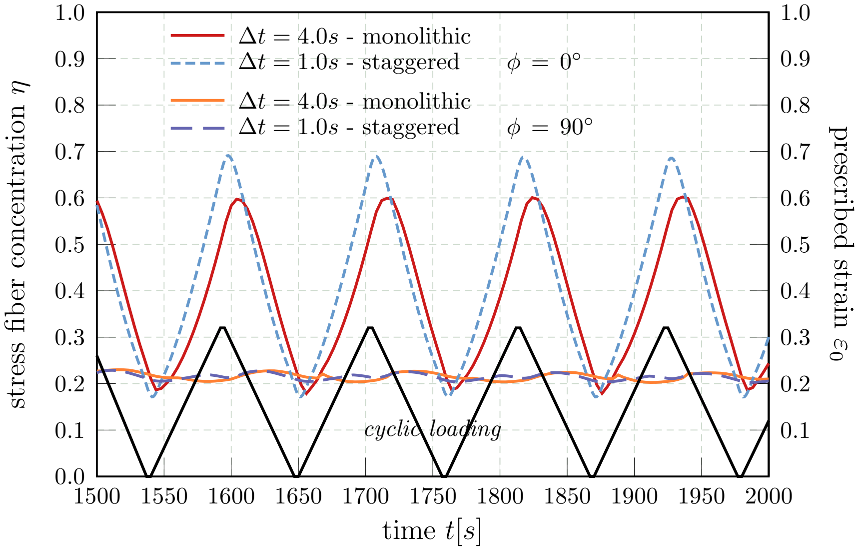

Fig. 5.12: Cyclic loading response with cyclic load function (black solid line), with an amplitude of 0.32, applied along $\phi = 0°$. At the unloaded position, the concentration of stress fibre is lower along the loading direction than its orthogonal direction. The phase shift between staggered and monolithic solutions comes due to the higher time step used.

It can be observed from the circular histograms, Fig. 5.13, that both staggered and monolithic solvers show similar behaviour qualitatively even though the time step used are $1s$ and $4s$ respectively. The computation of the stress fibre concentration at each angle and time step is computationally intensive but can be eased by using higher time step increments as is possible with the monolithic solver.

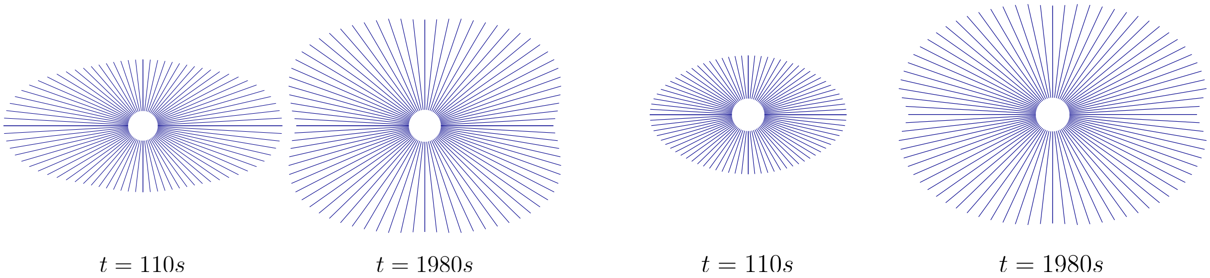

(a) monolithic, $\Delta t = 4s$ (b) staggered, $\Delta t = 1s$

Fig. 5.13: Circular histograms – qualitative comparison of stress fibre growth subjected to cyclic loading along the horizontal direction ($\longleftrightarrow$) show similar behaviour even with different time steps used.

5.4.3. Performance aspects

It is worth noting that the system of equations of the monolithic scheme, Eq. (5.39), has a factor 1.5 more degrees of freedom than the system of equations of the staggered scheme, Eq. (5.21), which is solved in two independent steps considering matrices of dimensions $2N$ and N. Furthermore, the monolithic scheme cannot exploit symmetry properties during the solution process. As a consequence of the different scales involved in the solution of the mechanical response and the focal adhesion concentration, the system matrices are ill-conditioned. Despite a pre-conditioning prior to the solution, a severe numerical sensitivity remains which is reflected in the large number of iterations needed by the Newton-Raphson method to obtain equilibrium in each step, cf. Fig. 5.14. Direct solver was used for both methods to account for sufficient stability. The higher numerical effort needed to factorize the non-symmetric system matrix of the monolithic scheme compared to the smaller and symmetric system matrix of the staggered scheme was easily compensated by the significantly larger time step that could be used in the monolithic scheme. Regarding the numerical complexity of the two solution schemes, the monolithic method saves a factor > 3 which pays off for the considered time spans. Thus, in all the computations tested with temporal and spatial discretisations, monolithic scheme exhibited to be more stable at a slightly fewer number of iterations.

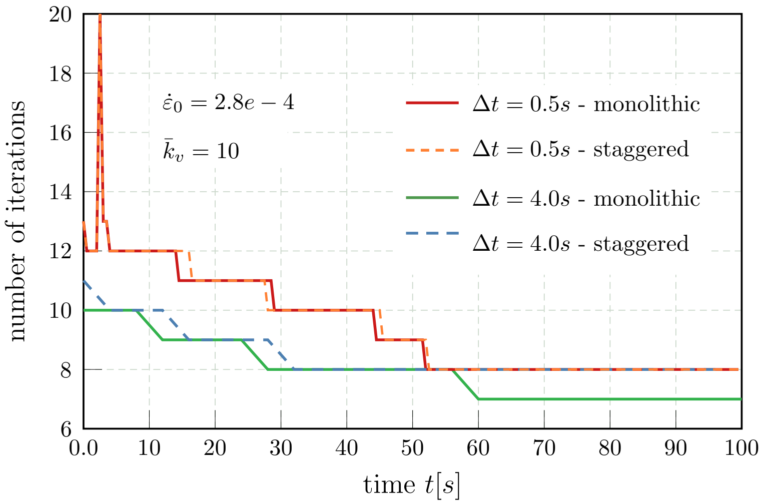

Fig. 5.14: Total number of iterations per time step.

5.5. Summary

In this chapter, different coupling schemes, used for solving the bio-chemo-mechanical model introduced in Chapter 4 have been studied. Variationally consistent continuum formulations coupling the different physics in terms of monolithic and staggered numerical solution schemes have been derived. The difference in the way the governing equations were coupled limited the value of the time step that could be used for staggered scheme, while, the value of the time step used did not have a significant effect on the monolithic scheme. The algorithmic description of the two solution procedures have been provided as well. The variational formulation of the reaction-diffusion model for the feedback loop mechanism has been developed as well. The two derived solution schemes were compared by studying the growth of stress fibre concentration in the cell over time and the numerical performances of these two methods were compared. The space and time refinement showed that staggered coupling scheme failed to provide a steady-state solution with increase in time-step size and showed a distinct mesh sensitivity which was observed already at smaller time steps. The stress fibre reorientation problem was studied for the effect of different time step sizes. It was observed that the qualitative behaviour of staggered and monolithic solvers were same, even though the time steps used were $1s$ and $4s$ respectively. Thus, to be able to apply the numerical model to predict the behaviour of any type of cell, it is necessary to have a solution scheme which is robust for any parameter values used. In this regard, monolithic coupling plays a crucial role.

6. Conclusion

6.1. Discussions

During the course of the thesis, biological experiments and numerical simulations were performed to understand the cell reorientation phenomenon. Observations from the experiments and the solutions obtained from the numerical model were compared. The solution schemes that could be followed to solve the coupled system of equations were analysed.

As mentioned in Chapter 1, to understand the complex behaviour of living organisms from the cellular level to that of an organism, the study has to be multi-disciplinary. Application of concepts of mechanics to biological materials, cell mechanics and biomechanics, have helped in understanding the responses of cells and organs to external mechanical forces. It has been found that mechanical properties of cells change during diseases such as asthma, and cancer. Thus, by observing the process of variation of mechanical properties, it might be possible to predict the final state of the cell, and thereby prevent the disease from spreading. In this regard, there have been many *in vivo* and *in vitro* experiments designed to understand the nature of cellular responses to a variety of mechanical stimuli. In addition, with advancements in numerical techniques and computational technologies several numerical models have been developed to simulate such cell behaviours, to be able to predict their response, and thereby prevent diseases. Thus, the principal aim of the thesis was to develop a numerical model to simulate the response of cells to a variety of mechanical loadings and validate them through experiments.

As explained in Chapter 2, cells are made up of cytoskeleton, which is responsible for their structural integrity. For a cell to survive, they have to attach to ECM. The bond between the cell and the ECM is developed by focal adhesions, which contain mechanosensitive proteins called integrins. The mechanotransduction process starts with the response of these integrins to external mechanical stimuli. Response to such stimuli leads to several bio-chemical reactions resulting in the growth of focal adhesions. As a consequence of the focal adhesion formation, actin and myosin proteins within the cytoplasm form a bond to form stress fibres. These stress fibres are usually found to extend from one end of the membrane to the other, terminating at focal adhesions. To understand the mechanisms involved in the formation of focal adhesion and stress fibres, several experiments, with a variety of stimuli mechanisms, have been performed. Some of them aimed at studying stress fibres only while some in studying focal adhesions. In addition, the crosstalk between stress fibres and focal adhesions has been studied in detail as well. The important observation from these experiments is that the behaviour of cells depend on the mechanical properties of its surroundings in addition to the stimuli it experiences. Along with the experimental techniques, numerical models have been developed to simulate the cell behaviour. In this regard, there are a few models simulating focal adhesions, while some simulate stress fibres. There are a few models that can simulate their interaction as well.

One of the experimental techniques used to study the response of cells to external stimuli is the *in vitro* cyclic stretching experiments. In this experimental procedure, cells attached to an elastic membrane reorient based on the magnitude and direction of cyclic loading parameters. In order to perform such experiments, a device, cell stretcher, which can apply a desired cyclic loading is needed. Thus, in chapter 3, a DIY design of the cell stretcher has been detailed and the process to be followed for additive manufacturing, following 3D printing, of the device has been explained. Since cells need to be adhered to a substrate, PDMS, a bio-compatible material with well characterised mechanical properties is used. The design of the mould used for the fabrication of PDMS substrate creating a well in the centre helped in preventing the cell solution spill. In addition, the right combination of the PDMS attachment clamps in the cell stretcher, and the design of the PDMS mould resulted in a well characterised strain field in the region where cells were cultured. Two stepper motors were used, controlled by an Arduino to apply the required cyclic load to cells. A combination of the nut and bolt mechanism was used as a linear actuator. The size of the device was limited to the size of a standard 96-well plate in order to be able to use it with any microscope systems. It was possible to place the cell stretcher inside the onstage incubator system of the EVOS fluorescence microscope thus enabling the live imaging of the cells. Using the cell stretcher thus built, uniaxial cyclic stretching experiments have been performed on two types of cells, NIH3T3 fibroblasts and MC3T3 osteoblasts.

The response of these cells subjected to uniaxial cyclic loading was similar to that observed in the literature; they reoriented away from the direction of loading. The magnitude of orientation was found to depend on the amplitude of the cyclic loading. Thus, when the cells were subjected to 7% stretch and 20% stretch, stress fibres were found to have a dominant angles of 50°, and 65° for fibroblasts while osteoblasts exhibited angles of 55°, and 62.5° respectively. Quantitative analysis of actin staining, representing the stress fibres, performed using ImageJ showed that the circularity of cells increased when they experience low amplitude cyclic loads (OL, FL), while it reduced significantly with an increase in the amplitude. In fact the value of the circularity obtained with high amplitude cyclic loads (OH, FH) was lower than that evaluated with no loading. Evaluation of the average value of $\cos 2\theta$ showed that with an increase in the amplitude of cyclic load, orientation of cells become less uniform and more dominant at particular angles. Even though fibroblast and osteoblast cell types have different physiological functions, the stress fibres are made up of actin-myosin cross bridge. Thus, by performing experiments on these two types of cells, it was possible to observe the difference in their response to same loading cycles.

Imaging cells through PDMS helped in understanding their response over time. It was observed that, in general, the response of osteoblast cells was slower than the fibroblast cells. It was observed that, for the same cyclic loading to the substrate, cells were found to have reoriented by 5 hours in case of fibroblasts while osteoblasts' response needed 8 hours. Due to the auto-fluorescence of PDMS at the low end of the light spectrum, it was not possible to observe the behaviour of response of stress fibres to such loading over time, using the fluorescence microscope. Fixing the cells after stretching and staining for actin and nucleus showed that even nucleus undergo reorientation and stretch due to such cyclic loadings, as seen in Fig. 6.1, whereas the fixed images of unstretched cells do not show such elongations as seen in Fig. 6.2. Though the exact mechanism involved in the nuclear deformation is not clear, it can be thought of as a reaction to the deformation of the cytoskeleton [20, 122].

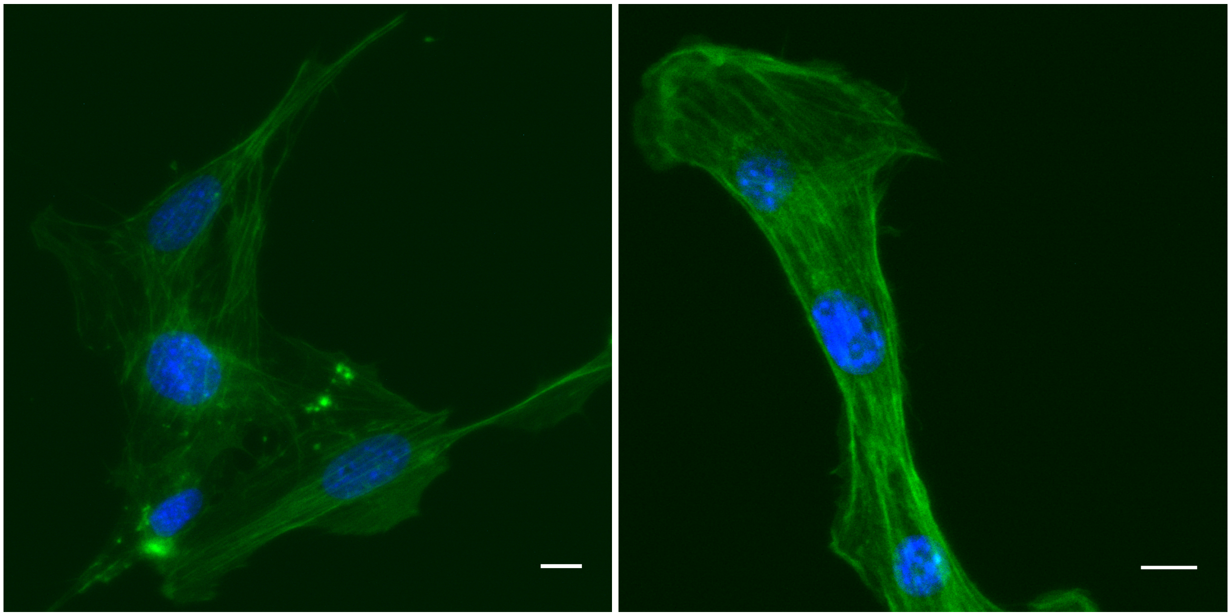

(A) (B)

Fig. 6.1: Nucleus orientation and elongation due to applied cyclic load in (A) Osteoblasts and (B) Fibroblasts. Scale bar = 20μm. Direction of loading $\longleftrightarrow$.

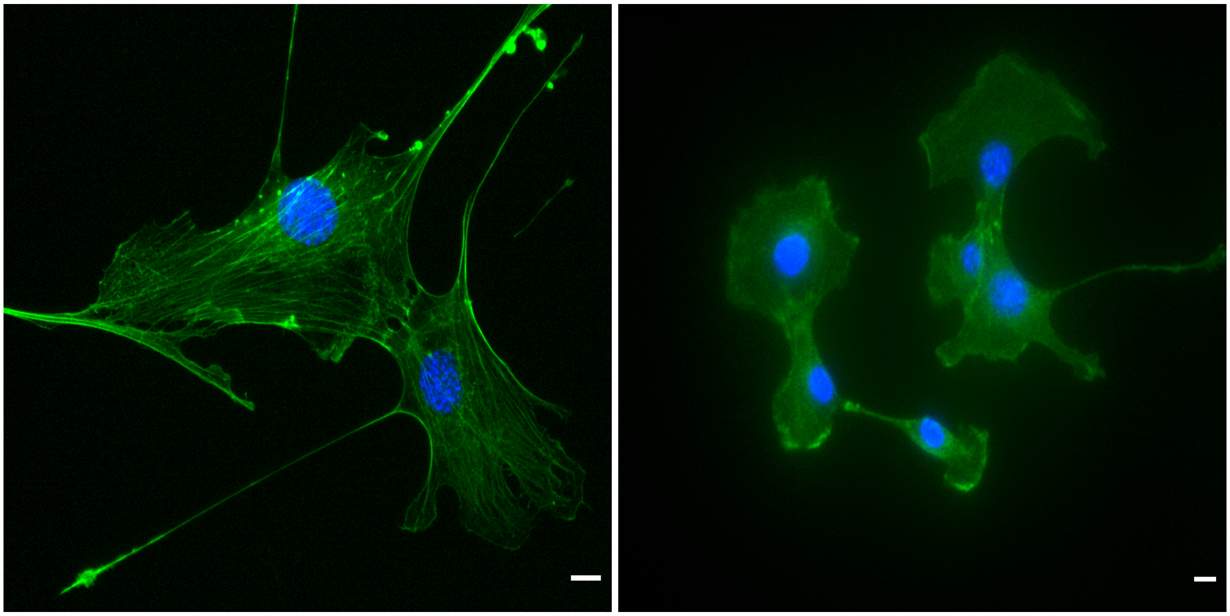

(A) (B)

Fig. 6.2: Undeformed nucleus in its reference unloaded state in (A) Osteoblasts and (B) Fibroblasts. Scale bar = 20μm.

Though the cyclic stretching experiments are performed *in vitro*, the response of cells to *in vivo* loading conditions can be predicted using suitable mathematical models. In this regard, in chapter 4, a model was developed as an extension of already existing stress fibre and focal adhesion growth models to include the feedback loop and use them to simulate the cyclic loading experiments, as performed in Chapter 3. Stress fibre growth was modelled as a first order ODE, where the active stress in the stress fibre, depending on the strain and the strain rate, and the calcium concentration, affected the instantaneous stress fibre concentration. Noting the similarities of stress fibres to muscle sarcomeres, a smooth non-linear Hill-type strain rate dependent function was used for the active stress. The total stress in the cell was assumed to be the sum of the active and passive stresses, where passive stress, assumed linear elastic, comes from the contribution of other components within the cytoplasm. Cells can sense the properties of the extra cellular matrix through the mechanosensitive proteins called integrins. The chemical potential of each of the integrins, low affinity and high affinity integrins, was evaluated, and an assumption that these two integrins were in thermodynamic equilibrium allowed their inter-conversion. The evaluated focal adhesion concentration was used to apply the traction force on the cell, and the mechanical equilibrium could be solved, thereby including the effect of focal adhesion growth on the equilibrium of the cell. Focal adhesion and stress fibre growths were not independent phenomenon. It was observed that there exists a feedback mechanism between them, which was included in the numerical model through a diffusion equation for the cytoplasmic calcium concentration, thereby explicitly affecting the stress fibre concentration due to focal adhesion growth. This resulted in a model with closed loop for the calcium signalling depending on the focal adhesion growth, which further affected the concentration of stress fibres.

The importance of the feedback loop has been shown through a numerical example, where the solution to a problem mimicking application of displacement to cell by optical tweezers is found. The growth of high affinity integrin concentration showed the need of a feedback loop in simulating the right physics of the cell behaviour. In addition, through a feedback loop, it was possible to bring the connection between focal adhesion and stress fibre concentration, as observed in ROCK inhibition simulation. The focal adhesion growth test on a square domain showed that the concentration of high affinity integrins, indicating focal adhesion, is higher on the boundary of the cell, as observed in experiments. By adding the substrate stress to the total stress in the cell, it was possible to simulate cyclic stretching experiments. The elastic substrate was subjected to uniaxial and biaxial cyclic loadings which resulted in heterogeneous distribution of stress fibre concentration. Solution to the problem of uniaxial cyclic loading showed that the stress fibre concentration reduces along the direction of loading with increasing amplitude, and therefore the stress fibre distribution appear to align away from the loading direction. But in the case of biaxial loading, stress fibre concentration did not show a preferred dominant direction. The response of the model to changes in substrate stiffness showed that the effect of cyclic loading is higher with increasing substrate stiffness. Solutions for the numerical problems were obtained by solving the coupled system of equations through a monolithic coupling scheme with small strain assumption.

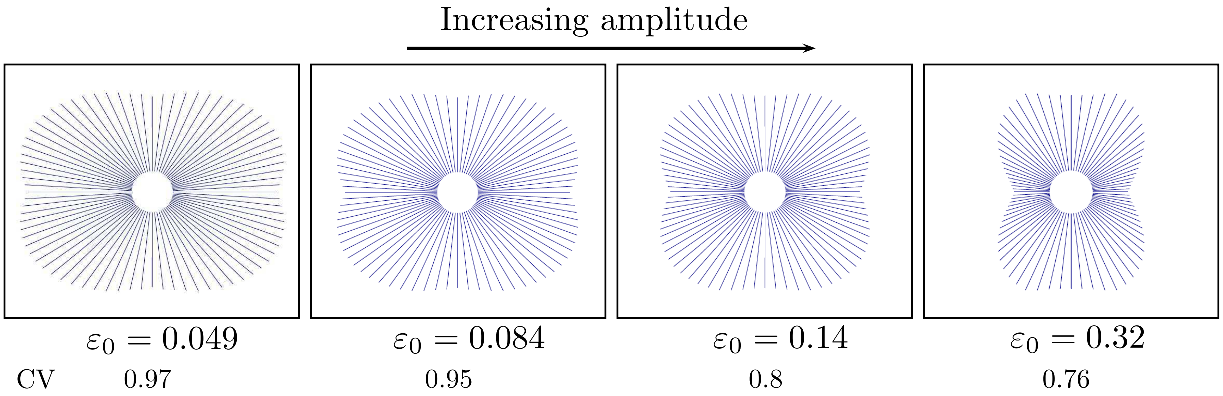

Fig. 6.3: Circular histogram obtained by simulation of stress fibre growth due to increasing amplitude of cyclic load. CV indicates circular variance for each loading amplitude. CV reduces with increase in amplitude of cyclic load. Direction of loading ⟷.

Load case FL (7% stretch)

Load case FH (20% stretch)

Fig. 6.4: Circular histograms obtained from experiments on fibroblasts for different amplitudes of cyclic load. CV indicates the circular variance. CV reduces with increase in amplitude of cyclic load. Direction of loading ⟷.

In Chapter 3, it was observed that, cyclic loading not only affects the stress fibres, but also the geometric properties of the nucleus. In the mathematical model introduced here, this aspect was neglected. In addition, the cell was assumed to be symmetric, leading to a symmetric circular histogram, as shown in Fig. 6.3. But, the circular histograms obtained from experimental observations in Chapter 3, were not symmetric, as shown in Fig. 6.4. Even with these assumptions, the numerical model could be used to solve a variety of bio-chemo-mechanical problems, which have been exhibited through the numerical examples, validating the solution with experimental observations qualitatively. In addition, the circular variance (CV) evaluated for both experimental observations and numerical simulations showed a decrease with an increase in loading amplitude.

The phenomenological model for the stress fibre, focal adhesion growth including the feedback loop leads to a coupled system of equations. It has been observed in the literature that the coupling scheme used for solving such a coupled problem has an effect on the robustness of the solution. In this regard, in Chapter 5, different coupling schemes, staggered and monolithic, were considered to solve the coupled system of equations. Even though small strain formulation was considered for the analysis presented in Chapter 4, for the sake of completeness, and to consider the effect of large displacements occurring during the biological experiments, large displacement formulation was considered for numerical analysis in chapter 5. But, it was later found that the large displacement formulation did not have any considerable effect on the solution to the numerical problems presented in Chapter 4. The main difference between staggered and monolithic coupling schemes is that in staggered coupling, the mechanical equilibrium was solved taking the high affinity integrin concentration from the previous time step while in the case of monolithic coupling, both, displacement and high affinity integrin concentrations were solved simultaneously. Thus, in order to solve for both the degrees of freedom in a single step, a coupled stiffness matrix is obtained, which is 1.5 times larger than that obtained by staggered coupling. The two step process followed by the staggered coupling scheme limits the value of the time step that can be used. In the case of monolithic scheme the value of the time step was found to have a negligible effect on the solution. In this regard, numerical examples were solved for changing parameter and time step sizes to study their effect on each of the coupling schemes. As discussed in Chapter 3, based on the physiological activities a particular cell type perform, the rate of stress fibre growth differs. In the phenomenological model presented in Chapter 4 and analysed in Chapter 5, different cell types could be simulated by changing the parameters, Hill constant $\bar{k}_v$, and strain rate constant $\dot{\varepsilon}_0$. Solutions showed that, these parameters influence the speed of convergence of the solution schemes to a steady-state solution. All tests showed a widely congruent result for a large time step monolithic solution in comparison with a small time step staggered solution, the latter showing reliability only for small time steps. Focal adhesion concentration obtained by monolithic coupling with a time step of 4s showed no difference when compared with that obtained by staggered coupling with 0.5s time step. The solution obtained with monolithic and staggered coupling schemes for stress fibre growth during cyclic loading simulations were found to give same results qualitatively even with different time step sizes. Thus, the monolithic scheme proved to be more robust compared to the staggered solver when solving the coupled equations of the bio-chemo-mechanical model including the feedback loop.

In sum, the cell stretcher device has been used to perform uniaxial cyclic loading experiments on the cell. The results obtained from the experiments could be compared with the solutions obtained by the phenomenological model developed for the stress fibre coupled with focal adhesion growth along with a feedback loop. The monolithic scheme for coupling the system of equations proved to be the robust way of coupling. Thus, with the experimental and numerical tools in hand, it is now possible to perform more biological experiments on stress fibres and focal adhesion and compare them with the numerical results. The experimental results can be used to upgrade the model if necessary, and the results from simulation could be used to design experiments as well.

6.2. Future Work

In this thesis, the uniaxial cyclic stretch experiments have been performed on fibroblast and osteoblast cells, which have been used successfully to validate the results obtained by numerical simulations. But, there are many possibilities where both experiments, and numerical modelling can be extended and thereby improved.

Experiments

1. Since the screw used in the rotary-linear conversion mechanism is 3D printed, there is a possibility that 1mm pitch might be a bit off, due to the errors occurring during printing. In addition, when the part is printed again, there is a possibility that the part might not be replicated accurately. Thus, either by using more accurate 3D printers or by using metal bolts, this source of error could be removed.

2. The cell stretcher which is built using the additively manufactured parts using the 3D printing technology is a cheap DIY solution to the very expensive commercial alternatives available in market. But, currently the design and the components used can provide cyclic load with mHz frequency only. This can be increased to Hz range either by changing the motor that is used, or by changing the pitch of the bolt that is used. Since the human body experiences cyclic load in frequency range of Hz, the *in vitro* experiments performed with frequency in Hz range would be closer to the *in vivo* loading experienced by a human body, and experiments could be performed on different cells such as endothelial cells.

3. PDMS mould can be redesigned to have partitions within the area where cells are cultured, as for e.g. done in [167]. Since the strain in each of the smaller areas can be accurately evaluated, the results can be used as different samples and can be used for statistical analyses.

4. Once the experiment is completed, the cells are fixed and stained for actin. The final stage of the fixing and staining process is to attach the PDMS to a glass cover slip. During this manual process, there is a high possibility of not attaching the PDMS membrane exactly parallel to the cover slip edges. This results in error while measuring the angles after microscopy imaging. In order to overcome this issue, a square raster image drawn on the acrylic in the PDMS mould, which is thereby printed on the PDMS is used for alignment. Though this seems to be a good way of alignment, the accuracy can be improved using some micro structure in the centre of the PDMS which can provide accurate references for horizontal and vertical alignments.

5. PDMS can be prepared by changing the ratio of curing agent to the elastomer liquid, giving different mechanical properties. Thus, experiments could be performed for varying substrate stiffness without any other changes.

6. The cell stretcher can be used to study the behaviour of cells on micropillars subjected to cyclic loading, as previously performed by [168]. The acrylic present in the centre of the mould can be modified to obtain micropillars in the well region of the PDMS substrate. Cells can be cultured in this region following the same procedure as followed in this thesis. The cyclic loading experiments on micropillars could lead to understand more about the role of focal adhesion on stress fibre growth and vice versa.

7. Since it is very easy to change the stiffness of the micropillars, different cases of loading and substrate conditions can be tested to understand the orientation behaviour of cells, based on applied strain and stress.

8. It might be interesting to observe the behaviour of calcium ions within the cytoplasm during cyclic loading and use the result to validate the model.

Numerical modelling

1. The model currently implemented can only experience isotropic stress from the substrate. The implementation could be extended to understand the behaviour of cells subjected to anisotropic substrate stress including anisotropic initial concentration of focal adhesion.

2. Simulation of cells placed on micropillars and subjected to cyclic loading would be another extension possible, as previously attempted on a grooved substrate by [169]. The displacement obtained by micropillar tracking experiments could be used as the Dirichlet boundary condition for the simulation.

3. As observed in [114], due to the dissociation of stress fibres when cells are subjected to a constant strain, the strain dependence function should be modified to include such a behaviour.

4. The future implementations have to consider improving the conditioning of the stiffness matrix.

5. Calcium concentration solved simultaneously with displacement and focal adhesion concentration can be used to predict the behaviour of calcium ions within cytoplasm for different loading conditions. This might be useful in the study of diseases such as diabetes and other heart related diseases.

6. Sophisticated focal adhesion-substrate bond model could be implemented, and along with the feedback loop, this would affect the behaviour of stress fibres too.

7. The model which includes the feedback mechanism, can now be extended to solve cell motility problems, and thereby simulate durotaxis.

8. In a larger context, model should be able to predict the behaviour of cells subjected to *in vivo* loadings, for example the displacement and force readings obtained from Gait analysis for bone cells.
9. As a bigger picture to the extension of this research, cell-cell interaction could be considered, and the model could be solved in a full 3D context including shear flow.

6.3. Summary : A Poem

A cell's response to stimuli

Cells, fundamental to living, yet intricate
have to survive without changing their fate.
How to understand them without apoptosis
is a million dollar question for the biologists.

They endure push and pull from the matrix, extra cellular
causing actin-myosin proteins to develop stress fibre.
They alter themselves along with the matrix around
due to mechanosensitive proteins, integrins, that are bound.

Apply cyclic load in one direction, they align away
irrespective of the cell type that is chosen as prey.
With an increase in amplitude, reorientation is higher
since they *strain avoid* to form stress fibres and live longer.

Developing mechanical models to simulate the behaviour
helps us to preform *in vitro* experiments with a new flavour.
The phenomenological model for stress fibre and focal adhesion
predicts right responses with feedback loop used for completion.

The coupled system of equations can be solved monolithically
which solves for a range of parameters and time steps robustly.
Modelling to bolster, questions in biology can see new answer
to help prevent and cure diseases that have troubled us forever
to make the earth a healthy planet for now and forever.

7. Appendices

7.1. Runge-Kutta Methods

Runge-Kutta methods are an important class of numerical methods used to find approximate solutions of ordinary differential equations. They were initially introduced by Carl Runge and Martin Kutta [170]. The main principle behind such methods is to approximate the integral according to some quadrature rule. Since it is possible to reduce higher order differential equations to a set of first order differential equations, Runge-Kutta methods are applicable for higher order differential equations as well. Consider the initial value problem (IVP):

$$\dot{y} = f(t, y(t)). \tag{7.1}$$

The general solution can be written as

$$y(t_{n+1}) = y^n + \int_{t_n}^{t_{n+1}} f(t, y(t))\, dt. \tag{7.2}$$

The integral can be approximated according to some quadrature rule as,

$$\int_{t_n}^{t_{n+1}} f(t, y(t))\, dt \approx h \sum_{l=1}^{m} \gamma_l k_l \tag{7.3}$$

where γ_l are certain weights, h is some time step and k_l are certain function evaluations $k_l = f(t, \hat{y}(t))$ and $l = 1...m$. Substituting Eq. 7.3 in Eq. 7.2, results in the so called m-stage Runge-Kutta method:

$$y^{n+1} = y^n + h \sum_{l=1}^{l=m} \gamma_l k_l \tag{7.4}$$

Based on the choice of m, γ and k, different quadrature approximations can be obtained. The choice $m = 1,\ \gamma_1 = 1,\ k_1 = f(t_n, y^n)$ yields

$$y^{n+1} = y^n + hf(t_n, y^n)$$

which represents explicit Euler scheme, while the choice $m = 2, \gamma_1 = 0, \gamma_2 = 1, k_1 = f(t_j, y^j), k_2 = f(t_j + \frac{h}{2}, y^j + \frac{h}{2}k_1)$ yields

$$y_{n+1} = y_n + hk_2 + O(h^3)$$

which corresponds to improved Euler method. Continuing this scheme, the classical Runge-Kutta or the fourth order Runge-Kutta method (RK4) can be obtained by choosing

$$\begin{aligned}
k_1 &= f(t_n, y_n) \\
k_2 &= f(t_n + \frac{h}{2}, y_n + \frac{k_1}{2}) \\
k_3 &= f(t_n + \frac{h}{2}, y_n + \frac{k_2}{2}) \\
k_4 &= f(t_n + h, y_n + k_3) \\
y_{n+1} &= y_n + \frac{k_1}{6} + \frac{k_2}{3} + \frac{k_3}{3} + \frac{k_4}{6} + O(h^5)
\end{aligned} \tag{7.5}$$

It can be seen that the RK4 method requires 4 function evaluations, and has an error of order 5. Based on this, explicit and improved Euler schemes can be termed RK1 and RK2 respectively. The general expression for the function evaluation can be written as

$$k_i = f\left(t_n + \alpha_i h, y^n + h\sum_{l=1}^{m} \beta_{i,l} k_l\right), i = 1, ..., m. \tag{7.6}$$

The coefficients used in the general expression, $\alpha_i, \beta_{i,l}$, along with the weights γ_l can be organised in a table known as Butcher table, as shown in Table. 7.1.

$$\begin{array}{c|ccc}
\alpha_1 & \beta_{1,1} & \cdot\ \cdot\ \cdot & \beta_{1,m} \\
\alpha_2 & \beta_{2,1} & \cdot\ \cdot\ \cdot & \beta_{2,m} \\
\cdot & \cdot & & \cdot \\
\cdot & \cdot & & \cdot \\
\cdot & \cdot & & \cdot \\
\alpha_m & \beta_{m,1} & \cdot\ \cdot\ \cdot & \beta_{m,m} \\
\hline
 & \gamma_1 & \cdot\ \cdot\ \cdot & \gamma_m
\end{array}$$

Table 7.1: General representation of Butcher table

For explicit Runge-Kutta method, since k_i can be computed using $k_1, ...k_{i-1}$, the Butcher table reduces to Table. 7.2

$$\begin{array}{c|cccc}
\alpha_1 & & & & \\
\alpha_2 & \beta_{2,1} & & & \\
\alpha_3 & \beta_{3,1} & \beta_{3,2} & & \\
\cdot & \cdot & \cdot & & \\
\cdot & \cdot & \cdot & & \\
\cdot & \cdot & \cdot & & \\
\alpha_m & \beta_{m,1} & \cdot\ \cdot\ \cdot & \beta_{m,m-1} & \\
\hline
 & \gamma_1 & \cdot\ \cdot\ \cdot & & \gamma_m
\end{array}$$

Table 7.2: Butcher table for explicit RK method

Thus, for Euler method, $m = 1$, the Butcher table reduces to Table. 7.3

$$\begin{array}{c|c}
0 & \\
\hline
 & 1
\end{array}$$

Table 7.3: Butcher table for explicit Euler method

while RK4 method can be represented by Table.7.4.

0				
$\frac{1}{2}$	$\frac{1}{2}$			
$\frac{1}{2}$	0	$\frac{1}{2}$		
1	0	0	1	
	$\frac{1}{6}$	$\frac{1}{3}$	$\frac{1}{3}$	$\frac{1}{6}$

Table 7.4: Butcher table for RK4 method

7.1.1. Embedded Runge Kutta Scheme

This scheme of Runge-Kutta method involves combining two RK schemes such that some or all ks match, in order to obtain a higher accuracy with a lower order function evaluations. The most popular embedded Runga-Kutta method is the RK4(5) scheme, where RK4 and RK5 are combined. The ODE45 function in Matlab (MathWorks), uses Cash-Karp algorithm for the RK4(5) method. The butcher table is given in 7.5. The local truncation error is estimated using order 6.

0						
$\frac{1}{5}$	$\frac{1}{5}$					
$\frac{3}{10}$	$\frac{3}{40}$	$\frac{9}{40}$				
$\frac{3}{5}$	$\frac{3}{10}$	$\frac{-9}{10}$	$\frac{6}{5}$			
1	$\frac{-11}{54}$	$\frac{5}{2}$	$\frac{-70}{27}$	$\frac{35}{27}$		
$\frac{7}{8}$	$\frac{1631}{55296}$	$\frac{175}{512}$	$\frac{575}{13824}$	$\frac{44275}{110592}$	$\frac{253}{4096}$	
RK4	$\frac{37}{378}$	0	$\frac{250}{621}$	$\frac{125}{594}$	0	$\frac{512}{1771}$
RK5	$\frac{2825}{27648}$	0	$\frac{18575}{48384}$	$\frac{13525}{55296}$	$\frac{277}{14336}$	$\frac{1}{4}$

Table 7.5: Butcher table for RK4(5) scheme

7.1.2. Adaptive step size control

The aim is to obtain the necessary result with desired accuracy using only necessary number of steps. That is the solution begins with an assumption of time step h. The value is evaluated at the next time step and local error is found. If the error is found to be less than the tolerance, then the step size chosen in necessarily less than required. Hence the time step is increased. If the error is higher than the tolerance, the time step is decreased and solution is progressed [165]. The ODE45 function used for integration in matlab uses RK4(5) function with adaptive step size control for integration.

7.2. Richardson extrapolation

If a sequence of approximations with different values of h is given as $y(f;h)$, $y(f;\frac{h}{2})$, $y(f;\frac{h}{4})$, ... The error for the trapezoid rule with step h can be written as

$$E(f;h) = I(f) - y(f;h) = a_2h^2 + a_4h^4 + a_6h^6 + ... \tag{7.7}$$

while the error with step $\frac{h}{2}$ can be written as

$$E(f;\frac{h}{2}) = I(f) - y(f;\frac{h}{2}) = a_2\frac{h}{2}^2 + a_4\frac{h}{2}^4 + a_6\frac{h}{2}^6 + ... \tag{7.8}$$

The exact integrals can then be written as

$$\begin{aligned} I(f) &= y(f;h) + a_2h^2 + a_4h^4 + a_6h^6 + ... + a_nh^n \\ I(f) &= y(f;\frac{h}{2}) + a_2\frac{h}{2}^2 + a_4\frac{h}{2}^4 + a_6\frac{h}{2}^6 + ... + a_n\frac{h}{2}^n \end{aligned} \tag{7.9}$$

Performing right manipulations such that the leading error term cancels leads to

$$(2^2-1)I(f) = 2^2T(f;\frac{h}{2}) - T(f;h) + a_4^{'}h^4 + \bar{a}_6h^6 + ... + \bar{a}_nh^n \tag{7.10}$$

Neglecting all the higher order error terms,

$$I(f) = \frac{1}{(2^2-1)}\left(2^2T(f;\frac{h}{2}) - T(f;h)\right) \tag{7.11}$$

A similar expansion performed for 4th order Runge-Kutta scheme leads to

$$I(f) = \frac{1}{(2^4 - 1)} \left(2^4 T(f; \frac{h}{2}) - T(f; h) \right) \tag{7.12}$$

7.3. 3D Printing

3D printing technology is a method of additive manufacturing, which has gained popularity in the recent times because of its cost effectiveness, simplicity and durability. One of the most famous printers today is the Ultimaker FDM 3D printer. In this printer, a plastic material in the form of solid tube is pushed into a nozzle which can melt the material and deposit on the hot glass plate according to the design developed in a CAD software in advance. Few common materials that is used for 3D printing are Poly Lactic Acid (PLA), Polycarbonate (PC), Nylon and Acrylonitrile Butadiene Styrene (ABS). Each of these materials has its own advantages and disadvantages depending on its material properties. For manufacturing the 3D printed cell stretcher, PLA and PC materials have been used.

7.3.1. PLA

PLA is the most popular material for 3D printing today. It is one of the easiest materials to print because of the low temperature needed to melt the material, and its capability to handle high print speeds. It can also provide high resolution of the print, which helps in developing prototypes and model with aesthetic details.

7.3.2. PC

PC is one of the engineering materials used in 3D printing. It is a very strong material with high tensile strength. But, it is not a very popular material because of the high temperature needed for printing. The accuracy is not that high, leading to changes that needs to be made in design to provide right tolerances.

The Base of the cell stretcher had to be very strong, while threads of the screw had to be accurate in order to get right strain distribution. In this regard, the base of the cell stretcher was printed with PC, while other parts were printed with PLA. PC can also sustain high temperatures upto 120^0, making it the right material to be used for the cell stretcher, since it has to be kept in the incubator at 37^0 for 8-10 hours. Comparison of material properties of PLA and PC is given in Table. 7.6.

Property	PLA	PC
Tensile strength	49.6 MPa	76.4 MPa
Printing temperature	200-210^0 C	260-280^0 C
Bed plate temperature	60^0 C	110^0 C

Table 7.6: Comparison of PLA and PC material properties

7.4. Statistical Analyses

In order to understand the data obtained from the experiments, statistical analyses are important. Statistical tests performed are

1. ANOVA
2. Multiple comparison test

All statistical tests are performed using the inbuilt functions in Matlab. ANOVA or analysis of variance is a test which compares the group means of a sample data, and provides result if the mean of different groups are equal. ANOVA was performed between different amplitude cases for both fibroblast and osteoblast cells, post-hoc multiple comparison test, results of which are given in Fig. 7.1

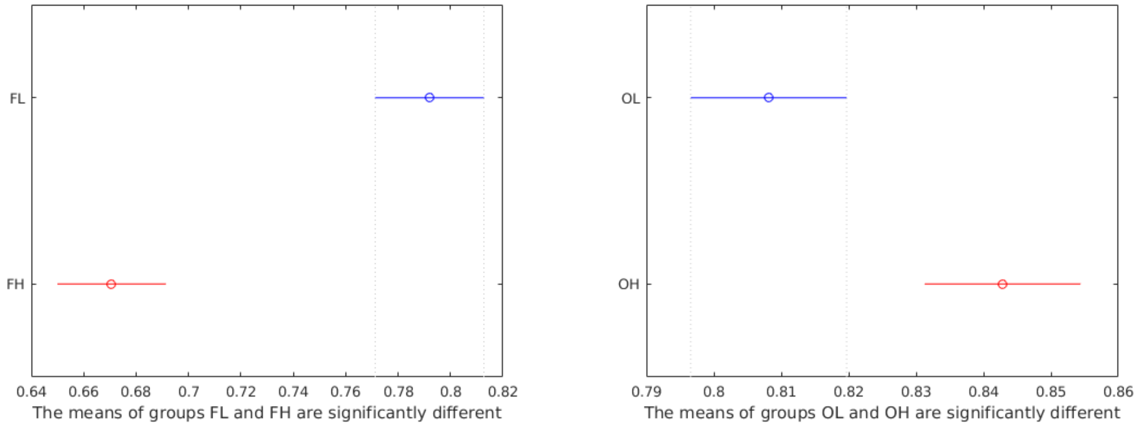

Fig. 7.1: Result of ANOVA post-hoc multiple comparison test of (A)Fibroblast cells and (B) Osteoblast cells for low and high amplitude loadings.

Bibliography

[1] Yuan-Cheng Fung. *Biomechanics:Mechanical Properties*. Springer New York, 1990.

[2] James D. Murray. *Mathematical Biology: I. An Introduction*. 3rd ed. Interdisciplinary Applied Mathematics. Springer-Verlag, 2002.

[3] Yuan-Cheng Fung. *Biomechanics:Motion, Stress and Growth*. Springer New York, 1993.

[4] David H. Boal. *Mechanics of the Cell*. Cambridge Univ. Press, 2008.

[5] Yu-li Wang and Dennis E. Discher. *Cell Mechanics*. 1st ed. Academic Press, 2007.

[6] Roland Kaunas et al. Cooperative effects of Rho and mechanical stretch on stress fiber organization. *Proceedings of the national academy of sciences of the united states of america*, 2005. DOI: `10.1073/pnas.0506041102`.

[7] Abhishek Tondon, Hui-Ju Hsu, and Roland Kaunas. Dependence of cyclic stretch-induced stress fiber reorientation on stretch waveform. *Journal of biomechanics*, 2012. DOI: `10.1016/j.jbiomech.2011.11.012`.

[8] Uta Faust et al. Cyclic stress at mHz frequencies aligns Fibroblasts in direction of zero strain. *Plos one*, 2011. Ed. by Markus J. Buehler. DOI: `10.1371/journal.pone.0028963`.

[9] Alexandra M. Greiner et al. Cyclic Tensile Strain Controls Cell Shape and Directs Actin Stress Fiber Formation and Focal Adhesion Alignment in Spreading Cells. *Plos one*, 28-Oct-2013. DOI: `10.1371/journal.pone.0077328`.

[10] Christine Obbink-Huizer et al. Computational model predicts cell orientation in response to a range of mechanical stimuli. *Biomechanics and modeling in mechanobiology*, 2014. DOI: `10.1007/s10237-013-0501-4`.

[11] Zhensong Wei et al. Analysis and interpretation of stress fiber organization in cells subject to cyclic stretch. *Journal of biomechanical engineering*, 2008. DOI: `10.1115/1.2907745`.

[12] Pradeep Keshavanarayana, Martin Ruess, and René de Borst. A feedback-loop extended stress fiber growth model with focal adhesion formation. *International journal of solids and structures*, 2017. DOI: `10.1016/j.ijsolstr.2017.08.023`.

[13] Pradeep Keshavanarayana, Martin Ruess, and René de Borst. On the monolithic and staggered solution of cell contractility and focal adhesion growth. *International journal for numerical methods in biomedical engineering*, 2018. DOI: `10.1002/cnm.3138`.

[14] Alexander G. Robling and Charles H. Turner. Mechanical Signaling for Bone Modeling and Remodeling. *Critical reviews in eukaryotic gene expression*, 2009.

[15] K. M. Khan and A. Scott. Mechanotherapy: how physical therapists' prescription of exercise promotes tissue repair. *British journal of sports medicine*, 2009. DOI: `10.1136/bjsm.2008.054239`.

[16] Paul Weiss and Beatrice Garber. Shape and movement of mesenchyme cells as functions of the physical structure of the medium. *Proceedings of the national academy of sciences of the united states of america*, 1952.

[17] Robert C. Buck. Reorientation response of cells to repeated stretch and recoil of the substratum. *Experimental cell research*, 1980. DOI: `10.1016/0014-4827(80)90456-5`.

[18] Ann A. Lee et al. An equibiaxial strain system for cultured cells. *American journal of physiology-cell physiology*, 1996. DOI: `10.1152/ajpcell.1996.271.4.C1400`.

[19] W. Ford Doolittle. A paradigm gets shifty. *Nature*, 1998. DOI: `10.1038/32033`.

[20] Rachel M. Stewart et al. Nuclear–cytoskeletal linkages facilitate cross talk between the nucleus and intercellular adhesions. *The journal of cell biology*, 2015. DOI: `10.1083/jcb.201502024`.

[21] A. Vaziri, H. Lee, and M.R. Kaazempur Mofrad. Deformation of the cell nucleus under indentation: Mechanics and mechanisms. *Journal of materials research*, 2006. DOI: `10.1557/jmr.2006.0262`.

[22] Paul Martin. Wound Healing–Aiming for Perfect Skin Regeneration. *Science*, 1997. DOI: `10.1126/science.276.5309.75`.

[23] William A. Muller. Leukocyte–endothelial-cell interactions in leukocyte transmigration and the inflammatory response. *Trends in immunology*, 2003. DOI: `10.1016/S1471-4906(03)00117-0`.

[24] Jean Paul Thiery. Epithelial-mesenchymal transitions in tumour progression. *Nature reviews. cancer*, 2002. DOI: `10.1038/nrc822`.

[25] Thomas Risler. Cytoskeleton and Cell Motility. *Arxiv*, 2009. DOI: `10.1007/978-0-387-30440-3_112`. arXiv: `1105.2423`.

[26] Revathi Ananthakrishnan and Allen Ehrlicher. The Forces Behind Cell Movement. *International journal of biological sciences*, 2007.

[27] Bruce Alberts et al. Fibroblasts and Their Transformations: The Connective-Tissue Cell Family. *Molecular Biology of the Cell.* 4th ed. New York: Garland Science, 2002.

[28] Cécile Sykes and Julie Plastino. Cell biology: Actin filaments up against a wall. *Nature*, 2010. DOI: `10.1038/464365a`.

[29] Viola Vogel and Michael Sheetz. Local force and geometry sensing regulate cell functions. *Nature reviews. molecular cell biology*, 2006. DOI: `10.1038/nrm1890`.

[30] Alex Mogilner. On the edge: modeling protrusion. *Current opinion in cell biology*, 2006. DOI: `10.1016/j.ceb.2005.11.001`.

[31] B. Geiger et al. Transmembrane crosstalk between the extracellular matrix–cytoskeleton crosstalk. *Nature reviews. molecular cell biology*, 2001. DOI: `10.1038/35099066`.

[32] Ronen Zaidel-Bar et al. Functional atlas of the integrin adhesome. *Nature cell biology*, 2007. DOI: `10.1038/ncb0807-858`.

[33] Pakorn Kanchanawong et al. Nanoscale architecture of integrin-based cell adhesions. *Nature*, 2010. DOI: `10.1038/nature09621`.

[34] Benoit Ladoux and Alice Nicolas. Physically based principles of cell adhesion mechanosensitivity in tissues. *Reports on progress in physics*, 2012. DOI: `10.1088/0034-4885/75/11/116601`.

[35] Sarita K. Sastry and Keith Burridge. Focal Adhesions: A nexus for intracellular signaling and cytoskeletal dynamics. *Experimental cell research*, 2000. DOI: `10.1006/excr.2000.5043`.

[36] Radoslav Janoštiak et al. Mechanosensors in integrin signaling: The emerging role of p130Cas. *European journal of cell biology*. Cell Migration and Invasion in Physiology and Pathology. 2014. DOI: `10.1016/j.ejcb.2014.07.002`.

[37] Frederick C MacKintosh and Christoph F Schmidt. Active cellular materials. *Current opinion in cell biology*. Cell Structure and Dynamics, 2010. DOI: `10.1016/j.ceb.2010.01.002`.

[38] G. Bao and S. Suresh. Cell and molecular mechanics of biological materials. *Nature materials*, 2003. DOI: `10.1038/nmat1001`.

[39] Sandra B. Lemke and Frank Schnorrer. Mechanical forces during muscle development. *Mechanisms of development*. Roles of Physical Forces in Development, 2017. DOI: `10.1016/j.mod.2016.11.003`.

[40] G. Isenberg et al. Cytoplasmic actomyosin fibrils in tissue culture cells. *Cell and tissue research*, 1976. DOI: `10.1007/BF00225909`.

[41] Keith Burridge and Erika S. Wittchen. The tension mounts: Stress fibers as force-generating mechanotransducers. *The journal of cell biology*, 2013. DOI: `10.1083/jcb.201210090`.

[42] S. Pellegrin and H. Mellor. Actin stress fibres. *Journal of cell science*, 2007. DOI: `10.1242/jcs.018473`.

[43] Démosthène Mitrossilis et al. Single-cell response to stiffness exhibits muscle-like behavior. *Proceedings of the national academy of sciences*, 2009. DOI: `10.1073/pnas.0903994106`.

[44] E. Lazarides. Tropomyosin antibody: the specific localization of tropomyosin in nonmuscle cells. *The journal of cell biology*, 1975. DOI: `10.1083/jcb.65.3.549`.

[45] W.h. Goldmann and G. Isenberg. Analysis of filamin and α-actinin binding to actin by the stopped flow method. *Febs letters*, 1993. DOI: `10.1016/0014-5793(93)80847-N`.

[46] M. Chrzanowska-Wodnicka and K. Burridge. Rho-stimulated contractility drives the formation of stress fibers and focal adhesions. *The journal of cell biology*, 1996. DOI: `10.1083/jcb.133.6.1403`.

[47] Christopher S. Chen. Mechanotransduction - a field pulling together? *Journal of cell science*, 2008. DOI: `10.1242/jcs.023507`.

[48] Robert J. Pelham and Yu-li Wang. Cell locomotion and focal adhesions are regulated by substrate flexibility. *Proceedings of the national academy of sciences*, 1997. DOI: `10.1073/pnas.94.25.13661`.

[49] Matthew J. Paszek and Valerie M. Weaver. The tension mounts: mechanics meets morphogenesis and malignancy. *Journal of mammary gland biology and neoplasia*, 2004. DOI: `10.1007/s10911-004-1404-x`.

[50] A. Wayne Orr et al. Mechanisms of mechanotransduction. *Developmental cell*, 2006. DOI: `10.1016/j.devcel.2005.12.006`.

[51] Amelia Khalili and Mohd Ahmad. A Review of Cell Adhesion Studies for Biomedical and Biological Applications. *International journal of molecular sciences*, 2015. DOI: `10.3390/ijms160818149`.

[52] Tom Shemesh et al. Focal adhesions as mechanosensors: A physical mechanism. *Proceedings of the national academy of sciences of the united states of america*, 2005. DOI: `10.1073/pnas.0500254102`.

[53] Vikram S. Deshpande et al. A bio-mechanical model for coupling cell contractility with focal adhesion formation. *Journal of the mechanics and physics of solids*, 2008. DOI: `10.1016/j.jmps.2007.08.006`.

[54] Michele A Wozniak et al. Focal adhesion regulation of cell behavior. *Biochimica et biophysica acta (bba) - molecular cell research*, 2004. DOI: `10.1016/j.bbamcr.2004.04.007`.

[55] José Luis Alonso and Wolfgang H. Goldmann. Cellular mechanotransduction. *Aims biophysics*, 2016. DOI: `10.3934/biophy.2016.1.50`.

[56] Marita L. Rodriguez, Patrick J. McGarry, and Nathan J. Sniadecki. Review on cell mechanics: experimental and modeling approaches. *Applied mechanics reviews*, 2013. DOI: `10.1115/1.4025355`.

[57] K.J Van Vliet, G Bao, and S Suresh. The biomechanics toolbox: experimental approaches for living cells and biomolecules. *Acta materialia*, 2003. DOI: `10.1016/j.actamat.2003.09.001`.

[58] Robert M. Hochmuth. Micropipette aspiration of living cells. *Journal of biomechanics*, 2000. DOI: `10.1016/S0021-9290(99)00175-X`.

[59] K L Sung et al. Leukocyte relaxation properties. *Biophysical journal*, 1988.

[60] Shin Daehwan and Athanasiou Kyriacos. Cytoindentation for obtaining cell biomechanical properties. *Journal of orthopaedic research*, 2005. DOI: `10.1002/jor.1100170613`.

[61] Daniel Riveline et al. Focal Contacts as Mechanosensors: Externally Applied Local Mechanical Force Induces Growth of Focal Contacts by an Mdia1-Dependent and Rock-Independent Mechanism. *The journal of cell biology*, 2001. DOI: `10.1083/jcb.153.6.1175`.

[62] Andrew J. Maniotis, Christopher S. Chen, and Donald E. Ingber. Demonstration of mechanical connections between integrins, cytoskeletal filaments, and nucleoplasm that stabilize nuclear structure. *Proceedings of the national academy of sciences*, 1997. DOI: `10.1073/pnas.94.3.849`.

[63] Akira Katsumi et al. Effects of cell tension on the small GTPase Rac. *The journal of cell biology*, 2002. DOI: `10.1083/jcb.200201105`.

[64] Karen A. Beningo et al. Nascent focal adhesions are responsible for the generation of strong propulsive forces in migrating fibroblasts. *The journal of cell biology*, 2001. DOI: `10.1083/jcb.153.4.881`.

[65] Fang Li et al. Cell shape regulates collagen type I expression in human tendon fibroblasts. *Cell motility and the cytoskeleton*, 2008. DOI: `10.1002/cm.20263`.

[66] John L. Tan et al. Cells lying on a bed of microneedles: An approach to isolate mechanical force. *Proceedings of the national academy of sciences*, 2003. DOI: `10.1073/pnas.0235407100`.

[67] Nathalie Q. Balaban et al. Force and focal adhesion assembly: a close relationship studied using elastic micropatterned substrates. *Nature cell biology*, 2001. DOI: `10.1038/35074532`.

[68] Marie FA Cutiongco et al. Predicting phenotype using morphological cell responses to nanotopography. *Biorxiv*, 2018. DOI: `10.1101/495879`.

[69] Christopher S. Chen et al. Cell shape provides global control of focal adhesion assembly. *Biochemical and biophysical research communications*, 2003. DOI: `10.1016/S0006-291X(03)01165-3`.

[70] Catherine G. Galbraith, Kenneth M. Yamada, and Michael P. Sheetz. The relationship between force and focal complex development. *The journal of cell biology*, 2002. DOI: `10.1083/jcb.200204153`.

[71] James H.-C. Wang et al. Specificity of endothelial cell reorientation in response to cyclic mechanical stretching. *Journal of biomechanics*, 2001. DOI: `10.1016/S0021-9290(01)00150-6`.

[72] Kazuaki Nagayama et al. Strain waveform dependence of stress fiber reorientation in cyclically stretched osteoblastic cells: effects of viscoelastic compression of stress fibers. *American journal of physiology-cell physiology*, 2012. DOI: `10.1152/ajpcell.00155.2011`.

[73] J. H. Wang. Substrate deformation determines actin cytoskeleton reorganization: A mathematical modeling and experimental study. *Journal of theoretical biology*, 2000. DOI: `10.1006/jtbi.1999.1035`.

[74] Ariel Livne, Eran Bouchbinder, and Benjamin Geiger. Cell reorientation under cyclic stretching. *Nature communications*, 2014. DOI: `10.1038/ncomms4938`.

[75] Manuel Théry et al. Cell distribution of stress fibres in response to the geometry of the adhesive environment. *Cell motility and the cytoskeleton*, 2006. DOI: `10.1002/cm.20126`.

[76] Abhishek Tondon and Roland Kaunas. The direction of stretch-induced cell and stress fiber orientation depends on collagen matrix stress. *Plos one*, 2014. Ed. by Sanjay Kumar. DOI: `10.1371/journal.pone.0089592`.

[77] Amy M. Collinsworth et al. Orientation and length of mammalian skeletal myocytes in response to a unidirectional stretch. *Cell and tissue research*, 2000. DOI: `10.1007/s004410000224`.

[78] Roland Kaunas, Shunichi Usami, and Shu Chien. Regulation of stretch-induced JNK activation by stress fiber orientation. *Cellular signalling*, 2006. DOI: `10.1016/j.cellsig.2006.02.008`.

[79] James H.-C. Wang, Pascal Goldschmidt-Clermont, and Frank C.-P. Yin. Contractility affects stress fiber remodeling and reorientation of Endothelial cells subjected to cyclic mechanical stretching. *Annals of biomedical engineering*, 2000. DOI: `10.1114/1.1317528`.

[80] Alejandro Nieponice et al. Mechanical stimulation induces morphological and phenotypic changes in bone marrow-derived progenitor cells within a three-dimensional fibrin matrix. *Journal of biomedical materials research part a*, 2007. DOI: `10.1002/jbm.a.31041`.

[81] Carsten Grashoff et al. Measuring mechanical tension across vinculin reveals regulation of focal adhesion dynamics. *Nature*, 2010. DOI: `10.1038/nature09198`.

[82] Colin P. Johnson et al. Forced unfolding of proteins within cells. *Science*, 2007. DOI: `10.1126/science.1139857`.

[83] Takeshi Kobayashi and Masahiro Sokabe. Sensing substrate rigidity by mechanosensitive ion channels with stress fibers and focal adhesions. *Current opinion in cell biology*, 2010. DOI: `10.1016/j.ceb.2010.08.023`.

[84] Paul A. Janmey and R. Tyler Miller. Mechanisms of mechanical signaling in development and disease. *Journal of cell science*, 2011. DOI: `10.1242/jcs.071001`.

[85] Démosthène Mitrossilis et al. Real-time single-cell response to stiffness. *Proceedings of the national academy of sciences*, 2010. DOI: `10.1073/pnas.1007940107`.

[86] G. I. Bell. Models for the specific adhesion of cells to cells. *Science*, 1978. DOI: `10.1126/science.347575`.

[87] Ulrich S. Schwarz, Thorsten Erdmann, and Ilka B. Bischofs. Focal adhesions as mechanosensors: The two-spring model. *Biosystems*, 2006. DOI: `10.1016/j.biosystems.2005.05.019`.

[88] Alice Nicolas, Benjamin Geiger, and Samuel A. Safran. Cell mechanosensitivity controls the anisotropy of focal adhesions. *Proceedings of the national academy of sciences*, 2004. DOI: `10.1073/pnas.0403539101`.

[89] Joseph E. Olberding et al. The non-equilibrium thermodynamics and kinetics of focal adhesion dynamics. *Plos one*, 2010. DOI: `10.1371/journal.pone.0012043`.

[90] Mirko Maraldi and Krishna Garikipati. The mechanochemistry of cytoskeletal force generation. *Biomechanics and modeling in mechanobiology*, 2015. DOI: `10.1007/s10237-014-0588-2`.

[91] Celeste M. Nelson et al. Emergent patterns of growth controlled by multicellular form and mechanics. *Proceedings of the national academy of sciences*, 2005. DOI: `10.1073/pnas.0502575102`.

[92] Camilla Mohrdieck et al. A Theoretical Description of Elastic Pillar Substrates in Biophysical Experiments. *Chemphyschem*, 2005. DOI: `10.1002/cphc.200500109`.

[93] Cornelis Storm et al. Nonlinear elasticity in biological gels. *Nature*, 2005. DOI: `10.1038/nature03521`.

[94] R. L. Satcher and C. F. Dewey. Theoretical estimates of mechanical properties of the endothelial cell cytoskeleton. *Biophysical journal*, 1996. DOI: `10.1016/S0006-3495(96)79206-8`.

[95] R. Bruinsma and E. Sackmann. Bioadhesion and the dewetting transition. *Comptes rendus de l'académie des sciences - series iv - physics-astrophysics*, 2001. DOI: `10.1016/S1296-2147(01)01225-2`.

[96] M. Dembo et al. The Reaction-Limited Kinetics of Membrane-to-Surface Adhesion and Detachment. *Proceedings of the royal society of london. series b, biological sciences*, 1988.

[97] E. A. Evans. Detailed mechanics of membrane-membrane adhesion and separation. I. Continuum of molecular cross-bridges. *Biophysical journal*, 1985. DOI: `10.1016/S0006-3495(85)83770-X`.

[98] L. B. Freund and Yuan Lin. The role of binder mobility in spontaneous adhesive contact and implications for cell adhesion. *Journal of the mechanics and physics of solids*, 2004. DOI: `10.1016/j.jmps.2004.05.004`.

[99] Achim Besser and Samuel A. Safran. Force-Induced adsorption and anisotropic growth of focal adhesions. *Biophysical journal*, 2006. DOI: `10.1529/biophysj.105.074377`.

[100] Igor L. Novak et al. Cooperativity between cell contractility and adhesion. *Physical review letters*, 2004. DOI: `10.1103/PhysRevLett.93.268109`.

[101] Umut Akalp et al. Structural modeling of mechanosensitivity in non-muscle cells: Multiscale approach to understand cell sensing. *Acs biomaterials science & engineering*, 2017. DOI: `10.1021/acsbiomaterials.6b00693`.

[102] Franck J. Vernerey and Umut Akalp. Role of catch bonds in actomyosin mechanics and cell mechanosensitivity. *Physical review e*, 2016. DOI: `10.1103/PhysRevE.94.012403`.

[103] A. V. Hill. The heat of shortening and the dynamic constants of muscle. *Proceedings of the royal society of london b: biological sciences*, 1938. DOI: `10.1098/rspb.1938.0050`.

[104] Andrew F Huxley. Muscle structure and theories of contraction. *Progress in biophysics and biophysical chemistry*, 1957.

[105] K. Kruse and F. Jülicher. Actively contracting bundles of polar filaments. *Physical review letters*, 2000. DOI: `10.1103/PhysRevLett.85.1778`.

[106] Preethi L. Chandran, Christopher B. Wolf, and Mohammad R. K. Mofrad. Band-like stress fiber propagation in a continuum and implications for myosin contractile stresses. *Cellular and molecular bioengineering*, 2009. DOI: `10.1007/s12195-009-0044-z`.

[107] D. E. Ingber. Cellular tensegrity: defining new rules of biological design that govern the cytoskeleton. *Journal of cell science*, 1993.

[108] Donald E. Ingber. Tensegrity I. Cell structure and hierarchical systems biology. *Journal of cell science*, 2003. DOI: `10.1242/jcs.00359`.

[109] K. D. Costa and F. C. P. Yin. Analysis of indentation: implications for measuring mechanical properties with atomic force microscopy. *Journal of biomechanical engineering*, 1999. DOI: `10.1115/1.2835074`.

[110] M. Dao, J. Li, and S. Suresh. Molecularly based analysis of deformation of spectrin network and human erythrocyte. *Materials science and engineering: c*. Proceedings of the First TMS Symposium on Biological Materials Science, 2006. DOI: `10.1016/j.msec.2005.08.020`.

[111] Frank P. T. Baaijens et al. Large deformation finite element analysis of micropipette aspiration to determine the mechanical properties of the Chondrocyte. *Annals of biomedical engineering*, 2005. DOI: `10.1007/s10439-005-2506-3`.

[112] Vikram S. Deshpande, Robert M. McMeeking, and Anthony G. Evans. A bio-chemo-mechanical model for cell contractility. *Proceedings of the national academy of sciences*, 2006. DOI: `10.1073/pnas.0605837103`.

[113] Franck J. Vernerey and Mehdi Farsad. A constrained mixture approach to mechano-sensing and force generation in contractile cells. *Journal of the mechanical behavior of biomedical materials*, 2011. DOI: `10.1016/j.jmbbm.2011.05.022`.

[114] A. Vigliotti et al. A thermodynamically motivated model for stress-fiber reorganization. *Biomechanics and modeling in mechanobiology*, 2015. DOI: `10.1007/s10237-015-0722-9`.

[115] Cheng Zhu, Gang Bao, and Ning Wang. Cell mechanics: mechanical response, cell adhesion, and molecular deformation. *Annual review of biomedical engineering*, 2000. DOI: `10.1146/annurev.bioeng.2.1.189`.

[116] Franck J. Vernerey and Mehdi Farsad. A mathematical model of the coupled mechanisms of cell adhesion, contraction and spreading. *Journal of mathematical biology*, 2014. DOI: `10.1007/s00285-013-0656-8`.

[117] Amit Pathak et al. An analysis of the cooperative mechano-sensitive feedback between intracellular signaling, focal adhesion development, and stress fiber contractility. *Journal of applied mechanics*, 2011. DOI: `10.1115/1.4003705`.

[118] A. Vigliotti, R. M. McMeeking, and Vikram S. Deshpande. Simulation of the cytoskeletal response of cells on grooved or patterned substrates. *Journal of the royal society interface*, 2015. DOI: `10.1098/rsif.2014.1320`.

[119] Wolfgang Alt and Micah Dembo. Cytoplasm dynamics and cell motion: two-phase flow models. *Mathematical biosciences*, 1999. DOI: `10.1016/S0025-5564(98)10067-6`.

[120] Nicola J. Armstrong, Kevin J. Painter, and Jonathan A. Sherratt. A Continuum approach to modelling cell-cell adhesion. *Journal of theoretical biology*, 2006. DOI: `10.1016/j.jtbi.2006.05.030`.

[121] J. Escribano, M. T. Sánchez, and J. M. García-Aznar. A discrete approach for modeling cell–matrix adhesions. *Computational particle mechanics*, 2014. DOI: `10.1007/s40571-014-0006-7`.

[122] Michele M. Nava, Manuela T. Raimondi, and Riccardo Pietrabissa. Bio-chemo-mechanical models for nuclear deformation in adherent eukaryotic cells. *Biomechanics and modeling in mechanobiology*, 2014. DOI: `10.1007/s10237-014-0558-8`.

[123] C. Michler et al. A monolithic approach to fluid–structure interaction. *Computers & fluids*, 2004. DOI: `10.1016/j.compfluid.2003.06.006`.

[124] Björn Hübner, Elmar Walhorn, and Dieter Dinkler. A monolithic approach to fluid–structure interaction using space–time finite elements. *Computer methods in applied mechanics and engineering*, 2004. DOI: `10.1016/j.cma.2004.01.024`.

[125] U. Küttler et al. Coupling strategies for biomedical fluid-structure interaction problems. *International journal for numerical methods in biomedical engineering*, 2010. DOI: `10.1002/cnm.1281`.

[126] Bernd Markert. *Weak or Strong: On Coupled Problems in Continuum Mechanics*. Report / Universität Stuttgart, Institut Für Mechanik (Bauwesen), Lehrstuhl II. OCLC: 699868505. Stuttgart: Institut für Mechanik (Bauwesen), Lehrstuhl II, 2010.

[127] Thomas D Brown. Techniques for mechanical stimulation of cells in vitro: a review. *Journal of biomechanics*, 2000. DOI: `10.1016/S0021-9290(99)00177-3`.

[128] Harshad Kamble et al. Cell stretching devices as research tools: engineering and biological considerations. *Lab chip*, 2016. DOI: `10.1039/C6LC00607H`.

[129] Yuli Huang and Nam-Trung Nguyen. A polymeric cell stretching device for real-time imaging with optical microscopy. *Biomedical microdevices*, 2013. DOI: `10.1007/s10544-013-9796-2`.

[130] Jasper Foolen et al. The influence of matrix integrity on stress-fiber remodeling in 3D. *Biomaterials*, 2012. DOI: `10.1016/j.biomaterials.2012.06.103`.

[131] Kamble Harshad et al. An electromagnetic cell-stretching device for mechanotransduction studies of olfactory ensheathing cells. *Biomedical microdevices*, 2016. DOI: `10.1007/s10544-016-0071-1`.

[132] F. Khademolhosseini et al. A magnetically actuated cellular strain assessment tool for quantitative analysis of strain induced cellular reorientation and actin alignment. *Review of scientific instruments*, 2016. DOI: `10.1063/1.4960567`.

[133] Craig B. Clark, Thomas J. Burkholder, and John A. Frangos. Uniaxial strain system to investigate strain rate regulation *in vitro*. *Review of scientific instruments*, 2001. DOI: `10.1063/1.1362440`.

[134] Axel Gerstmair et al. A device for simultaneous live cell imaging during uni-axial mechanical strain or compression. *Journal of applied physiology*, 2009. DOI: `10.1152/japplphysiol.00012.2009`.

[135] S Schürmann et al. The IsoStretcher : An isotropic cell stretch device to study mechanical biosensor pathways in living cells. *Biosensors and bioelectronics*, 2016. DOI: `10.1016/j.bios.2016.03.015`.

[136] Simon Jungbauer et al. Two Characteristic Regimes in Frequency-Dependent Dynamic Reorientation of Fibroblasts on Cyclically Stretched Substrates. *Biophysical journal*, 2008. DOI: `10.1529/biophysj.107.128611`.

[137] Jochen Guck et al. The Optical Stretcher: A Novel Laser Tool to Micromanipulate Cells. *Biophysical journal*, 2001. DOI: `10.1016/S0006-3495(01)75740-2`.

[138] Keir C Neuman and Steven M Block. Optical trapping. *Review of scientific instruments*, 2004. DOI: `10.1063/1.1785844`.

[139] Denis Desmaële, Mehdi Boukallel, and Stéphane Régnier. Actuation means for the mechanical stimulation of living cells via microelectromechanical systems: A critical review. *Journal of biomechanics*, 2011. DOI: `10.1016/j.jbiomech.2011.02.085`.

[140] N. Scuor et al. Design of a novel MEMS platform for the biaxial stimulation of living cells. *Biomedical microdevices*, 2006. DOI: `10.1007/s10544-006-8268-3`.

[141] Kyle Kurpinski and Song Li. Mechanical Stimulation of Stem Cells Using Cyclic Uniaxial Strain. *Jove (journal of visualized experiments)*, 2007. DOI: `10.3791/242`.

[142] Darina Hroncová et al. Kinematical Analysis of Crank Slider Mechanism Using MSC Adams/View. *Procedia engineering*, 2012. DOI: `10.1016/j.proeng.2012.09.507`.

[143] I D Johnston et al. Mechanical characterization of bulk Sylgard 184 for microfluidics and microengineering. *Journal of micromechanics and microengineering*, 2014. DOI: `10.1088/0960-1317/24/3/035017`.

[144] Yon Jin Chuah et al. Simple surface engineering of polydimethylsiloxane with polydopamine for stabilized mesenchymal stem cell adhesion and multipotency. *Scientific reports*, 2016. DOI: `10.1038/srep18162`.

[145] Jessamine Ng Lee et al. Compatibility of Mammalian Cells on Surfaces of Poly (dimethylsiloxane). *Langmuir*, 2004. DOI: `10.1021/la048562+`.

[146] Jongsoo Kim, Manoj K. Chaudhury, and Michael J. Owen. Hydrophobic Recovery of Polydimethylsiloxane Elastomer Exposed to Partial Electrical Discharge. *Journal of colloid and interface science*, 2000. DOI: `10.1006/jcis.2000.6817`.

[147] G.M. Bayley and P.E. Mallon. Surface studies of corona treated polydimethylsiloxane-*block* -polystyrene hybrid copolymer films. *Polymer engineering & science*, 2008. DOI: `10.1002/pen.21063`.

[148] *Corona Treatment Theory*. https://www.pillaartech.com.

[149] Yong Zhu, Masahisa Otsubo, and Chikahisa Honda. Degradation of polymeric materials exposed to corona discharges. *Polymer testing*, 2006. DOI: `10.1016/j.polymertesting.2006.01.003`.

[150] R. Rezakhaniha et al. Experimental investigation of collagen waviness and orientation in the arterial adventitia using confocal laser scanning microscopy. *Biomechanics and modeling in mechanobiology*, 2012. DOI: `10.1007/s10237-011-0325-z`.

[151] Johannes Schindelin et al. Fiji: an open-source platform for biological-image analysis. *Nature methods*, 2012. DOI: `10.1038/nmeth.2019`.

[152] Johannes Schindelin et al. The ImageJ ecosystem: An open platform for biomedical image analysis. *Molecular reproduction and development*, 2015. DOI: `10.1002/mrd.22489`.

[153] Bruno Capaccioni et al. Image analysis and circular statistics for shape-fabric analysis: applications to lithified ignimbrites. *Bulletin of volcanology*, 1997. DOI: `10.1007/s004450050158`.

[154] Gerhard Holzapfel, Jürgen Wehland, and Klaus Weber. Calcium control of actin-myosin based contraction in triton models of mouse 3T3 fibroblasts is mediated by the myosin light chain kinase (MLCK)-calmodulin complex. *Experimental cell research*, 1983. DOI: `10.1016/0014-4827(83)90192-1`.

[155] Kenichi Hirata et al. Involvement of tho p21 in the GTP-enhanced calcium ion sensitivity of smooth muscle contraction. *Journal of biological chemsitry*, 1992.

[156] Jeremiah T. Herlihy and Richard A. Murphy. Length-tension relationship of smooth muscle of the Hog Carotid artery. *Circulation research*, 1973. DOI: `10.1161/01.RES.33.3.275`.

[157] Yunfeng Chen et al. Receptor-mediated cell mechanosensing. *Molecular biology of the cell*, 2017. Ed. by Valerie Marie Weaver. DOI: `10.1091/mbc.e17-04-0228`.

[158] Hideji Murakoshi, Hong Wang, and Ryohei Yasuda. Local, persistent activation of Rho GTPases during plasticity of single dendritic spines. *Nature*, 2011. DOI: `10.1038/nature09823`.

[159] Kiran Bhadriraju et al. Activation of ROCK by RhoA is regulated by cell adhesion, shape, and cytoskeletal tension. *Experimental cell research*, 2007. DOI: `10.1016/j.yexcr.2007.07.002`.

[160] Martin Schwartz. Rho signalling at a glance. *Journal of cell science*, 2004. DOI: `10.1242/jcs.01582`.

[161] Xiang-Dong Ren et al. Disruption of Rho signal transduction upon cell detachment. *Journal of cell science*, 2004. DOI: `10.1242/jcs.01205`.

[162] T. Meyer and L. Stryer. Molecular model for receptor-stimulated calcium spiking. *Proceedings of the national academy of sciences*, 1988. DOI: `10.1073/pnas.85.14.5051`.

[163] J. D. Mih et al. Matrix stiffness reverses the effect of actomyosin tension on cell proliferation. *Journal of cell science*, 2012. DOI: `10.1242/jcs.108886`.

[164] René de Borst et al., eds. *Nonlinear Finite Element Analysis of Solids and Structures*. 2nd ed. Chichester: Wiley, 2012.

[165] William .H. Press et al. *Numerical Recipes - The Art of Scientific Computing*. 3rd ed. Cambridge University Press, 2007.

[166] Aram Soroushian, Peter Wriggers, and Jamshid Farjoodi. Asymptotic upper bounds for the errors of Richardson extrapolation with practical application in approximate computations. *International journal for numerical methods in engineering*, 2009. DOI: `10.1002/nme.2642`.

[167] Tsubasa S. Matsui, Hugejile Wu, and Shinji Deguchi. Deformable 96-well cell culture plate compatible with high-throughput screening platforms. *Plos one*, 2018. Ed. by Gernot Zissel. DOI: `10.1371/journal.pone.0203448`.

[168] Yidan Cui et al. Cyclic stretching of soft substrates induces spreading and growth. *Nature communications*, 2015. DOI: `10.1038/ncomms7333`.

[169] Tommaso Ristori et al. Prediction of Cell Alignment on Cyclically Strained Grooved Substrates. *Biophysical journal*, 2016. DOI: `10.1016/j.bpj.2016.09.052`.

[170] Runge–Kutta methods. *Wikipedia*, 2018. Page Version ID: 865751632.